JOINT INSTITUTE FOR NUCLEAR RESEARCH

Proceedings of VII ICFA Beam Dynamics Workshop on *Beam-Beam Issues for Multibunch, High Luminosity Circular Colliders*

Dubna, 18 - 20 May 1995

Edited by
P. Beloshitsky and E. Perelstein

Dubna 1996

Novosibirsk Tau-Charm Factory Design Study

N. Dikansky, V. Parchomchuk, A.N.Skrinsky, V. Yakimenko,
Budker Institute of Nuclear Physics, Novosibirsk, 630090, Russia

Abstract

A method of colliding beams is developed to study the fundamental properties of matter in two directions. The first direction is aimed at achieving higher energies allowing the discovery of new particles and fields. The goal of the second one is the study of more delicate fundamental properties of quarks and fields by increasing luminosity in crudely studied energy ranges. The study of CP violation is the most famous example. To study the CP violation in the region of B-quarks, the project of a B-factory as an asymmetrical electron-positron collider with a beam energy of 7/4 GeV and luminosity up to $10^{34} cm^{-2} s^{-1}$ was developed at BINP. During the development of this project, it became clear that the Institute's economical situation, which grew worse in the period of 1990-1993, did not allow us to carry out this project in a reasonable time. Besides, Japan (KEK) and USA (SLAC) began to build the B-factories. Therefore, it is hardly probable to obtain any new results on the third B-factory. On the other hand, a beam energy region of 0.7-2.5 GeV, which still is very interesting, is not studied completely. The interest in this field of research is due to a great body of information obtained on a LEAR facility which is utilized to study proton-antiproton annihilation approximately in this energy region. Studying the cross-section of birth of observed resonances in electron-positron annihilation noticeably increases the value and reliability of their interpretation. In 1993, as a result of discussions, the International Program Committee on High-Energy Physics of the Ministry of Science recommended to reorientate the Novosibirsk project VEPP-5 into a Tau-Charm-factory with high luminosity [1].

1. Parameters of Colliding Beams and Interaction Points

The beam parameters for the Tau-Charm-factory should satisfy the requirements for obtaining a maximum high luminosity of $1.0 10^{34} cm^{-2} s^{-1}$. In addition to the maximum luminosity regime, it is planned to obtain the beam parameters required for the so-called monochromatization of colliding beams and polarized colliding ones. To work in these regimes, the beam emittance control systems are needed. Thus, to obtain monochromatic colliding beams, it is necessary that the main contribution to the vertical size be made by energy spread at the interaction point and the vertical betatron size be substantially less. To control and preserve polarization, rather long solenoids with a longitudinal magnetic field are required. It is undoubtedly impossible to provide simultaneously all these regimes; so, regime-to-regime transition will be made by replacing magnetic elements in straight

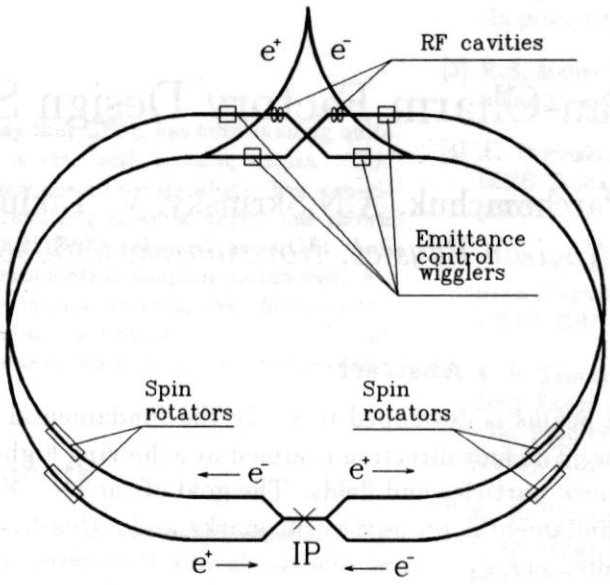

Figure 1: Schematic layout

sections. In this case, the contribution of half-rings into emittances should be as small as possible. The maximum luminosity of the facility is determined by the expression

$$L_{max} = \frac{cN_{max}\gamma\xi_{max}}{r_e D_{min}\sigma_l}, \tag{1}$$

where N_{max} is the maximum number of particles in a bunch; D_{min} is the interbunch distance, ξ_{max} is the parameters of beam interaction; r_e is the classical electron radius; $\gamma = E/mc^2$, and σ_l is the bunch length (sigma). Assuming that a RF system is used at a 700 MHz frequency and the interbunch distance is multiple to the RF wave length, we can present the beam parameters for the maximum luminosity in Table 1.

It is necessary full reconstruction of the experimental stright section to obtain ultra monochromatic colliding beams $\sigma_M \approx 6$ keV. The strong quadrupoles and weak dipoles should be used for beam separation and control of the vertical dispertion function at interection point. The length of such section estimated more than 30 m.

The Tau-Charm-factory is located in a tunnel with a $3x3m^2$ cross-section, whose floor and ceiling are 163 and 166 m above the sea level, respectively. The underground room consists of two half-rings, 89.58 m in radius, and strait section length 100 m, which connect the half-rings. In this case, the length of an ideal orbit is 773.036 m, corresponding to 1805 lengths of the RF wave. With such a geometry, each 19th separatriss contains a particle bunch; in all, the ring has 95 bunches. To install the injection equipment and magnetic systems of emittance control, the technical gap is increased up to $3x5m^2$. The gap should be widened to the side of injection channels so that to have 1.5 m to the inner

Energy (GeV)	2.0
Number of particles in bunch	2.010^{11}
Interbunch distance (m)	8.14
Beta-function at IP (cm)	1
The value of ξ_{max}	0.1
Beam radius $\sigma(\mu m)$	33
Beam emittance $\epsilon_x = \epsilon_y(cm)$	10^{-5}
Beam current (A)	1.12
Circumference (m)	773.036
Radius of ring (m)	89.63
Straite section length (m)	100
Luminosity $(cm^{-2}s^{-1})$	1.010^{34}

Table 1: Parameters of the TAU-Charm beams

Number of particles in bunch	1.510^{11}
Interbunch distance (m)	16.28
Beta-function at IP (cm) β_x/β_y	20 / 2
The value of ξ_{max}/ξ_D	0.05 / 0.01
Beam emittance ϵ_x/ϵ_y (cm)	10^{-5} / 10^{-9}
Beam current (A)	0.4
Energy resolution σ_M (keV)	6
Luminosity $(cm^{-2}s^{-1})$	5.010^{31}

Table 2: Parameters of the TAU-Charm beams for monochromatic coliding

wall and 3.5 m to the external one. The nearest-to-the-surface point of the tunnel is at a 10 m depth; the nearest-within-reach point is the bottom of a technological line, which is 168.6 m above the sea level, corresponding to a ground thickness of 2.6 m above the ceiling of the Tau-Charm-factory tunnel. At present, the tunnel, 200 m long, beginning from the injection complex to a shaft, where the injection channel of the Tau-Charm-factory begins, has been built. In the nearest future, we shall begin to build the channels distributing the electron and positron bunches into an injection gap. The factory is built by the firm "Gornyak" at a pace depending mainly on the financial possibilities. Keeping the pace, we shall need about 5 years to build the underground part.

2. Element of Magnetic System Periodicity

The Tau-Charm-factory magnetic system consists of two storage rings located over each other and intercrossing at the interaction point. To provide collisions of longitudinally polarized beams, spin rotators are supposed to be installed in the half-rings. As an example of the specific magnetic system, we present a simple system which consists of a dipole magnet, 1.5 m long, with a field of 1024 G and quadrupole lenses, each has a 0.4 m length, whose parameters are given in detail in Table 2. In the energy monochromatization regime, the beams remain round, with a dispersion radius of 33 micrometers; the

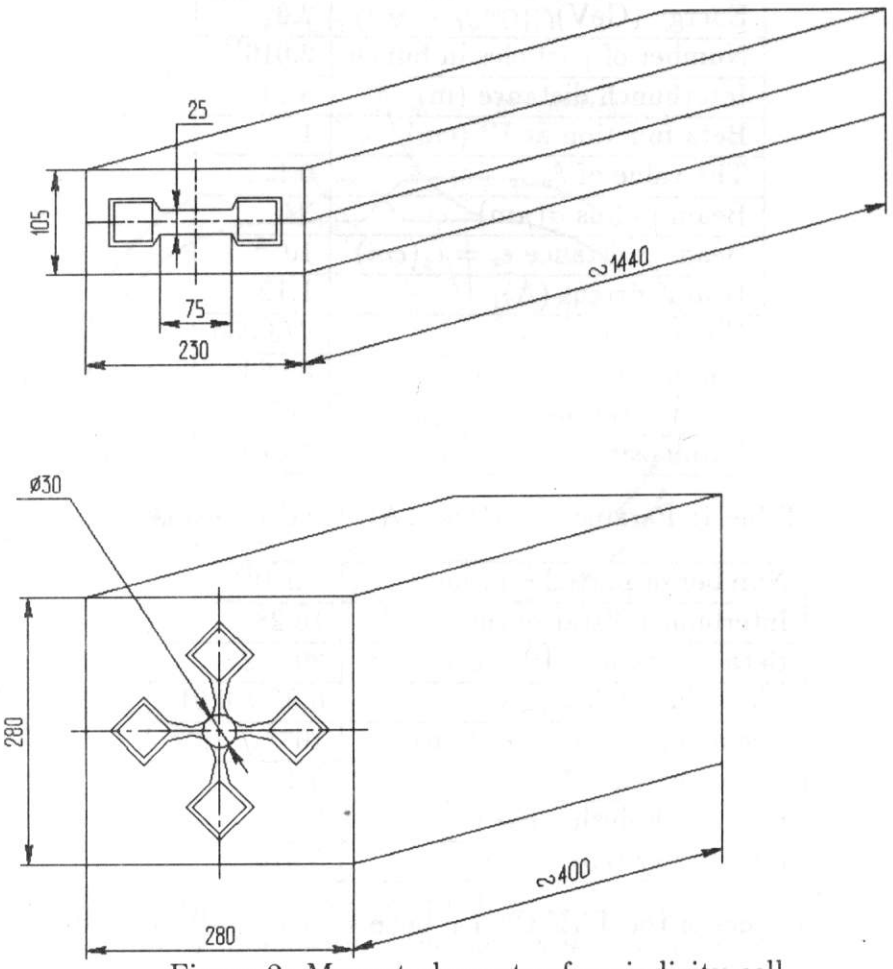

Figure 2: Magnet elements of periodicity cell

value of a vertical energy dispersion is chosen according to the spread. In this case, the value of monochromatization is determined by the ratio of the vertical betatron size and the vertical energy one.

3. Emittance Control Section

To control emittance, it is necessary to use special magnetic system sections where the magnetic field can be changed. A well-known element used for this purpose is the Wiggler-magnet which allows us to noticeably increase the energy loss for radiation. As a rule, the ψ-function is small in the wiggler-magnet. As a result, introducing strong decay, the magnet does not give a considerable increase in the emittance. Let us consider a special magnet design which gives a strong dispersion and the introducing of which will significantly increase the emittance. The equation for the ψ-function has the form

$$\frac{d^2\psi}{ds^2} + G\psi = K. \tag{2}$$

In a smoothed approximation, in the case where the frequency is assumed to be constant along the magnetic gap and the dipole magnetic field to be modulated by the resonance

	Length (cm)	Field (kG)	Gradient (kG/cm)
Quad	40		1.0631
Gap	30		
Dipole	150	1.042	
Gap	30		
Quad	40		-1.0631
Gap	30		
Dipole	150	1.042	
Gap	30		

Table 3: Parameters of the magnet elements

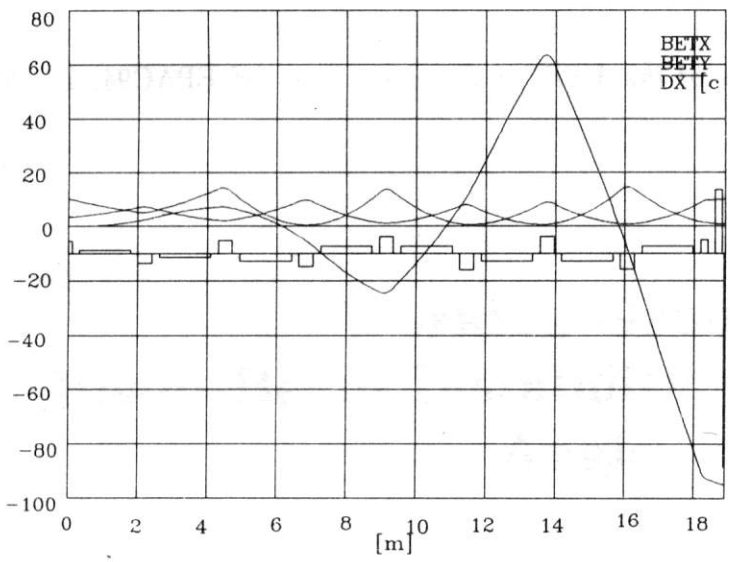

Figure 3: Insertion of the ψ-function control

frequency, the amplitude of the ψ-function beats increases linearly. To obtain the necessary emittance under these conditions, the length of such a section should be several tens meters. At the point where ψ is maximum, the Wiggler-magnet controlling the emittance value in the given direction is placed. For two rings, the electron and positron ones, we need four Wiggler-magnets to independently tune the beam emittances.

4. Interaction Point

The most interesting possibility of obtaining the maximum luminosity is the setting up of the interaction point with a small β-function using a strong longitudinal field (9.6 T and 2.18 m long). Possessing symmetrical focusing in both directions, such a system satisfies the idea of operation with round beams and can allow us to obtain the parameters for a space charge $\xi_{max} > 0.1$. The main problem in setting up the interaction point is a necessity of electrostatic beam separation. The total length of separation plates with a field of 100 kV/cm is 2 m. They are located at the point where the β-function value is high, presenting the difficulties in providing the coherent beam stability. A steady

obtaining of a powerful electrical field under the conditions of synchrotron irradiation of the separation plates is also a rather serious problem.

5. Conclusion

The construction of the Tau-Charm-factory under the existing economic conditions in Russia is not a simple problem. However, the successful completion of this project will allow us to enter the third thousand years with an interesting machine which the world scientific community needs to acquire fundamental knowledge.

References

[1] Dikansky N.S., at al. *Status of the VEPP-5 Complex*, Proc. of EPAC94, London, 1994, p,482

Synchrobetatron Beam-Beam Resonances in Long Bunches Due to Horizontal Crossing

D.V. Pestrikov
Budker Institute for Nuclear Physics
630090 Novosibirsk, Russian Federation
pestrikov@inp.nsk.su

1. Introduction

The goal luminosities of the future electron-positron factories must reach huge values ($10^{33} \div 10^{34}$ $1/\mathrm{cm}^2\mathrm{s}$). As is known, the luminosity of a collider generally can be increased rising the collision frequency, or/and simultaneously reducing the β-function at the interaction point (β_z^*) and the lengths of colliding bunches (σ_s). In large colliders the collision frequency is increased using the multi-bunch beams. In order to avoid, or to suppress effects from parasitic collisions it is reasonable to use the schemes, where in the interaction region the orbits of colliding bunches cross each-other at some angle (2ϕ, see in Fig.1). The performance of schemes with the crossing in the vertical plane is limited by resonances between vertical and synchrotron oscillations of particles [1]. Since usually colliding bunches have very small vertical size the limitation, found in [1], seems to be very severe to use the schemes with vertical crossings in the high-luminosity collider projects. For this reason, the designs of the future B-factories mainly focus on the schemes with the crab- or conventional crossing in the horizontal plane (see, for instance, [2, 3]). Since the crab-crossing is a very new technique, the schemes with a conventional crossing in the horizontal plane are presently considered as a number one for practical applications.

Present understanding of the beam-beam instability in colliding schemes with small β-function and σ_s cannot be reduced to several simple recipes and generally, demands an additional study. From one side, due to large phase advance of betatron oscillations along the interaction region (the so-called phase-averaging effect [4]) this can strongly suppress the beam-beam resonances [4, 5, 6]. From the other, an increase in the angular spread of bunches due to the decrease in β_z^* results in the spontaneous crossings of the counter-moving bunch with angles ($\phi_{eff} \sim a_z/\beta_z^*$) and in corresponding excitation of synchrobetatron resonances. The study of the common effect of the phase averaging and of the crossing angle was only started in Refs.[7] and [8].

In this paper we calculate the strengths of the synchrobetatron beam-beam resonances with the excitation of vertical betatron oscillations and tune shifts for long bunches, crossing each-other in the horizontal plane. These resonances occur due to a nonlinear

dependence of the beam-beam deflecting force on the transverse offsets of a particle. In a collider with flat bunches, like B-factory, relevant instability of the vertical betatron oscillations can limit the acceptable value of the crossing angle. In colliders with round bunches, these resonances can result in additional limitations to those, which were found in [9], on the position of the working point in the tune space. We assume the weak-strong

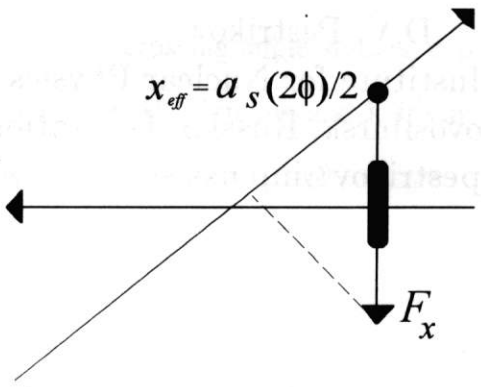

Figure 1: Collision scheme.

beam approximation, zero dispersion function in the interaction region and neglect the lattice chromatic effects.

2. Strengths of Resonances

The oscillations of particles in the interaction region will be described by the following equations:

$$
\begin{gathered}
z = \sqrt{J_z\beta_z(s)}\cos(\psi_z + \alpha_z(s)), \quad x = \sqrt{J_x\beta_x(s)}\cos(\psi_x + \alpha_x(s)), \\
s = R_0\theta = ct + R_0\varphi, \quad R_0\varphi = a_s\cos\psi_s, \quad \Delta p = -\frac{p_0\nu_s}{\eta}\varphi_s\sin\psi_s, \\
R_0(p_z/p) = dz/d\theta = z', \quad R_0(p_x/p) = x', \quad \Delta p = p - p_0, \\
\psi_z' = \nu_z, \quad \frac{d}{ds}(\psi_z + \alpha_z) = \frac{1}{\beta_z}, \quad \psi_x' = \nu_x, \quad \frac{d}{ds}(\psi_x + \alpha_x) = \frac{1}{\beta_x} \quad \psi_s' = \nu_s, \\
I_{z,x} = \frac{pJ_{z,x}}{2}, \quad I_s = \frac{p\nu_s a_s^2}{2R_0|\eta|} = \frac{pJ_s}{2}.
\end{gathered}
\tag{1}
$$

Here, $\Pi = 2\pi R_0$ is the perimeter of the closed orbit, $\eta = (1/\gamma^2) - \alpha$, α is the momentum compaction factor, and $p_0 \simeq \gamma Mc$ is the momentum of the synchronous particle. Equations of motion of the test particle from the weak beam are generated by the Hamiltonian:

$$
H(J, \psi, \theta) = \nu_x J_x + \nu_z J_z + \nu_s J_s - V_{bb}(J, \psi, \theta), \tag{2}
$$

where the term V_{bb} describes the perturbations due to the beam-beam interaction. For the sake of simplicity we assume that the distribution over transverse coordinates in the strong bunch $\rho(\mathbf{r}_\perp)$ is a Gaussian

$$\rho(\mathbf{r}_\perp) = \frac{N}{2\pi\sigma_x\sigma_z}\exp\left(-\frac{(x+\phi s)^2}{2\sigma_x^2} - \frac{z^2}{2\sigma_z^2}\right). \tag{3}$$

Then, if $\lambda(s)$ is a linear density in the strong bunch, for ultrarelativistic $\gamma \gg 1$ electron and positron bunches colliding at the angle 2ϕ (see in Fig.1) we can write V_{bb} in the following form

$$V_{bb} = \frac{4Ne^2R_0}{pc}\lambda(s+ct)\int\frac{d^2k}{\pi k^2}\exp\left\{i[k_x(x+2\phi s)+k_z z] - \frac{k_x^2\sigma_x^2 + k_z^2\sigma_z^2}{2}\right\}. \tag{4}$$

This equation describes the perturbation of the weak bunch as a sequence of the periodic and very short kicks (during $\Delta t \simeq \sigma_s/c$, where σ_s is a bunch length). Since without other perturbations equations of motion read

$$J'_\alpha = \frac{\partial V_{bb}}{\partial\psi_\alpha}, \quad \psi'_\alpha = \nu_\alpha - \frac{\partial V_{bb}}{\partial J_\alpha}, \quad \alpha = x, z, s, \tag{5}$$

the amplitudes ($\sqrt{J_\alpha}$) and phases (ψ_α) of oscillations get systematic variations when the tunes (ν_x, ν_z and ν_s) approach the resonant values

$$m_x\nu_x + m_z\nu_z + m_s\nu_s = n. \tag{6}$$

The strengths of these resonances are estimated by the values of the amplitudes of the Fourier-expansion of V_{bb} in phases and azimuth

$$V_{bb} = \sum_{m,n} V_{m,n}\exp(i[m_x\psi_x + m_z\psi_z + m_s\psi_s - n\theta]), \quad m \equiv \{m_x, m_z, m_s\}. \tag{7}$$

Using an expansion

$$\exp[ika\cos\psi] = \sum_{m=-\infty}^{\infty} i^m J_m(ka)e^{im\psi},$$

and Eq.(4) we rewrite V_{mn} in the following form

$$V_{m,n} = \frac{2Ne^2}{\pi pc}\int_0^{2\pi}\frac{d\psi_s}{2\pi}e^{-im_s\psi_s}\int_{-\infty}^{\infty}ds\lambda(2s - a_s\cos\psi_s)\int\frac{d^2k}{\pi k^2}J_{m_x}(k_x\sqrt{J_x\beta_x(s)})\times$$
$$J_{m_z}(k_z\sqrt{J_z\beta_z(s)})\exp\left\{-\frac{k_x^2\sigma_x^2 + k_z^2\sigma_z^2}{2} - ik_x 2\phi s + im_z\psi_z(s) + im_x\psi_x(s)\right\}, \tag{8}$$

where $d\psi_{x,z}(s)/ds = 1/\beta_{x,z}(s)$. Generally, an analysis of particle motion with such perturbations is embarrassed by very complicated dependences of amplitudes V_{mn} on the amplitudes of particles oscillations. To simplify this analysis we consider a special case, when colliding bunches are very flat so that

$$\sigma_x \gg \sigma_z, \quad \beta_x^* \gg \beta_z^*,$$

and when their closed orbits intersect each other in the horizontal plane at small angle ϕ. Taking into account that near the interaction point the betatron functions vary according to

$$\beta_x(s) = \beta_x^* + \frac{s^2}{\beta_x^*}, \quad \beta_z(s) = \beta_z^* + \frac{s^2}{\beta_z^*},$$

and

$$\psi_x(s) = \arctan(s/\beta_x^*), \quad \psi_x(s) = \arctan(s/\beta_x^*).$$

we find that in the region $\beta_x^* \gg \beta_z^*$ the harmonics $V_{m,n}$ can be calculated neglecting the variations of β_x and ψ_x along the interaction region. Then, for a resonance $m_z\nu_z + m_s\nu_s = n$ we obtain (for the sake of simplicity we take $J_x = 0$)

$$V_{m,n} \simeq \frac{2Ne^2}{\pi pc} \int \frac{d^2k}{\pi k^2} \int_0^{2\pi} \frac{d\psi_s}{2\pi} e^{-im_s\psi_s} \int_{-\infty}^{\infty} ds\lambda(2s - R_0\varphi)\times$$
$$\cdot J_{m_z}(k_z\sqrt{J_z\beta_z(s)}) \exp\left\{-\frac{k_x^2\sigma_x^2 + k_z^2\sigma_z^2}{2} - ik_x 2\phi s + im_z\psi_z(s)\right\}. \tag{9}$$

In the region $\sigma_z \ll a_z \ll \sigma_x$ due to a fast convergency of the integral over k_x, we can neglect in Eq(9) the variation of $1/k^2$ with k_x. Remaining integration over k_x yields

$$\int_{-\infty}^{\infty} dk_x \exp\left\{-\frac{k_x^2\sigma_x^2}{2} - ik_x 2\phi s\right\} = \frac{\sqrt{2\pi}}{\sigma_x} \exp\left\{-\frac{2\phi^2 s^2}{\sigma_x^2}\right\} \tag{10}$$

Substituting this expression in Eq.(9), we obtain

$$V_{m,n} = Y_m^f V_{m,n}^{(0)}. \tag{11}$$

Here, (see in [10] and in Appendix A for more detail)

$$V_{m,n}^{(0)} = 2\xi_z\epsilon_z\sqrt{\frac{2}{\pi}} \int_{-\infty}^{\infty} \frac{dv}{v^2} J_{m_z}(2v\sqrt{\chi_z}) e^{-v^2/2}, \quad \chi_z = \frac{J_z}{4\epsilon_z},$$

$$= \begin{cases} \dfrac{2\xi_z\epsilon_z k e^{-\chi_z}}{k^2 - 1/4}\left(I_k(\chi_z) + \dfrac{\chi_z}{k+1/2}[I_k(\chi_z) + I_{k+1}(\chi_z)]\right), & m_z = 2k\ , \\ 0, & m_z = 2k+1\ , \end{cases} \tag{12}$$

is the strength of the resonance calculated for the synchronous particle due to head-on collisions with a strong bunch of a zero length, ξ is the so-called beam-beam parameter

$$\xi_z = \frac{Ne^2\beta_z^*}{2\pi pc\sigma_x\sigma_z}, \tag{13}$$

and

$$Y_m^f = 2\int_0^{2\pi} \frac{d\psi_s}{2\pi} e^{-im_s\psi_s} \int_{-\infty}^{\infty} ds\lambda(2s - R_0\varphi) \exp\left\{-\frac{2\phi^2 s^2}{\sigma_x^2} + im_z\psi_z(s)\right\} \sqrt{\frac{\beta_z(s)}{\beta_z^*}} \tag{14}$$

is the so-called resonance suppression factor [4, 5, 6]. For a Gaussian linear density in the strong bunch we can rewrite Eq.(14) in the form

$$Y_m^f = \sqrt{2/\pi}\int_0^{2\pi}\frac{d\psi_s}{2\pi}e^{-im_s\psi_s}\int_{-\infty}^{\infty}du\exp\left(-2\left[u-\frac{a_s\cos\psi_s}{2\sigma_s}\right]^2\right.$$
$$\left.-\frac{2\phi^2\sigma_s^2u^2}{\sigma_x^2}+im_z\psi_z(\zeta u)\right)\sqrt{1+\zeta^2u^2},\quad \zeta=\sigma_s/\beta_z^*. \tag{15}$$

Note, that this expression only by a factor $\exp(-2\phi^2\sigma_s^2u^2/\sigma_x^2)$ in the integrand differs from similar expressions, calculated for head-on collisions of long bunches (see, for instance, in Ref.[6]). As against the case of short bunch, Y^f in Eq.(15) generally differs from zero for both even and odd m_s. It means that the interaction with a long bunch is accompanied by excitation of additional family of synchrobetatron resonances with $m_s = 2k+1$. Some impression concerning effects of the bunch length and of the crossing angle

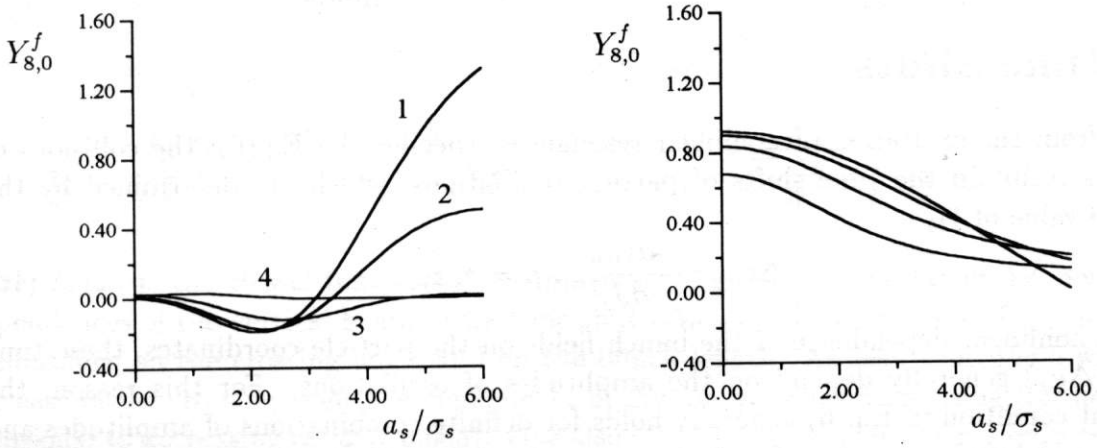

Figure 2: Dependence of Y_m^f on amplitude of synchrotron oscillations; $\sigma_x/\sigma_s = 0.01$, $m_z = 8$, $m_s = 0$. Left picture - $\sigma_s = \beta$, 1: $\phi = 0.0$, 2: $\phi = 0.0025$, 3: $\phi = 0.005$, 4: $\phi = 0.01$. Right picture - $\sigma_s = 0.1\beta$, from top to bottom (at $a_s = 0$) $\phi = 0.0$, 0.0025, 0.005, 0.01.

on the strength of betatron resonances (as an example we take the resonance $\nu_z = 1/8$) gives Fig.2. Like in the case of head-on collisions, comparable values of σ_s and β_z^* result in the significant suppression of betatron resonances at small amplitudes of synchrotron oscillations ($a_s \leq \sigma_s$; bunch core). Left picture in Fig.2 indicates, however, that with an increase in the crossing angle the width of the suppression region in a_s increases. As seen from Fig.3, such a behavior of Y_m^f is common for both betatron and synchrobetatron resonances. Conversely, right picture in Fig.2 shows a very little effect of the crossing angle on the strength of betatron resonances, if strong bunch is short. A comparison of Figs.3 and refyfsb2 shows that strengths of next synchrobetatron resonances is not necessarily smaller. This fact is not very surprising since for short bunches ($\sigma_s \to 0$) there are no odd synchrobetatron resonances at all.

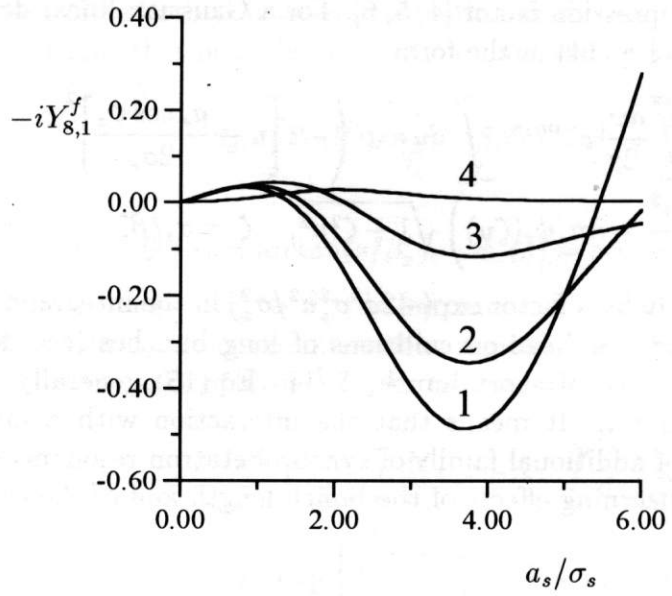

Figure 3: Dependence of Y^f_m on amplitude of synchrotron oscillations; $\sigma_s = \beta$, $\sigma_x/\sigma_s = 0.01$, $m_z = 8$, $m_s = 1$, 1: $\phi = 0.0$, 2: $\phi = 0.0025$, 3: $\phi = 0.005$, 4: $\phi = 0.01$.

3. Tune Shifts

Apart from the excitation of nonlinear resonances, specified by Eq.(6), the collisions of bunches result in the tune shifts of particle oscillations, which are determined by the average value of V_{bb}

$$\Delta\nu_\alpha = -\frac{\partial V_{0,0}}{\partial J_\alpha}, \quad \alpha = x, z, s, \tag{16}$$

Due to nonlinear dependence of the bunch fields on the particle coordinates, these tune shifts ($\Delta\nu_\alpha$) generally depend on the amplitudes of oscillations. For this reason, the resonant condition in Eq.(6) generally holds for definite combinations of amplitudes and therefore, determines some surface in the space of variables J_x, J_z and J_s. For our example we have to calculate $\Delta\nu_z(J_z, J_s)$ and $\Delta\nu_s(J_z, J_s)$. That can be done directly, using Eqs(16) and (9). For the tune shift of vertical oscillations we write

$$\Delta\nu_z(J_z, J_s) = \frac{2Ne^2}{\pi pc}\int\frac{d^2k}{\pi k^2}\int_0^{2\pi}\frac{d\psi_s}{2\pi}\int_{-\infty}^{\infty} ds\lambda(2s - R_0\varphi)\times$$

$$\frac{k_z\sqrt{\beta_z(s)}}{2\sqrt{J_z}}J_1(k_z\sqrt{J_z\beta_z(s)})\exp\left\{-\frac{k_x^2\sigma_x^2 + k_z^2\sigma_z^2}{2} - ik_x 2\phi s\right\}. \tag{17}$$

Assuming $\beta_x^* \gg \beta_z^*$, we again neglect in this expression the variation of β_x along the interaction region, as well as the variation of $1/k^2$ with k_x. Then, for a Gaussian linear

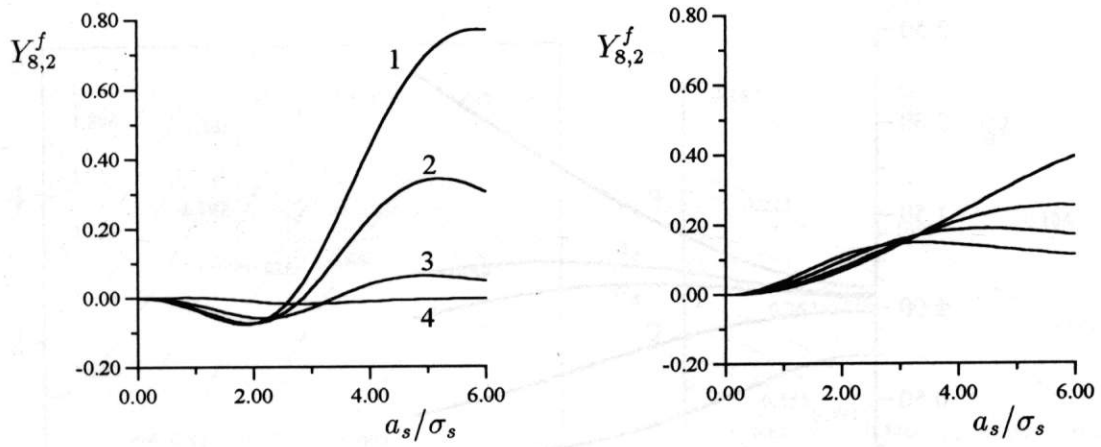

Figure 4: Dependence of Y^f_m on amplitude of synchrotron oscillations; $\sigma_x/\sigma_s = 0.01$, $m_z = 8$, $m_s = 2$. Left picture - $\sigma_s = \beta$, 1: $\phi = 0.0$, 2: $\phi = 0.0025$, 3: $\phi = 0.005$, 4: $\phi = 0.01$. Right picture - $\sigma_s = 0.1\beta$, from top to bottom (at $a_s = 6\sigma_s$) $\phi = 0.0$, 0.0025, 0.005, 0.01.

density simple transformations result in [1]

$$\Delta\nu_z(J_z, J_s) = \xi_z e^{-\chi_z}[I_0(\chi_z) + I_1(\chi_z)]Y^f_0(a_s, \zeta), \quad \chi_z = J_z/(4\epsilon_z),$$

$$Y^f_0 = \sqrt{\frac{2}{\pi}} \int_0^{2\pi} \frac{d\psi_s}{2\pi} \int_{-\infty}^{\infty} du \exp\left(-2\left[u - \frac{a_s \cos\psi_s}{2\sigma_s}\right]^2 - \frac{2\phi^2\sigma_s^2 u^2}{\sigma_x^2}\right) \sqrt{1+\zeta^2 u^2}. \tag{18}$$

Here, $I_m(x)$ is the Bessel function of an imaginary argument. The factor Y^f_0 describes dependences of the vertical beam-beam tune shift ($\Delta\nu_z$) on the amplitude of synchrotron oscillations, on the crossing angle and on the bunch length. As seen from Fig.5 with an increase in the crossing angle the dependence of $\Delta\nu_z$ on a_s varies from rising (for head-on collisions) to decreasing (at $\phi \geq 0.003$). One also can mention that in the region $\phi \simeq 0.003$ (and for aspect ratio $\sigma_z/\sigma_x = 0.01$) this dependence becomes very weak. The variation in resonant lines for betatron resonances ($\Delta\nu_z(a_z, a_s) = -\varepsilon_{mn}$, $\varepsilon_{mn} = \nu_z - (n/m)$) with an increase in the crossing angle is shown in Figs.6. If the beam cooling does not destroy the resonances, a damping of synchrotron oscillations will result in the drifting of particles along these resonant lines. Then, from Fig.6(a) we can conclude that for head-on collisions particles can reach the bunch core region only in the vicinity of the lower border of the resonant stopband, while at the upper border ($|\varepsilon_{mn}| \ll \xi_z$) most resonant lines end outside

[1] From Eq.(12) we find that the resonant contribution to $\Delta\nu_z$:

$$(\Delta\nu_z)_m = -\frac{\xi_z k e^{-\chi_z}}{k^2 - 1/4}\left[I_k(\chi_z)\left(1 + \frac{k+1}{k+1/2} + \frac{k}{\chi_z}\right) + \frac{I_{k+1}(\chi_z)}{2k+1}\right]\cos(m\psi_m), \quad m = 2k,$$

where $\psi_m = \psi_z - \theta(n/m)$ is the so-called slow phase, is small for higher order resonances.

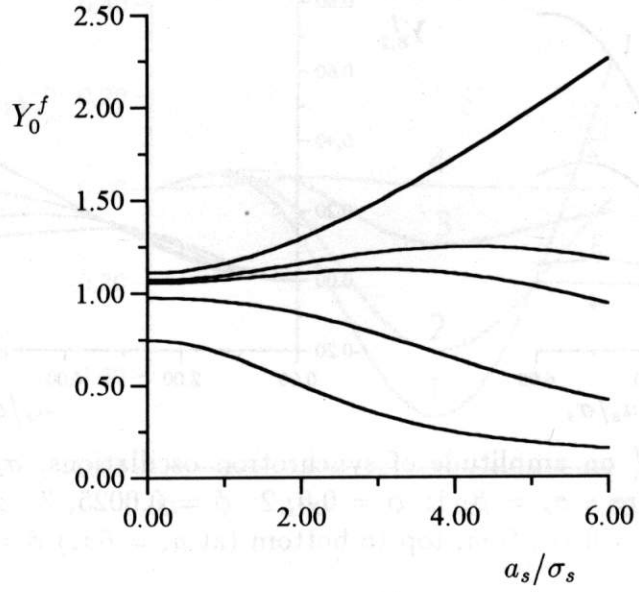

Figure 5: Dependence of Y_0^f on amplitude of synchrotron oscillations; $\sigma_s = \beta$, $\sigma_x/\sigma_s = 0.01$, from top to bottom: $\phi = 0, 0.0025, 0.003, 0.005, 0.01$.

the bunch core. For high crossing angles (Fig.6(b)) the resonant lines have non-positive slopes, which will result in the blowup of vertical oscillations due to longitudinal cooling (see, for instance, in Ref.[11]).

The tune shift of synchrotron oscillations can be calculated similarly. Using Eq.(16) we write

$$\Delta\nu_s = -\frac{\eta R_0}{2\nu_s a_s}\frac{\partial V_{0,0}}{\partial a_s}. \tag{19}$$

Since a_s enters in this expression via the function $\lambda(2s - a_s\cos\psi_s)$, we can use

$$\frac{\partial\lambda}{\partial a_s} = -\frac{\cos\psi_s}{2}\frac{\partial\lambda}{\partial s}.$$

Then, after integration in Eq.(19) over s by parts, we rewrite this equation in the form

$$\Delta\nu_s = -\frac{\eta R_0}{2\nu_s a_s}\frac{Ne^2}{\pi pc}\int\frac{d^2k}{\pi k^2}\int_0^{2\pi}\frac{d\psi_s}{2\pi}\cos\psi_s\int_{-\infty}^{\infty}ds\lambda(2s - a_s\cos\psi_s)$$
$$\times\frac{d}{ds}\left\{J_0(k_z\sqrt{J_z\beta_z})\exp\left(-\frac{k_x^2\sigma_x^2}{2} - \frac{k_z^2\sigma_z^2}{2}\left(1 + \frac{s^2}{\beta_z^{*2}}\right) - 2ik_x\phi s\right)\right\}. \tag{20}$$

The calculation of the derivative over s in the integrand results in an expression

$$\Delta\nu_s = \Delta_1 + \Delta_2 + \Delta_3, \tag{21}$$

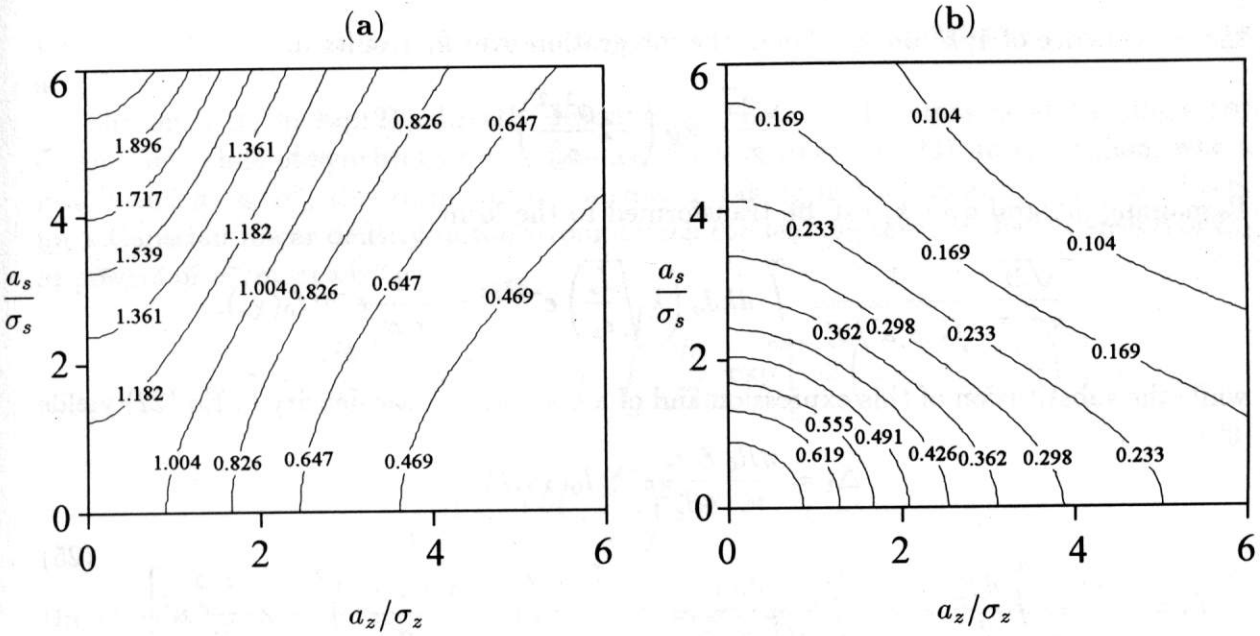

Figure 6: Resonant lines for the vertical betatron oscillations; **a**: $\phi = 0$, **b**: $\phi = 0.01$. The numbers near contour lines give the ratio ε_{mn}/ξ_z, $\sigma_s = \beta$, $\sigma_x/\sigma_s = 0.01$.

where

$$\Delta_1 = \frac{\eta R_0}{2\nu_s a_s}\frac{Ne^2}{\pi pc}\frac{\sigma_z^2}{\beta_z^{*2}}\int_0^{2\pi}\frac{d\psi_s}{2\pi}\cos\psi_s\int_{-\infty}^{\infty}dss\lambda(2s - a_s\cos\psi_s) \tag{22}$$

$$\times\int\frac{d^2kk_z^2}{\pi k^2}J_0(k_z\sqrt{J_z\beta_z})\exp\left(-\frac{k_x^2\sigma_x^2}{2} - \frac{k_z^2\sigma_z^2}{2}\left(1 + \frac{s^2}{\beta_z^{*2}}\right) - 2ik_x\phi s\right),$$

$$\Delta_2 = \frac{\eta R_0}{2\nu_s a_s}\frac{Ne^2}{\pi pc}\int_0^{2\pi}\frac{d\psi_s}{2\pi}\cos\psi_s\int_{-\infty}^{\infty}ds\lambda(2s - a_s\cos\psi_s) \tag{23}$$

$$\times\int\frac{d^2k2i\phi k_x}{\pi k^2}J_0(k_z\sqrt{J_z\beta_z})\exp\left(-\frac{k_x^2\sigma_x^2}{2} - \frac{k_z^2\sigma_z^2}{2}\left(1 + \frac{s^2}{\beta_z^{*2}}\right) - 2ik_x\phi s\right),$$

and

$$\Delta_3 = \frac{\eta R_0}{2\nu_s a_s}\frac{Ne^2}{\pi pc}\frac{\sqrt{J_z}}{\beta_z^{*3/2}}\int_0^{2\pi}\frac{d\psi_s}{2\pi}\cos\psi_s\int_{-\infty}^{\infty}\frac{dss}{\sqrt{1 + (s/\beta_z^*)^2}}\lambda(2s - a_s\cos\psi_s) \tag{24}$$

$$\times\int\frac{d^2kk_z}{\pi k^2}J_1(k_z\sqrt{J_z\beta_z})\exp\left(-\frac{k_x^2\sigma_x^2}{2} - \frac{k_z^2\sigma_z^2}{2}\left(1 + \frac{s^2}{\beta_z^{*2}}\right) - 2ik_x\phi s\right).$$

For the case of very flat bunches ($r = \sigma_z/\sigma_x \ll 1$) these very complicated expressions can be essentially simplified. Let us briefly discuss, for example, the calculation of Δ_1. We note that, if the aspect ratio r of the bunch is very small, and since the main contribution to integral over k_x in Eq.(22) gives the region $|k_x|\sigma_x \leq 1$, we may neglect in this expression

the dependence of $1/k^2$ on k_x. Then, the integration over k_x results in

$$\frac{\sqrt{2\pi}}{\sigma_x}\exp\left(-2\frac{\phi^2 s^2}{\sigma_x^2}\right).$$

Remaining integral over k_z can be transformed to the form

$$\frac{\sqrt{2\pi}}{\pi\sigma_x\sigma_z}\frac{1}{\sqrt{1+s^2/\beta_z^{*2}}}\int\limits_{-\infty}^{\infty}dkJ_0\left(k\sqrt{\frac{J_z}{\epsilon_z}}\right)e^{-k^2/2}=\frac{2}{\sigma_x\sigma_z}e^{-\chi_z}I_0(\chi_z),$$

while the substitution of this expression and of a Gaussian linear density in Eq.(22) yields

$$\Delta_1=\frac{\eta R_0}{\nu_s}\frac{\xi_z\epsilon_z}{4\beta_z^{*2}}e^{-\chi_z}I_0(\chi_z)F_1$$

$$F_1=\frac{8\sigma_s}{a_s\sqrt{2\pi}}\int\limits_0^{2\pi}\frac{d\psi_s}{2\pi}\cos\psi_s\int\limits_{-\infty}^{\infty}\frac{duu}{\sqrt{1+\zeta^2u^2}}\exp\left[-2\left(u-\frac{a_s\cos\psi_s}{2\sigma_s}\right)^2-2\frac{\phi^2\sigma_s^2}{\sigma_x^2}u^2\right]. \tag{25}$$

This expression can be simplified for synchrotron oscillations with small amplitudes ($a_s \ll \sigma_s$), when the leading contribution to Δ_1 reads

$$\Delta_1=\frac{\eta R_0}{\nu_s}\frac{\xi_z\epsilon_z}{\beta_z^{*2}}e^{-\chi_z}I_0(\chi_z)\frac{e^{\chi_x/\zeta^2}[K_1(\chi_x/\zeta^2)-K_0(\chi_x/\zeta^2)]}{\sqrt{2\pi}\zeta^3} \tag{26}$$

$$\chi_x=\Sigma_x^2/\sigma_x^2,\quad \Sigma_x^2=\sigma_x^2+\phi^2\sigma_s^2.$$

For a short strong bunch ($\zeta \ll 1$) using

$$e^z[K_1(z)-K_0(z)]\approx\frac{\sqrt{\pi}}{(2z)^{3/2}},\quad |z|\gg 1$$

we obtain form Eq.(26)

$$\Delta_1=\frac{\eta R_0}{\nu_s}\frac{\xi_z\epsilon_z}{4\beta_z^{*2}}\left(\frac{\sigma_x}{\Sigma_x}\right)^3,\quad \chi_z\ll 1,\quad a_s\ll\sigma_s,\quad \zeta\ll 1. \tag{27}$$

Similar calculations result in the following expression for Δ_3

$$\Delta_3=\frac{\eta R_0}{\nu_s}\frac{\xi_z\epsilon_z}{4\beta_z^{*2}}(\chi_z/2)e^{-\chi_z}[I_0(\chi_z)+I_1(\chi_z)]F_1,\quad a_z=\sqrt{J_z\beta_z^*}\ll\sigma_x. \tag{28}$$

Note, that in contrast to Eq.(25) the contribution from Δ_3 to $\Delta\nu_s$ increases $\propto\sqrt{\chi_z}$ for large amplitudes of betatron oscillations until $a_z \ll \sigma_x$. This term describes an effect of the crossings of the strong bunch at the angles due to betatron oscillations of a particle, when $\phi_{eff}\sim\sqrt{J_z/\beta_z^*}$. Since in the region $a_z \ll \sigma_x$ the transverse electric field of the bunch can be estimated like $E_\perp \simeq Ne\lambda/\sigma_x$, such crossings produce a longitudinal kick

$$\delta(\Delta p)\sim\sqrt{\frac{J_z}{\beta_z^*}}E_\perp,$$

which results in the contribution to the longitudinal tune shift increasing proportional to a_z.

The term Δ_2 in Eq.(21) directly describes an effect of the crossing at the angle (ϕ) on the tune shift of synchrotron oscillations. As seen from Eq.(23), in the region, where $r \ll 1$ and $a_z \ll \sigma_x$, this term can be calculated taking in the integrand $\sigma_z = 0$. Then, for a Gaussian linear density in the strong bunch the leading term of the expansion of Δ_2 in powers of a_z/σ_x reads

$$\Delta_2 \simeq 4\phi \frac{\eta R_0 \xi_z \sigma_z}{\beta_z^* \nu_s a_s} \int_0^{2\pi} \frac{d\psi_s}{2\pi} \cos\psi_s \int_{-\infty}^{\infty} \frac{du}{\sqrt{2\pi}} \exp\left[-2\left(u - \frac{a_s \cos\psi_s}{2\sigma_s}\right)^2\right] \times \int_0^{\infty} dk \sin\left(2ku\frac{\phi\sigma_s}{\sigma_x}\right) e^{-k^2/2}, \quad a_z \ll \sigma_x. \tag{29}$$

Direct calculation of integrals in this expression (see in Appendix B) results in

$$\Delta_2 \simeq \frac{\eta R_0}{\nu_s} \frac{Ne^2}{\pi p c a_s^2} \left[1 - \exp\left(-\frac{\phi^2 a_s^2}{2\Sigma_x^2}\right)\right], \quad \Sigma_x^2 = \sigma_x^2 + \phi^2 \sigma_s^2. \tag{30}$$

For oscillations with small amplitudes ($a_s \ll \sigma_s$) Eq.(30) yields

$$\Delta_2 \simeq \frac{\eta R_0}{\nu_s} \frac{\xi_z \epsilon_z}{4\beta_z^{*2}} 4 \frac{\sigma_x^2}{\Sigma_x^2} \frac{r\phi^2}{\theta_z^2}, \tag{31}$$

where $\theta_z = \sqrt{\epsilon_z/\beta_z^*}$ is the vertical rms angular divergency in the strong bunch. A comparison of Eqs(30) and (27) shows that the contribution from Δ_2 will dominate, if $\theta_z \ll \sqrt{r}\phi$. If, for example, $\sigma_x = 100\mu$m, $r = 0.01$, $\sigma_s = \beta_z^* = 1$ cm, which is typical for B-factory projects, we find that $\theta_z = 10^{-4}$ and that Δ_2 will exceed Δ_1 and Δ_3, if the crossing angle exceeds $\phi = 10^{-3}$.

4. Discussion

Collisions of flat bunches at the angle in the horizontal plane is accompanied by the excitation of both horizontal and vertical synchrobetatron resonances and, generally, may result in the blowup of the vertical beam size. These synchrobetatron resonances can be especially important for the tail particles of the bunch ($\phi a_s > \Sigma_x$). An accumulation of particles in the buckets of vertical oscillations near these resonances can saturate the luminosity of the collider, if the perturbation due to horizontal synchrobetatron resonances is small. If the perturbation due to horizontal synchrobetatron resonances is strong, such an accumulation will result in the decrease of the luminosity.

The dependence of the transverse beam-beam tune shifts on the amplitude of synchrotron oscillations and on the crossing angle generally vary the geometry of one-dimensional betatron resonances in the space of amplitudes of oscillations. No phase-convection is predicted for head-on collisions. However, near the upper side of the resonant stopbands the

damping of synchrotron oscillations may result in the storing of particles in the betatron tail region. For high crossing angles similar blowup in vertical direction happens due to the phase-convection effect. Such a variation in the geometry of resonant lines means that there is some optimum crossing angle, when the vertical tune shift does not depends on the amplitude of synchrotron oscillations, and when the damping of synchrotron oscillations has a little effect on the dynamics near betatron resonances.

The beam-beam tune shift of the synchrotron oscillations generally is contributed by the bunch waist, by the betatron angular spread in the weak bunch and by the crossing angle itself. The contributions from the bunch waist (Δ_1) and from the betatron angular spread decrease as the crossing angle increases. The contribution due to crossing angle collisions (Δ_2) saturates, when the crossing angle increases. For typical parameters of the future B-factories this contribution may dominate starting from very small crossing angles. However, until $a_x, a_z \ll \sigma_x\ \Delta_2$ does not depend on amplitudes of betatron oscillations. This tune shift (Δ_2) is proportional to the bunch current. For this reason, its effect must be analyzed together with perturbations due to longitudinal bunch wake fields.

The common effect of the phase-averaging and of the crossing at the angle substantially decreases the strengths of the vertical synchrobetatron resonances for flat colliding bunches. The reason is that the drop of the resonance strength due to crossing angle collisions compensates its increase due to mismatching between the beam-beam kick and the reaction of the betatron oscillations, which is specific for collisions of flat bunches.

A. Calculation of $V_{mn}^{(0)}$

The integral in Eq.(12) can be calculated expanding the Bessel function $J_{2k}(2v\sqrt{\chi})$ in the power series [10]

$$J_{2k}(2v\sqrt{\chi}) = (v^2\chi)^k \sum_{m=0}^{\infty} \frac{(-v^2\chi)^m}{m!(m+k)!}, \tag{A.1}$$

which results in

$$\int_0^{\infty} \frac{dve^{-v^2/2}}{v^2} J_{2k}(2v\sqrt{\chi}) = \frac{\Gamma(k-1/2)2^k}{\sqrt{2}\Gamma(2k+1)} \chi^k e^{2\chi} F(k+3/2, 2k+1, 2\chi), \tag{A.2}$$

where $F(\alpha, \gamma, z)$ is the confluent hypergeometric function. Using the identities [10]

$$F(\alpha+1, \gamma, z) = \left(1 + \frac{z}{\alpha}\frac{d}{dz}\right) F(\alpha, \gamma, z), \quad F(k+1/2, 2k+1, 2\chi) = \frac{2^k k!}{\chi^k} e^{\chi} I_k(\chi)$$

and

$$\frac{2^{2k-1}\Gamma(k+1/2)\Gamma(k)}{\Gamma(2k)} = \sqrt{\pi},$$

we obtain

$$\int_0^{\infty} \frac{dve^{-v^2/2}}{v^2} J_{2k}(2v\sqrt{\chi}) = \frac{k\sqrt{\pi/2}e^{-\chi}}{k^2 - 1/4} \left(I_k(\chi) + \frac{\chi[I_k(\chi) + I_{k+1}(\chi)]}{k+1/2} \right). \tag{A.3}$$

B. Calculation of integrals for Δ_2

Let us calculate the integrals in Eq.(29). After obvious substitution

$$u - \frac{a_s \cos\psi_s}{2\sigma_s} \to u$$

we rewrite the integrals over u and k in the form

$$\begin{aligned}
&\int_{-\infty}^{\infty} \frac{du}{\sqrt{2\pi}} e^{-2u^2} \int_0^{\infty} dk \sin\left(2ku\frac{\phi\sigma_s}{\sigma_x} + k\frac{\phi a_s}{\sigma_x}\cos\psi_s\right) e^{-k^2/2} \\
&= \int_0^{\infty} dk e^{-k^2/2} \sin\left(k\frac{\phi a_s}{\sigma_x}\cos\psi_s\right) \int_{-\infty}^{\infty} \frac{du}{\sqrt{2\pi}} e^{-2u^2} \cos\left(2ku\frac{\phi\sigma_s}{\sigma_x}\right) \\
&= \frac{1}{2}\int_0^{\infty} dk \exp\left(-\frac{k^2}{2}\frac{\Sigma_x^2}{\sigma_x^2}\right) \sin\left(k\frac{\phi a_s}{\sigma_x}\cos\psi_s\right).
\end{aligned}$$

Now, using

$$\int_0^{2\pi} \frac{d\psi}{2\pi} \cos\psi \sin(z\cos\psi) = J_1(z),$$

we obtain

$$\begin{aligned}
\Delta_2 &\simeq 2\frac{\eta R_0 \xi_z \sigma_z}{\beta_z^* \nu_s} \frac{\sigma_x}{a_s^2} \int_0^{\infty} dz J_1(z) \exp\left(-\frac{z^2}{2}\frac{\Sigma_x^2}{\phi^2 a_s^2}\right) \\
&\simeq 2\frac{\eta R_0 \xi_z \sigma_z}{\beta_z^* \nu_s} \frac{\sigma_x}{a_s^2} \left[1 - \frac{\Sigma_x^2}{\phi^2 a_s^2} \int_0^{\infty} dz J_0(z) \exp\left(-\frac{z^2}{2}\frac{\Sigma_x^2}{\phi^2 a_s^2}\right)\right] \\
&\simeq 2\frac{\eta R_0 \xi_z \sigma_z}{\beta_z^* \nu_s} \frac{\sigma_x}{a_s^2} \left[1 - \exp\left(-\frac{\phi^2 a_s^2}{2\Sigma_x^2}\right)\right].
\end{aligned}$$

References

[1] A. Piwinski. IEEE Trans on Nucl. Sci. **NS-24**, 1408, 1977.

[2] An Asymmetric B-Factory Based on PEP. Conceptual Design Report. LBL PUB-5303, SLAC-372, CALT-68-1715, UCRL-ID-106426, UC-IIRPA-91-01, 1991.

[3] Accelerator Design of the KEK B-factory. Ed. by S. Kurokawa, K. Satoh and E. Kikutani. KEK Report 90-24, 1991.

[4] S. Krishnagopal, R. Siemann. Phys.Rev. D **41**, 2312, 1990.

[5] N.S. Dikansky, P.M. Ivanov, D.V. Pestrikov, E.A. Simonov. In Procedings of the USA National Particle Accelerators Conference, San-Francisco May 1991, v.1, p. 523, 1991.

[6] N.S. Dikansky, D.V. Pestrikov. NIM, A 344, 286, 1994; Phase Averaging of the Beam-Beam Instability. KEK Preprint 93-7, 1993.

[7] D. Sagan, R. Siemann and S. Krishnagopal. In Proc of the 2nd European Particle Accelerator Conference, v. 2, p. 1649. Edittions Frontieres, 1990.

[8] D.V. Pestrikov. NIM, A 336, 427, 1993.

[9] W. Chou, A. Piwinski. In Proc. of the Conf. on B Factories, The State of the Art in Accelerators, Detectors and Physics. SLAC, 1992, p. 134.

[10] I.S. Gradsteyn, I.M. Ryzhik. Table of Integrals, Series and Products. Academic Press, New York, 1965.

[11] A. Gerasimov. Physica **D 41**, 89, 1990.

LIFETIME AND TAIL SIMULATIONS FOR BEAM-BEAM EFFECTS IN PEP-II B FACTORY*

D. N. Shatilov[a] and A. A. Zholents[b]
[a] Budker Institute of Nuclear Physics, 630090 Novosibirsk 90, Russia
[b] Center for Beam Physics, Accelerator and Fusion Research Division, Lawrence Berkeley Laboratory, University of California, Berkeley, CA 94720

Abstract

A fast tracking technique for doing beam tail simulations has been applied to a study of beam-beam effects in the SLAC/LBL/LLNL PEP-II B Factory. In particular, the dependence of beam lifetime and particle density distribution due to vacuum pressure, damping times, machine nonlinearity and parasitic crossings has been analyzed. Effects of accidental orbit separation and dispersion function at the interaction point (IP) have also been considered.

I. BEAM PARAMETERS AND MODEL

Beam and machine parameters for PEP-II B factory are described elsewhere [1]. For the sake of completeness, we reproduce in the Table I all parameters we need for a discussion of beam-beam effects. Our notation for most of the parameters has a standard and obvious meaning. Only a few definitions need explanation. In the PEP-II B factory, electron and positron bunches collide head-on at the IP. After the IP, beam orbits are magnetically separated in the horizontal plane. However, before entering its own vacuum pipe, each electron bunch and each positron bunch experiences four more interactions with other bunches of the opposite beam. We refer to these interactions as parasitic crossings (PC's). A parameter d_{sep} defines orbit separation at the first PC. Orbit separation at the remaining PCs is much larger and, consequently, the effect of beam-beam interactions at these PC is negligible. We will ignore them in our model and will consider only the first parasitic crossing on either side of the IP. Parameters $\Delta\nu_x$ and $\Delta\nu_y$ define horizontal and vertical betatron phase advance, in units of the betatron tune, from the main IP to the first PC.

A goal of our study was understanding the mechanisms leading to a beam lifetime limitation in electron-positron colliders. According to experimental observations [2], these mechanisms are fairly insensitive to particle density distribution in the beam core. Thus, a weak-strong model of beam-beam effects seems adequate to our task.

All our simulations were carried out with the beam-beam program LIFETRAC [3]. This program allows the following physics to be included in the simulation:

1. Beam-beam kick.
2. One turn, six-dimensional linear map.
3. Chromaticity up to the third order:

$$\nu_x = \nu_{0x} + C_x\delta + C_{xx}\delta^2 + C_{xxx}\delta^3$$

*Work supported by DOE under Contract DE-AC03-76SF00098 and by Budker INP of the Russian Academy of Science.

Table I
Beam parameters

	weak beam (e^+)	strong beam (e^-)
E [GeV]	3.1	9.0 [a]
ν_{0x}, ν_{0y}	34.57, 35.64	34.57, 35.64 [a]
ν_s	0.037	0.052 [a]
ξ_{0x}, ξ_{0y}	0.03, 0.03	0.03, 0.03 [a]
$\tau_{x,y}$ [turns]	7200, 7200	5014, 5014 [a]
τ_z [turns]	3600	2507 [a]
$\sigma_{\Delta p/p}$	0.80×10^{-3}	0.62×10^{-3} [a]
σ_z [cm]	1.0	1.0
ε_x [m×rad]	6.4×10^{-8}	4.8×10^{-8} [a]
ε_y [m×rad]	1.9×10^{-9}	1.4×10^{-9} [a]
	Main crossing	
$\beta^*_{x,y}$ [m]	0.50, 0.015	0.667, 0.02
$D^*_{x,y}$ [m]	0, 0	0, 0 [a]
σ^*_{0x}, σ^*_{0y} [μm]	177, 5.3 [a]	177, 5.3
	Parasitic crossing	
d_{sep} [mm]	3.5	
σ_x, σ_y [μm]	284, 223 [a]	243,167
$\Delta\nu_x$, $\Delta\nu_y$	0.143, 0.246	0.117, 0.245 [a]

[a] These parameters do not enter the weak-strong simulation

$$\nu_y = \nu_{0y} + C_y\delta + C_{yy}\delta^2 + C_{yyy}\delta^3.$$

Here $\delta = \Delta p/p$ and $C_x, C_{xx}, C_{xxx}, C_y, C_{yy}, C_{yyy}$ are parameters of chromaticity.

4. Machine nonlinearity in the form of an amplitude-dependent betatron tune:

$$\nu_x = \nu_{0x} + \varepsilon_x a_{xx} A_x^2 + \varepsilon_y a_{xy} A_y^2$$
$$\nu_y = \nu_{0y} + \varepsilon_x a_{xy} A_x^2 + \varepsilon_y a_{yy} A_y^2.$$

Here A_x and A_y are normalized amplitudes and a_{xx}, a_{xy} and a_{yy} are coefficients.

5. Elastic scattering on nuclei of the residual gas.
6. Parasitic crossings.
7. Dispersion functions at the IP and at the PC.
8. Slicing of a bunch with an arbitrary number of slices (typically, we use 5 pancake-like slices).
9. Orbit separation at the IP.

II. SIMULATION TECHNIQUE

The fast tracking technique developed in LIFETRAC [3] emerged from a concept proposed earlier in [4] and realized

later in [5]. It allows a determination of beam lifetime on a level of 10 hours with a statistical confidence of a few percent by tracking only about 10^7 particle-turns. Along with the lifetime, this technique is able to provide information on the particle density distribution in the beam tails.

The idea of the algorithm is based on the presence of a random component (such as quantum fluctuation noise) in the particle motion [4]. It turns out that a particle's trajectory in phase space depends only on current coordinates and momenta (and noise). A history of the particle's motion is irrelevant for its future trajectory. After accumulating rich statistics of a particle's motion in a certain region of phase space, one can ignore the exact knowledge of a particle trajectory in this region and replace it by statistical information. This information could contain particle coordinates and momenta recorded at the moment when the particle leaves the region. Then, each time the particle's trajectory goes inside that region, one can interrupt tracking and begin a new trajectory from one of the prerecorded points. By this technique, we force actual tracking to go on only in a region with poor statistics rather than tediously tracking in a region with well-defined statistics.

This algorithm was recently checked against 'brute-force' calculations performed with the program TRS [6] and we found excellent agreement in the results [7]. It is worth mentioning that the 'brute-force' calculations took 818 minutes of CPU time on a Cray-2S, while LIFETRAC reached the same accuracy in the tail distribution in 55 minutes of CPU time on a VAX-6610.

III. RESULTS

A result of the simulation of beam-beam effects in PEP-II for the nominal conditions without PC's is presented in Figure 1a. This plot (and other similar plots) shows particle distribution contours in amplitude space. The first contour corresponds to a particle density a factor $\sqrt{e}$ below the peak and all the following contours correspond to successive reduction with a factor of e. Amplitudes A_x, A_y are normalized amplitudes, i.e. $A_x = 1$ corresponds to a physical amplitude of $1\sigma_{0x}$ and $A_y = 1$ corresponds to a physical amplitude of $1\sigma_{0y}$.

The particle density distribution is obviously perturbed by nonlinear resonances $\ell\nu_x + m\nu_y + n\nu_s = k$. The identified resonances are shown by arrows. On top of each arrow we draw numbers, which correspond to the ℓ, m, n resonance identification. Particularly strong is the resonance $14\nu_x = k$. It is partly overlapped with some other resonances, which we were not able to identify.

For the lifetime determination we assumed a limiting aperture of $A_x = 10$ and $A_y = 25$. With that aperture we were not able to determine the lifetime, because it was very long. We interrupted calculations when the lifetime exceeded 8 years. We also did not find any blow-up of the beam core.

A. *Parasitic Crossings*

Adding PC's did not affect beam lifetime. It was still very long to be determined. But PC's did affect the beam

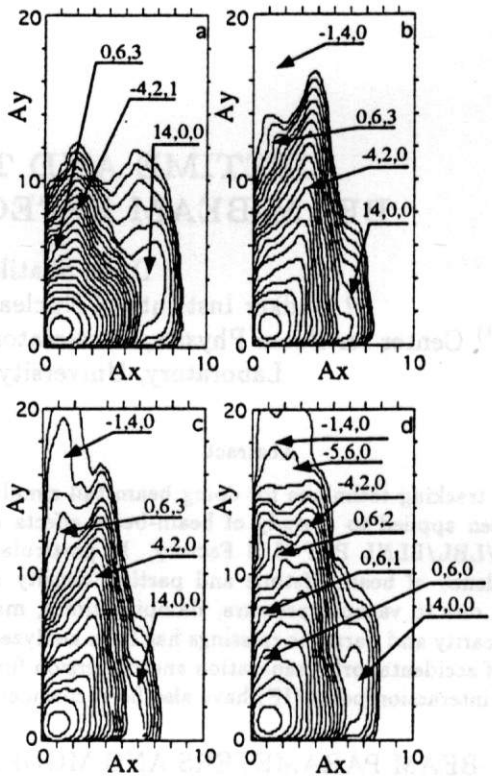

Figure. 1. Particle distribution contours: a) nominal case without parasitic crossings; b) the same as a) plus PC; c) the same as b) plus elastic scattering; d) the same as c), but with $\xi_{0x} = \xi_{0y} = 0.05$ and $a_{xx} = -200$ m^{-1}.

core (we found a 26% increase in the vertical beam size) and particle density distribution (see Figure 1b). The main factors giving rise to the effect of the PC's are strong resonances: $6\nu_y + 3\nu_s = k$ and $-4\nu_x + 2\nu_y = k$. At the same time, we found that resonances $-4\nu_x + 2\nu_y + \nu_s = k$ and $14\nu_x = k$ became weaker. This resonance restructuring is a result of a new beam footprint in tune space in the case with PC's.

B. *Vacuum*

Aside from beam-beam effects, the leading mechanism defining the beam lifetime in PEP-II on a level of 23 hours is elastic scattering on nuclei of the residual gas [1]. Since the beam-beam lifetime defined above is much larger, one might think that the beam-beam interaction will have no noticeable effect on the beam lifetime, but this is not right. The interference of beam-beam effects and elastic scattering could be significant. Imagine that the beam-beam interaction creates some resonance islands in phase space close to the aperture limit. Then, particles scattered inside these islands from the beam core, could be trapped there. As a result, the growing population of particles in the tails will decrease beam lifetime. This is exactly what we found when we included elastic scattering [3] in our sim-

ulation for PEP-II. The lifetime dropped from 22.9 hours (vacuum lifetime) to 16.7 hours. We attribute this to the elastic scattering into the resonance $-\nu_x + 4\nu_y = k$, which perturbs the particle density distribution at large vertical amplitudes (compare Figure 1c with Figure 1b).

C. Damping Time

We compared beam-beam effects for two damping times. First we used a damping time of 5400 turns as it is in [1]; second we took a damping time of 7200 turns, as proposed in [8]. In Figure 2, we show the dependence of the lifetime versus beam-beam parameters for our two cases. The difference between two cases is less than the statistical error expected in the calculations.

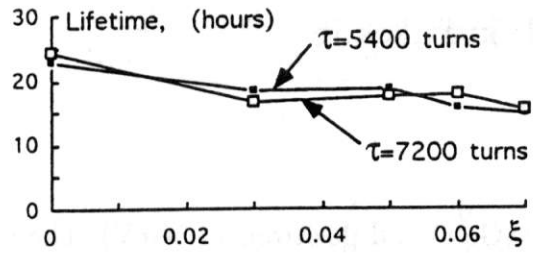

Figure. 2. Beam lifetime versus $\xi = \xi_{0x} = \xi_{0y}$ for two damping times. Arrows indicate damping time.

D. Machine Imperfections

In order to be more sensitive to the beam-beam effects, we did all the rest of our simulations with $\xi_{0x} = \xi_{0y} = 0.05$.

Chromaticity. We did not find any significant effect of chromaticity when we varied C_{xx}, C_{yy} in the range of ± 500 and C_{xxx}, C_{yyy} in the range of $\pm 10^4$, which are larger values than we anticipate for the machine.

Tune shifts with amplitude. In our notation, typical dependence of betatron tunes from amplitudes for PEP-II corresponds to a_{xx}=a_{yy}~-200m^{-1} and a_{xy}~-1000m^{-1} [9]. Simulations with these coefficients gave qualitatively similar results to those with zero nonlinearity. By adjusting a_{xx} with a_{yy}=a_{xy}=0 we could slightly increase the strength of the resonance $14\nu_x = k$ at a_{xx}=-200m^{-1} or significantly reduce it at a_{xx}=400m^{-1} (compare Figure 1d and Figure 3a), but both the beam lifetime and the beam core remained fairly insensitive to this change. For the rest of the simulations we used a_{xx}=-200m^{-1}.

Orbit separation at the IP. Table II contain all results. One can see that only the vertical beam size was sensitive to the orbit separation Δx, Δy.

Dispersion at the IP. Simulations with non-zero horizontal and vertical dispersions at the IP showed that the lifetime began to drop below 10 hours when $D_x^* \geq 4$ cm or $D_y^* \geq 0.5$ cm. An example with $D_y^* = 0.53$ cm is shown in the Figure 3b. Moreover, we found that a dispersion $D_x^* = 2.2$ cm already reduced the lifetime below 10 hours when combined with an accidental orbit separation of $\Delta x/\sigma_{0x}^* = 0.4$.

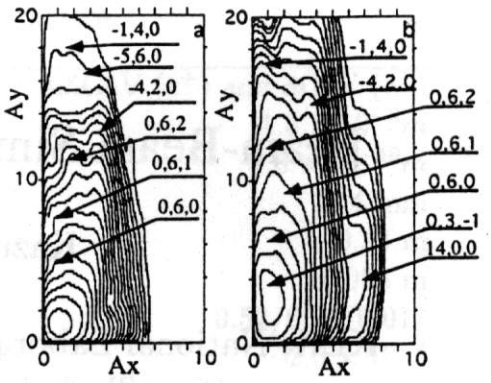

Figure. 3. Particle distribution contours: a) the same as Figure 1d, but with a_{xx}=$400\ \text{m}^{-1}$; b) the same as Figure 1d plus $D_y^* = 0.53$ cm.

Table II
Orbit separation

$\Delta x/\sigma_{0x}^*$	$\Delta y/\sigma_{0y}^*$	$\sqrt{x^2}/\sigma_{0x}^*$	$\sqrt{y^2}/\sigma_{0y}^*$	Lifetime,[h]
0	0	1.10	1.46	18.9
0.2	0	1.07	1.71	18.4
0.4	0	1.12	1.93	18.4
0	0.2	1.07	1.99	19.9
0	0.4	1.07	2.57	18.6

IV. Conclusion

Our study demonstrated that beam-beam effects should not affect the performance of the PEP-II B factory if $\xi_{0x} = \xi_{0y} = 0.03$. We did not find significant reduction in the beam lifetime even for larger beam-beam parameter, but we did see in many occasions a large increase in the vertical beam size.

Acknowledgment. We are grateful to M. Furman and M. Zisman for many useful discussions.

References

[1] PEP-II Design Report, SLAC-Report-418, 1993.
[2] A. Temnykh, Third Advance ICFA Beam Dynamics Workshop, INP, Novosibirsk, 1989, p.5.
[3] D.Shatilov, Preprint BINP 92-79, Novosibirsk, 1992, (in russian), unpublished.
[4] J. Irwin, ref.2, p.123.
[5] T. Chen et al., Phys. Rev. E49, 1994, p.2323.
[6] J. Tennyson, unpublished code 'TRS', 1989.
[7] M. Furman et al., CBP Note-59 (1995).
[8] J. Heim et al., Wiggler Insertion of the PEP-II B Factory LER, these proceedings.
[9] E. Forest et al., EPAC 1994, London, 1994, p.1033.

BEAM-BEAM SIMULATIONS AT LARGE AMPLITUDES AND LIFETIME DETERMINATION

Dmitry Shatilov
Budker Institute of Nuclear Physics (BINP), 630090 Novosibirsk, Russia
E-mail: Shatilov@inp.nsk.su

I. INTRODUCTION

We study incoherent beam-beam effects. Strong nonlinearity of the interaction leads to resonances and stochasticity, so that the behavior of the particles in the phase space becomes very complicated for analytical estimations. This is the reason for a wide employment of computer simulation for studying the beam-beam effects.

The perturbations of the equilibrium distribution can be conventionally divided into two parts: the perturbations at small amplitudes (core region) and the ones at large amplitudes (tails). The first cause an emittance growth, the second result in the lifetime decrease. Both effects restrict the beam current and, therefore, the luminosity, but the connection between them is rather weak. This means that one can have a strong beam size growth with a very good lifetime and vice versa, a bad lifetime with almost an unperturbed core region. The lifetime determination is the most difficult problem here, because a huge CPU time is required to correctly determine the distribution in the tails. Besides, almost all the CPU time is spent for improving core distribution. Such situation motivates the search for possibility of "CPU redistribution" for large amplitudes. Naturally, the question of accuracy arises since the tracking algorithm is changed artificially. Maintaining accuracy is the main problem we shall discuss below.

The base idea of the technique described below has been proposed in 1989 by J. Irwin[1]. It was developed later by T. Chen, J. Irwin and R. Siemann[9]. In INP this concept was developed independently by the author. Actually, this paper is a simple translation of the preprint INP 92-79 (in russian[7]). It should be noticed, that justification and realization of Chen et al's and the author's methods are rather different, although recently carried out comparison indicated good agreement between both of them and the brute force technique.

The method was developed for the "weak-strong" case, but this limitation is not so important and after a simple modification it can be used for the "strong-strong" case as well.

II. DESCRIPTION OF THE METHOD

There are different ways to simulate the equilibrium distribution of the beam particles. The first one, the ensemble of N independent particles is considered. If the simulation time is much greater than the damping time, the initial positions of these particles do not matter. Otherwise, they will influence the results and one has to care about correct initialization. Another way is watching for a single particle only. If the simulation time here is chosen N times greater than in the first case, both of them become equivalent, but there is no the initialization problem in the last one. For future discussion it does not matter which way is used, but for definiteness we consider a single particle for a long time (hundreds of damping times).

Besides coordinates and momenta, we use normalized amplitudes and phases as well:

$$x_\beta = \sigma_{\beta x} A_x \cos\varphi_x \qquad x'_\beta = \frac{\sigma_{\beta x}}{\beta_x} A_x (\sin\varphi_x + \alpha_x \cos\varphi_x) \quad (1)$$

$$z_\beta = \sigma_{\beta z} A_z \cos\varphi_z \qquad z'_\beta = \frac{\sigma_{\beta z}}{\beta_z} A_z (\sin\varphi_z + \alpha_z \cos\varphi_z) \quad (2)$$

$$s = \sigma_l A_s \cos\varphi_s \qquad \frac{\Delta E}{E_0} = \frac{\sigma_E}{E_0} A_s \sin\varphi_s \quad (3)$$

Here all the parameters (σ, β, α) are related to an unperturbed beam. During simulation, the particle moves along a very complicated trajectory within a 6-dimensional phase space. The equilibrium distribution and the density of the flows in this space are the most complete information one can extract, but not all of it is of equal importance. The distribution in the space of amplitudes is much more important because the amplitudes are "slow" variables. The amplitudes define the nonlinear tune shifts and, therefore, the falling within a resonance. The distribution in the space of phases is not so informative since the phases are "quick" variables, but this distribution is also important for the motion within resonances. As far as the flows are concerned, the most important one is the flow to the aperture (which is defined as the limit values of the amplitudes). This flow, not the distribution in the tails, defines the lifetime, though there is a connection between these two.

For the sake of simplicity, let us consider the two-dimensional case (four-dimensional phase space). The three-dimensional case will be discussed separately in section IV. We observe the test particle and locate its position in the plane of amplitudes at certain moments each turn (at the Interaction Point), so its motion looks like "jumps" from point to point. These jumps are produced by damping, noise and kicks from the opposite beam. The lattice nonlinearity, if any, also makes a contribution.

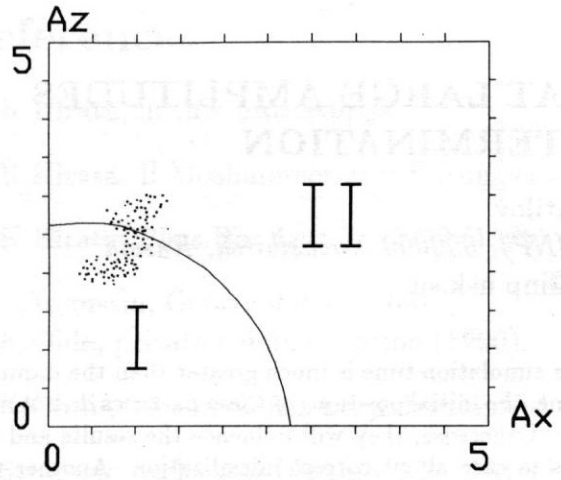

Figure. 1. A plane of amplitudes is split into internal (I) and external (II) regions. A small piece of the particle's trajectory is shown by points.

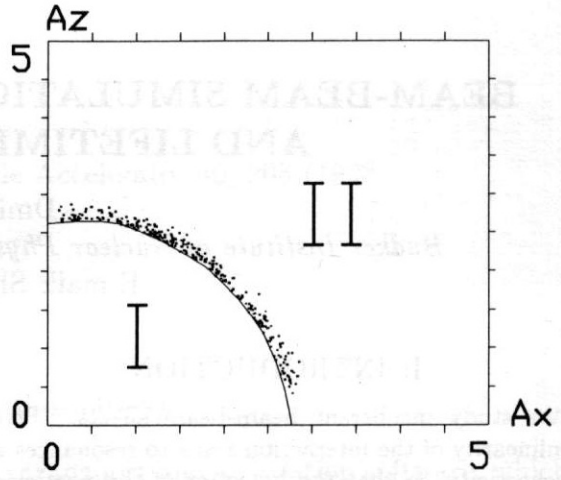

Figure. 2. The outflights are shown by points, which form a specific halo above a boundary. In future these points will be used as the positions for restarts.

Now we draw a special line, or boundary, to split the amplitude plane into two parts: *internal* (I) and *external* (II) (see Fig. 1). During the first step of the new algorithm we record all particle's coordinates and momenta each time it leaves the internal region for the external one (at once after crossing the boundary). These points (we call them *outflights*) form an original halo above the boundary (see Fig. 2). After some time, we get enough statistics of such outflights to proceed to the next step. Let us imagine that the internal region becomes a "black box" (or *hidden* region), so that we cannot watch a particle within it. In this case, the particle's trajectory looks like a large number of completely independent pieces, which starts from the points of outflights and ends when the particle falls into the hidden region. During the second step, we put the test particle to one of the outflight points immediately when it leaves for the hidden region. Such a procedure is called *restart*. The points for the restarts are chosen from the complete outflights statistics by using a random number generator.

It should be noted that this algorithm violates the course of events with time. This means that the observer is able to distinguish a real trajectory from our simulation. The reason is as follows: when the particle falls into the hidden region, it spends some time near the boundary and there is a high probability of crossing the boundary many times in close proximity to this place. In other words, the outflights are usually made by local groups, before the particle goes away from the boundary. This means that there is a correlation between the location of outflights and the time, when they take place. But this correlation vanishes since we use a random number generator to choose the points for restarts. Luckily, such rearrangement of events in time has no influence on the motion characteristics: we obtain quite correct distribution and flows in the phase space during the second step. The reason is that the process under consideration is a Markovian process (without memory). The particle's behavior does not depend on its history, and since we reproduce the probability of falling into a certain cell of the phase space when the particle leaves the hidden region, we must obtain the correct density and flows within this space.

Now it is easy to understand how to proceed to large amplitudes. After completion of the first step the regions change their meaning: the internal region becomes hidden, and the next boundary is drawn to split the "old" external region into internal and external ones (see Fig. 3). During the second step the position of the particle is checked each turn. As soon as it leaves for the hidden (I) region, a restart is produced. In case it moves from the internal region (II) to the external one (III), all its coordinates and momenta are registered to accumulate the statistics of outflights across the second boundary. Later on, we call the boundary between the hidden and internal regions as R-boundary (boundary for restarts); the boundary between the internal and external regions we call C-boundary (boundary for crossings). For the third step, the regions I and II are joined to form the new hidden region (so the C-boundary becomes the R-boundary), and the third boundary (it is the C-boundary for the third step) is drawn to split region III into the internal and external regions (their numbers are III and IV, respectively), and so on. The reduction of CPU time can be calculated as a ratio between the number of restarts and the number of corresponding outflights. Usually this value is about 5–10 for each step.

Approximately in this form this technique has been already suggested by J. Irwin[1]. He used simple circular arcs as boundaries and the radius of the arc was chosen so that particles spent 90% of the CPU time in the internal region and 10% in the external one.

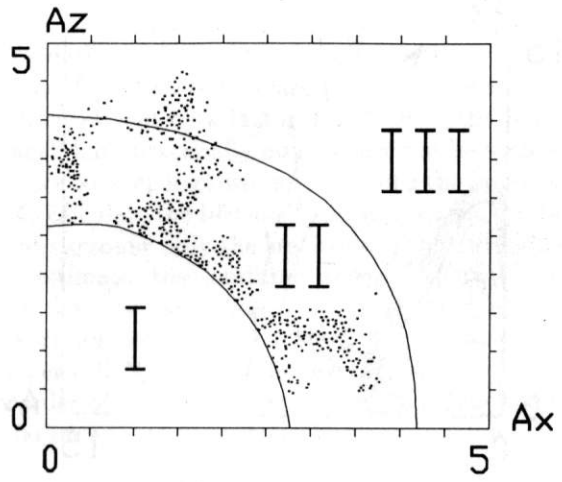

Figure. 3. The particle's trajectory during the second step, consisting of a large number independent pieces. I — hidden, II — internal, III — external regions.

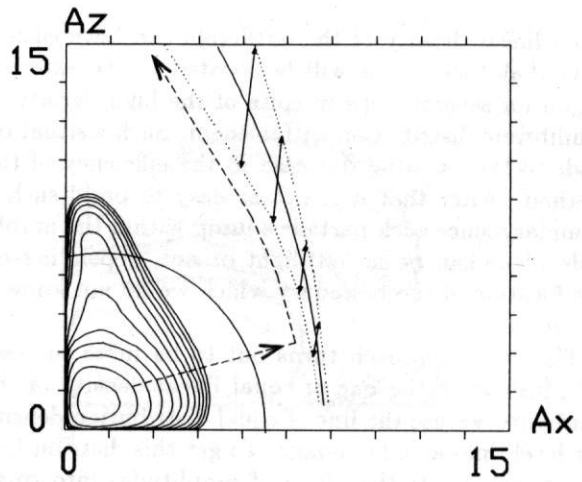

Figure. 4. An example of location of the boundary which leads to a loss of accuracy. The most probable way of a particle going to the aperture is shown by dashed line.

This solution is very attractive due to its simplicity and can give good result, but sometimes loss of accuracy is possible in the case where the lifetime is calculated. Maintaining accuracy is the main problem here. The difficulties result from our wish to develop a universal method which must work correctly for systems with very different (practically arbitrary) "phase space portraits".

Rigorously speaking, the only source of errors is the incorrect (insufficient) statistics of outflights from the hidden region. However, the accuracy of the results depends on many factors: simulation time, damping times, shape and location of boundaries within the amplitude plane. It is easy to guess that there is direct connection between the accuracy and the decrease in the CPU time this method provides. The accuracy can be increased at the expense of efficiency, for example, by increasing the simulation time for each step and decreasing the distance between the boundaries. The aim is to achieve an optimal compromise here: to get high efficiency with good enough guaranteed accuracy.

The amplitude of noise measured in units of normalized amplitude is defined by the damping time according to the formula:

$$\delta_A = 2\sqrt{\alpha}. \qquad (4)$$

Here α is the damping decrement and δ_A is the r.m.s. of amplitude change due to noise after a single turn. Without loss of generality, we can assume a Gaussian distribution for kicks caused by the noise. The damping time (in units of revolution time) is defined as $1/\alpha$ and this is a natural time scale of the system. The damping times are different for different degrees of freedom, but all of them are of the same order of magnitude. The largest one is denoted by τ and the simulation time for each step, measured in units of τ, is denoted by T (we assume it to be approximately the same from step to step).

Now let us consider the example shown in Fig. 4 to understand the influence of the shape and location of the boundaries. Here we can see two strong resonances disturbing substantially the equilibrium distribution. The first one is located at small amplitudes (it is shown as the disturbance of lines of equal density). The second one (shown as resonance line and resonance vectors) plays a main role in the process of losing particles at the aperture. The dashed line shows the Most Probable Way of a particle going to the Aperture (MPWA): first of all it moves to the second resonance (due to the noise only), is captured in it, and then moves to the high amplitudes along the resonance by streaming[2]. The first resonance leads to a very strong change in the density (several orders of magnitude) along the boundary which is chosen as a circular arc. As a result, since the simulation time is finite, all the outflights across this boundary are concentrated at the place where the boundary crosses the first resonance. This means that there are no outflights in the region where the MPWA is located. So, we lose this path for all following steps and the error in the lifetime determination can reach several orders of magnitude! By increasing the simulation time, we can get few outflights in the direction we need, but the insufficient statistics of such events leads to incorrect probability for this process and the accuracy of lifetime determination will not be good enough.

What is the optimal shape of the boundary? On the face of it, the main condition is the equal linear density of the outflights along the boundary. Indeed, a large number of outflights under this condition prevents from the above situations. Nevertheless, this choice has some essential disadvantages. First of all, it does not perfectly correspond to our goal of moving to large amplitudes because there is a possibility of forming spacious areas at small amplitudes with very weak flows out from the core. As a result, the line of

equal linear density of the outflights can have such a form that these areas will be located in the external region for several steps in spite of the high density of equilibrium distribution within them. Such a situation leads to the essential decrease in the efficiency of the method. After that it is not so easy to build such a boundary since each particle's jump within the amplitude plane can be an outflight or not, depending on the location of the boundary which we do not know a priori.

The other approach turns out to be more successful. Instead of the line of equal linear density of the outflights, we use the line of equal distribution density (or level line) as a boundary. To get this distribution, we should divide the plane of amplitudes into small rectangular cells (it is convenient to use cells of size δ_A). During the simulation we will account (individually for each step) how many times a test particle falls within each cell. After completion of the step, we will have an array of such numbers (N_p), which describe the equilibrium distribution outside the hidden region. The dispersion of N_p along the C-boundary must be sufficiently small since the boundary was chosen as a level line. The mean value of N_p on the C-boundary is marked by a tilde. It can be affirmed that the main condition, we must satisfy to get good statistics and solve our problems, is

$$\widetilde{N}_p \geq \overline{N} \gg 1, \qquad (5)$$

where $\overline{N}$ is the constant (to be defined below), while $\widetilde{N}_p$ can vary from step to step. Indeed, on the one hand, this condition guarantees the representation of all the details of the "phase space portrait" since these details cannot be greater than δ_A. In other words, this is a criterion of statistical reliability of the obtained level lines. On the other hand, for the next step we will get a high value of N_p along all the border of the hidden region (or R-boundary). This means that we reproduce correctly the probability of any particle's "journey" which begins inside the hidden region and crosses the area with the high "density" N_p. It is worth of noting two important details: $\widetilde{N}_p$ keeps approximately the same value from step to step and the simulation time T, necessary to satisfy condition $\widetilde{N}_p \geq \overline{N}$, does not depend on the damping time τ for the two-dimensional case.

Let us consider now Fig. 5, in which the situation similar to Fig. 4 is shown. Here the dotted lines show the flows of phase convection, which result in almost all the outflights located at a certain place in spite of the boundary (bold) is a level line. The MPWA is connected with capture in the second resonance and streaming along it, as well as in Fig. 4. As is seen, the short way from the core to this resonance is improbable. Nevertheless, even if there is a "channel" crossing the boundary at the place where no outflights have been obtained, during the next step we reproduce the probability of getting to this channel correctly since

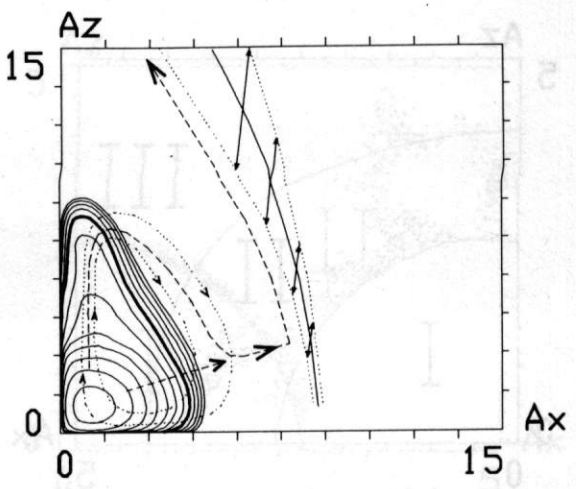

Figure. 5. The boundary (bold) coincides with a level line. Nevertheless, almost all the outflights are concentrated at a certain place due to the convective flows (dotted). The short dashed line shows a possible (but improbable) channel of going away. Since this channel crosses the area with high value of N_p, we correctly reproduce the probability of getting to it.

the value of N_p around the hidden region is sufficiently high (at least several times greater than $\overline{N}$).

It is convenient to measure the distance between the boundaries through the logarithm of density change. Indeed, any boundary can be defined by a single value, i.e., the number of the corresponding level. Let us introduce for each step an individual reference system of levels Q_i in which they are read from the border of hidden region. So, the level $Q_i = 0$ corresponds to the R-boundary for the i-th step, the level $Q_i = k$ corresponds to the density $\exp(k)$ times less than the density at the level $Q_i = 0$, and so on. In these terms, the distance between the neighboring boundaries j and $(j+1)$ (i.e. R- and C-boundaries for the $(j+1)$-th step) is just a value of Q_j at the boundary $(j+1)$. In future these distances are assumed to be equal to the same constant q for all the steps. Now we have to understand what the values q and the simulation time for each step T must be. We should keep in mind the following:

- The condition $\widetilde{N}_p \geq \overline{N}$ must be satisfied, otherwise we will get a wrong distribution. This means that with the distance between boundaries q, the value of T must also increase exponentially.
- The value of N_p obtained in time T at the level q depends on the shape of equilibrium distribution, so we cannot know it a priori.
- We need a lot of the outflights. If the boundaries are chosen correctly, as it was described above, the accuracy of the lifetime is determined by the statistics of the outflights. We can estimate it as $\sqrt{C_g/C}$, where C is the number of outflights and C_g is the mean number of outflights within a group (as a rule the outflights occur by local groups, which we can consider as the particular events).

- Deviations of the boundary from the true level line, if they are not so large (the true density data disagreement by a factor of 2–3 along the boundary), have practically no influence on the accuracy since we keep high value of N_p along the boundary. To calculate the lifetime accuracy, we need to take into account only the statistics of the outflights.

To estimate the optimal distance between the boundaries, the same time $T = T_0$ is assumed to be necessary for each step to achieve the number of particles per cell $N_p = \overline{N}$ at the level $Q_i = 0$ (just above the border of the hidden region). In this case, the full simulation time to move to m levels is as follows:

$$t = \frac{m}{q} T_0 \exp(q). \tag{6}$$

Here m/q is the number of steps and $T_0 \exp(q) = T$ is the simulation time for each step to achieve $N_p = \overline{N}$ at the level $Q_i = q$. We have to set $q = 1$ to minimize the time t. This means that the density falls down by a factor of e between the boundaries. Pay attention to that in this case we optimize q without taking into consideration the accuracy of the lifetime, which is defined through the statistics of the outflights. Fixing the final accuracy of the lifetime, we get the other expression for q. Indeed, on each step we have a statistical error of the outflights $\sqrt{C_g/C} \ll 1$. Since we follow the rules of building boundaries, the accuracy of the lifetime can be estimated as $(m/q)\sqrt{C_g/C}$. Here we assume (for estimation only) the equal number of the outflights across each boundary if $\widetilde{N}_p$ keeps the same value from step to step. So, the simulation time T is proportional to the square of the number of steps and for the full time we get

$$t \sim \frac{\exp(q)}{q^3}. \tag{7}$$

In this case, the minimum is achieved at $q = 3$.

To estimate the value of T_0, let us consider an unperturbed beam. The equilibrium distribution density (including the phase volume) is represented by the equation

$$\rho(A_x, A_z) = A_x A_z \exp(-\frac{A_x^2 + A_z^2}{2}). \tag{8}$$

The maximum density, which is equal to $1/e$, is achieved at the point $A_x = A_z = 1$. The number of particle's falling within a cell of size δ_A at the point (1,1) is $N_p = 4T_0/e$ (we assume here the same damping decrements for both directions). Defining the value of $\overline{N} = 100$, we get $T_0 \approx 70$.

Practically, the distance between the boundaries is chosen as $q = 2.5$. Under this condition, the simulation time must be $T \sim 1000$ damping times for each step. The determination of the lifetime of several hours takes usually 6–8 steps and even if the accuracy of the outflight statistics is 5% for each step, we obtain a final lifetime accuracy of 50% or better, which seems to be good enough.

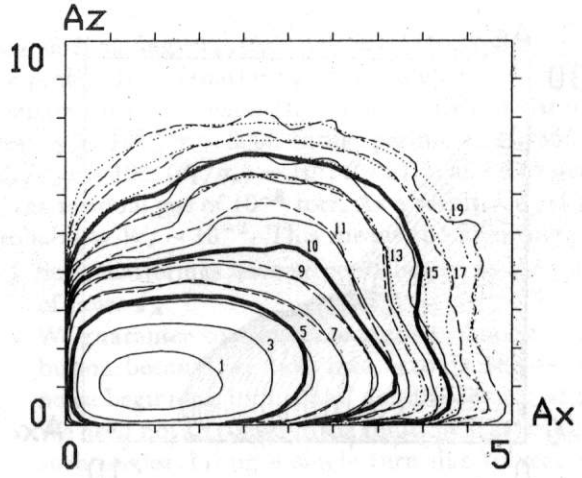

Figure. 6. The level lines obtained during three sequential steps (1 — solid, 2 — dashed, 3 — dotted) are shown. Increasing of the line number by two corresponds to the equilibrium density decreasing by a factor of e. Boundaries (5, 10, 15) are shown as bold.

An important advantage of the method is the possibility of controlling the accuracy during the simulation: we can vary the simulation time T from step to step in such a way that the necessary value of $\widetilde{N}_p$ and number of outflights are achieved. Moreover, we can get the knowledge of the accuracy of the method directly from the results (see Fig. 6). Here we can see the level lines obtained from several sequential steps and three boundaries. The first step actually consists of two parts which can be called "zero" step and the first step itself. The zero step is necessary to obtain the initial distribution at small amplitudes and to draw the first boundary. During the first step we get the outflights across this boundary and improve the statistics of the distribution, so the first boundary will not exactly correspond to the final level line $Q_1 = q$. The second boundary is built after completion of the first step and goes along the level line $Q_1 = 2q$. After completion of the second step, we get the new lines (dashed, see Fig. 6) which have the statistical reliability much better than the same lines on the first step. Nevertheless, close to the first boundary they are in good agreement, which means that both sets are reliable here. When going away from the first boundary to large amplitudes, the differences between the two sets of lines grow. This is a consequence of the insufficient statistics at large amplitudes after completion of the first step. As we can see, the second boundary has been determined well enough since it is close to the level line $Q_2 = q$ obtained after completion of the second step, as well as the third boundary ($Q_2 = 2q$) which was built after the second step is close to the level line $Q_3 = q$ obtained after completion of the third step (dotted lines in Fig. 6).

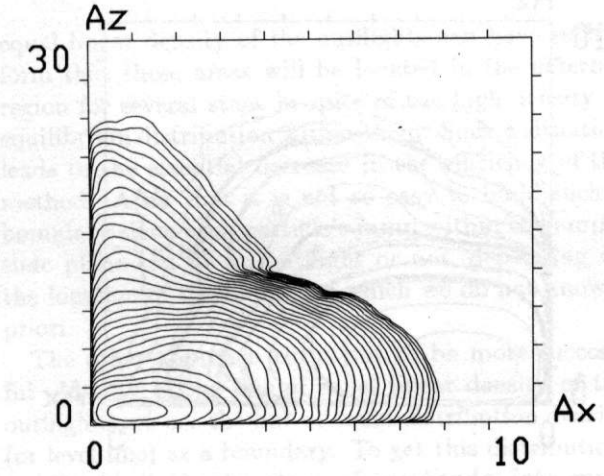

Figure. 7. The final level lines (see also Fig. 6) for the working point: $\{Q_x\} = 0.545$, $\{Q_z\} = 0.575$, $Q_s = 0.02$, $\xi_x = 0.005$, $\xi_z = 0.06$, $\sigma_x/\sigma_z = 1000$, $\sigma_l/\beta_z = 0.5$. The equilibrium density changes by a factor of e from line to line. The results of eleven sequential steps are used. The benefit in the CPU time was $\sim 10^8$.

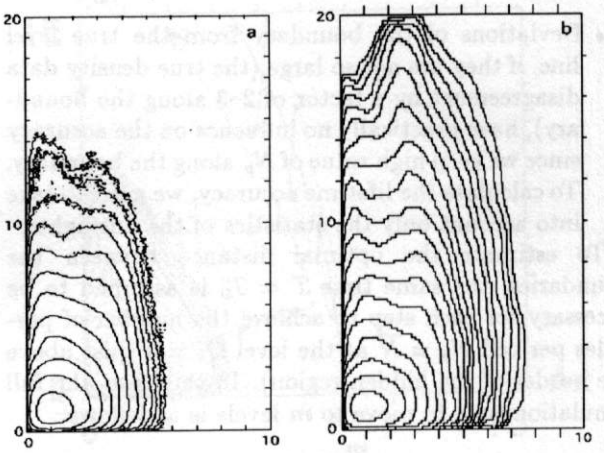

Figure. 8. The two-dimensional amplitude distribution for PEP-II B-factory working point. (a): TRS, brute force technique; (b): LIFETRAC, proposed technique.

The final level lines for this working point are shown in Fig. 7. In the core region the results of the first step are used. Between the first and the second boundaries the results of the second step are used. Between the second and the third boundaries we use the results of the third step, and so on. As is seen, the advance to large amplitudes takes place in the regions, where the equilibrium density of distribution was defined well enough during the previous step. This condition ensures good "sewing" of all the steps.

Obviously, the decisive test of the technique validity can be only get from the comparison against the brute force technique. Recently such a comparison has been carried out for three beam-beam codes[11]:

- TRS[10] is a multiparticle strong-strong code, which does brute force tracking.
- LIFETRAC[7] is a weak-strong code, which uses the described above tracking technique.
- LFM[9] is a weak-strong code, which uses tracking algorithm similar (but not identical) to LIFETRAC.

The two-dimensional amplitude distributions for PEP-II B-factory working point[11] are shown in Fig. 8. The results from TRS correspond to $5 \cdot 10^9$ particle-turns and took 818 CPU minutes to run on Cray-2S/8128. The results from LIFETRAC correspond to an effective number of $4 \cdot 10^{11}$ particle-turns and took 100 CPU minutes on VAX-6610 computer. The results from LFM are similar to the ones from LIFETRAC (see Tech. Note[11] for more information). The agreement among the codes is quite good. We hope that the next comparisons will be performed and will stimulate the progress in the tracking techniques.

In conclusion we discuss what the maximum amplitudes we can "climb" using this method are. Up to now we assumed the uniform density within a cell of size δ_A. However, at high amplitudes the level lines join together so close that this condition is violated. This means that we need the other criteria for the necessary value of $\widetilde{N}_p$ and the final lifetime accuracy (maybe, the simulation time shall increase with the increase in the step number). But we do not go deep into this problem, because it is not important for practical purposes. Indeed, the typical value of the damping time for e^+e^- colliders is about $10^3 - 10^4$ turns, which corresponds to the amplitude of noise $\delta_A \leq 1/30$. So, even for the unperturbed distribution the distance between the neighboring levels remains greater than δ_A up to the amplitudes $A \sim 30$, which is usually greater than the real aperture limit.

III. SCATTERING ON THE RESIDUAL GAS

Scattering has an essential influence on the equilibrium distribution, especially at large amplitudes. Just scattering defines the lifetime without an opposite beam. If both the beam-beam interaction and scattering occur, the interference between these two perturbations can have an effect. For example, if a strong resonance is located on large amplitudes, the scattering can essentially increase the probability of particle achieving it, providing particle's falling within the resonance directly from the core. So, including the scattering into simulation seems to be useful and important, but this is not possible directly in the new method. To clarify the problem, let us consider the elastic scattering without beam-beam effects. The scattering angle is inversely proportional to the impact parameter, so the probability of getting the amplitude jump ΔA is inversely proportional to the magnitude of this jump. Without scattering, the equilibrium density decreases as $\exp(-A^2/2)$. Hence, it can be seen that, beginning

from a certain value of the amplitude, the distribution is defined only by a single scattering from the core region. In our method this core turns out to be inside the first boundary, and scattering to large amplitudes can be considered as a particular case of the outflight. Although this process plays a main role for the distribution at high amplitudes, its probability is very small and we may get no such specific outflights in time T during the first step. This means that we lose the way of going to large amplitudes for all the next steps, as in the case shown in Fig. 4.

Nevertheless, slight modification of the technique allows us to successfully include the scattering. The idea is to simulate the scattering from the hidden region independently of the outflights statistics. We can do it correctly because we know the distribution inside this region.

Before discussing this technique, we would like to consider in detail the ordinary scattering outside the hidden region. We take into account only the elastic scattering because it has a greater influence on the equilibrium distribution (inelastic scattering is very important for lifetime definition, but actually it does not disturb the equilibrium distribution since almost all the particles lose immediately after such scattering). The cross-section for $\gamma \gg 1$ and $\theta \ll 1$ is classical:

$$d\sigma = 4Z^2 \frac{r_e^2}{\gamma^2} \cdot \frac{\mathrm{o}}{\theta^4}, \tag{9}$$

whence

$$\theta = 2Z \frac{r_e}{\gamma\rho}. \tag{10}$$

Here Z is the nucleus charge, θ is the scattering angle, ρ is the impact parameter, o is solid angle. Each act of the scattering causes the change of momenta of the electron which can be written in normalized variables as follows:

$$\Delta p_x = \frac{\beta_x}{\sigma_x} \cdot \theta \cos\varphi, \tag{11}$$

$$\Delta p_z = \frac{\beta_z}{\sigma_z} \cdot \theta \sin\varphi. \tag{12}$$

Here φ is the angle between the horizontal and scattering planes. It follows that the elastic scattering, as well as the beam-beam effects, mainly disturbs the vertical distribution (for flat beams) due to the relation $\beta_z/\sigma_z \gg \beta_x/\sigma_x$. The scattering at small angles, when repeated many times, results in small normal (Gaussian) noise which can be combined with quantum fluctuations of synchrotron radiation into certain common noise defining the beam sizes. A special approach must be applied to scattering at amplitudes comparable with δ_A or greater, on which strong perturbations of noise distribution arise (we can consider scattering as a specific noise with very long tails).

Thus, we simulate only the scattering at the angles greater than a certain angle. As a border value, we take such an angle θ_0, that $\Delta p_z = \delta_A/10$, and estimate the probability of scattering at the angle $\theta \geq \theta_0$ during a single turn. For example, we use VEPP-4 parameters: $\gamma = 10^4$, $\tau \sim 3000$ turns, perimeter P=366 m, $\langle\beta_x/\sigma_x\rangle \sim 10^4$, $\langle\beta_z/\sigma_z\rangle \sim 10^5$, $Z = 7.5$, and a pressure of the residual gas of 10^{-8} torr. As a result, we get the probability $W_s \sim 10^{-2}$. This means the following:

- Such scatterings have no contribution to the r.m.s. of noise δ_A.
- We guarantee correct reproduction of noise distribution because we take into account the tails of noise beginning from small amplitudes $\Delta p \ll \delta_A$.
- We need not to consider the multiple scattering on such angles during a single turn due to very low probability of these events.
- The increase in the CPU time due to simulation of the above scatterings is insignificant.

The simulation with account of scattering (outside the hidden region) is now as follows: first of all, the probability of scattering at the angles $\theta \geq \theta_0$ is calculated using parameters of the ring. During the simulation, a random number generator is used at each turn to decide whether the scattering occurs. If yes, the particular angle is defined according to the formula

$$\theta = \theta_0/\sqrt{R}, \qquad 0 < R < 1, \tag{13}$$

where R is the other random number. The third random number is used then to define the scattering plane inclination angle φ and the fourth random number to define the azimuth of the collider on which the scattering takes place. To calculate the jumps in the normalized momenta, we have to multiply the obtained values of θ_x and θ_z with the corresponding relations β_x/σ_x, β_z/σ_z taken at the scattering point. In practice, the mean values of these relations are used, although a real lattice and distribution of ions along the ring (it can be quite different for different places) can be readily taken into consideration.

Now we come back to the scattering from the hidden region. When a particle falls inside, it has exactly three possibilities at each turn, one of them is realized without fail:

1) The particle leaves the hidden region without scattering (ordinary outflight).

2) The particle is scattered at the angle $\theta \geq \theta_0$. As a result, it can leave the hidden region (a particular case of the outflight), and can remain inside as well.

3) The particle is not scattered and remains inside the hidden region.

The latter case is the most probable, and the essence of the above-described method is the consideration of only such events, where the particle leaves the hidden region without spending the CPU time for the third case. Now we only should take into account one more possibility of leaving the hidden region due to scatter-

ing. To reproduce this process correctly, the probability of the first case is necessary.

The algorithm of simulation is now as follows: during the first step (see Fig. 1), in time T_1, we get a number of the outflights C_1 which can be divided into two parts: the outflights with scattering (C_{1s}) and the ones without it (C_{1r}). So, we have $C_1 = C_{1s} + C_{1r}$ and only the last events are saved as positions for future restarts. Besides, the fraction of time the particle has spent in the external region $V_1 < 1$ is accounted. On the second step (see Fig. 3), the probability of leaving the hidden region without scattering during a single turn is

$$W_1 = \frac{C_{1r}}{(1 - V_1) \cdot T_1 \cdot \tau}. \tag{14}$$

Here the denominator is the number of turns the particle has spent within the internal region on the first step. The process of leaving is simulated in the following way: using a random number generator, we decide, according to the probabilities W_1 and W_s, what possibility (1 or 2) is realized at the moment. If it is the 1-st possibility, a conventional restart is produced according to the statistics of the outflights without scattering. Otherwise, the point from which the particle is scattered is chosen randomly, according to the equilibrium distribution inside the hidden region (this has been already known), then the particular angle of scattering is defined, and so on (see the scattering outside the hidden region). After all, we get new amplitudes of the particle and check whether it leaves the hidden region or not. In the last case, the whole algorithm is repeated beginning with the choice from the 1-st and 2-nd possibilities. As a result, the "process of restarting" becomes longer due to a possibility of producing a few idle scatterings inside the hidden region without leaving it. But this time has no effect on the simulation time T_2 which takes into account only the motion outside the hidden region.

During the second step, the particle makes R_2 restarts and $C_2 = C_{2s} + C_{2r}$ outflights. At the same time it spends the fraction of time $V_2 < 1$ in the external region (now it is region III). The time which is necessary to achieve the same statistics, when a conventional tracking technique is used, is called *equivalent time*. For the 2-nd step it is as follows:

$$T_{2eq} = T_1 \cdot \frac{R_2}{C_1}. \tag{15}$$

The benefit for the CPU time due to application of the new method can be calculated as T_{2eq}/T_2. On the third step, the probability of the ordinary outflight (1-st possibility) is

$$W_2 = \frac{C_{2r}}{(1 - V_1 \cdot V_2) \cdot T_{2eq} \cdot \tau}. \tag{16}$$

The restarts are produced like on the second step, but using W_2 instead of W_1. In this case, the equivalent time and benefit are:

$$T_{3eq} = T_{2eq} \cdot \frac{R_3}{C_2}, \tag{17}$$

$$\frac{T_{3eq}}{T_3} = \frac{T_1 \cdot R_2 \cdot R_3}{T_3 \cdot C_1 \cdot C_2}. \tag{18}$$

Thus, we have the recurrent formulae to define the lifetime and the probability of the outflight without scattering W_k, which allows us to simulate the restart correctly.

Here we would like to make a remark concerning the value of W_k. At the first sight it looks strange because only near the border of the hidden region the particle is able to leave it without scattering. In spite of this, W_k was defined by the full time which the particle spends within the hidden region, and the most part of this time is spent in the core, far from the border. To clarify this situation, it is necessary to remember the main condition that should be satisfied to obtain the correct distribution outside the hidden region. Namely, we must reproduce the relations between the probabilities to find the particle in a certain place of the phase space at once after it has left the hidden region. We are not interested in how and were from the particle jumps, what time correlation between such events is. We need only the relations between the probabilities and the value of W_k was defined quite correctly for this purpose.

Nevertheless, one more step must be done to successfully include the scattering into simulation. The reason is a decrease in the efficiency of the method when moving to large amplitudes. Indeed, the probability W_k falls down exponentially from step to step while the probability of scattering at the angle $\theta \geq \theta_0$, W_s, keeps the same value for all the steps. As a result, we obtain $W_s \gg W_k$ for $k \gg 1$. On the other hand, to leave the hidden region from the core, larger scattering angles are necessary with the distance of the border of the hidden region from the core. So, a lot of the CPU time will be spent for a huge number of idle scatterings within the hidden region without leaving it. To solve this problem, we use a division of the hidden region produced by sequential boundaries. It is quite easy to find the minimum scattering angles θ_{km} which can force the particle out from the region m to the region k (i.e. outside the hidden region) on the k-th step ($k > m$). Besides, we can calculate the relations between the probabilities to find the particle within these regions since we know the absolute probability for each m-th region:

$$\rho_m = V_0 \cdot V_1 \cdots V_{m-1} \cdot (1 - V_m), \qquad V_0 = 1. \tag{19}$$

This allows us to define the probability W_{km} of scattering from the region m at the angle $\theta \geq \theta_{km}$ during a single turn for the k-th step. The whole probability of scattering at the angles greater than the limit is a

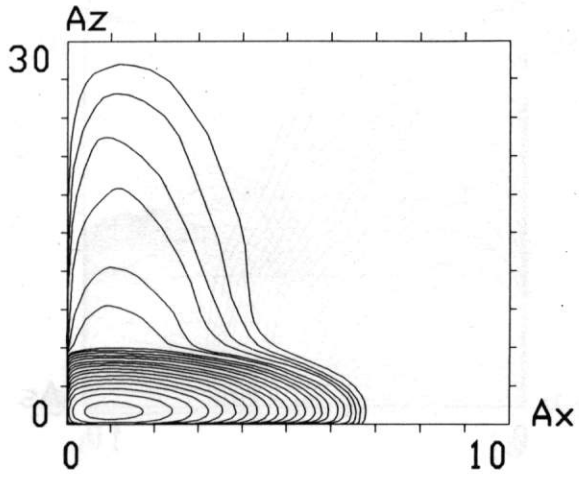

Figure. 9. Equilibrium distribution for VEPP-4 without beam-beam effects. The density of the residual gas is 10^{-8} torr.

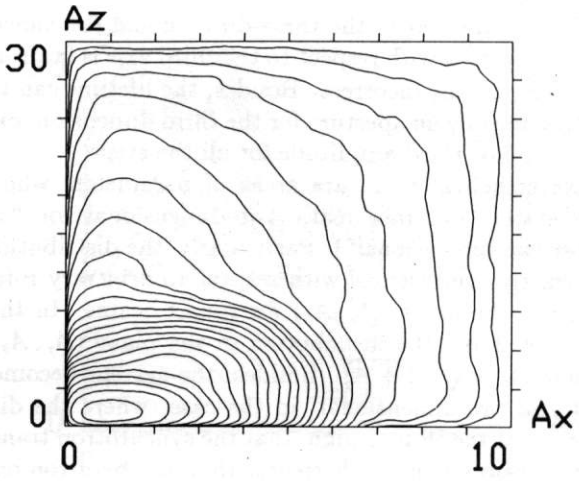

Figure. 10. The same working point as in Fig. 7 with account of the elastic scattering. The density of the residual gas is 10^{-8} torr. The roughness of level lines at large amplitudes caused from statistical errors, but anyway these are smaller than the distance between neighboring lines.

sum of W_{km}, and this value must be used instead of W_s:

$$\widetilde{W}_s = \sum W_{km}. \qquad (20)$$

Now we get $\widetilde{W}_s$ and W_k approximately of the same order of magnitude for all the steps. Now the algorithm of the restart must be changed a little. If the random number generator decides to produce the scattering, first of all we have to choose, according to probabilities W_{km}, where from (considering the region number m) this scattering must be done. Then we choose an arbitrary (according to the distribution that we have already known) point within this region and define the particular angle of scattering as

$$\theta = \theta_{km}/\sqrt{R}, \qquad 0 < R < 1, \qquad (21)$$

where R is the other random number. The inclination angle of a scattering plane and the collider azimuth are defined as usual. Finally, we obtain the new particle amplitudes. After all, we have to check whether the particle leaves the hidden region or not (the scattering on the angle $\theta \geq \theta_{km}$ does not guarantee the leaving).

For example, the equilibrium distribution without beam-beam effects is shown for VEPP-4 in Fig. 9. The lifetime was $4 \cdot 10^{10}$ turns for a vertical aperture of $30\sigma_z$ while the probability of a single scattering from the core to the aperture was $3.5 \cdot 10^{-11}$. The increase in the CPU time because of a more complicated restart algorithm was about 1%. The benefit in the CPU time due to this method was $\sim 10^5$. Fig. 10 shows the result of interference between the beam-beam interaction and the scattering (to be compared with Fig. 7, where scattering is turned off).

IV. THREE-DIMENSIONAL CASE

Up to now we considered the two-dimensional amplitude space. Evidently, all the results can be generalized for the three-dimensional case as well. This means that we have to build a distribution within the three-dimensional amplitude space and use two-dimensional boundaries (i.e., surfaces instead of lines). The only problem arises from the fact that probability to fall within a three-dimensional cell of size δ_A is much less than in the case of a two-dimensional cell. This leads to that the simulation time for each step T must be much greater in the three-dimensional case to satisfy the condition $\widetilde{N}_p \geq \overline{N}$. Moreover, the simulation time T depends now on the damping time τ. Besides, there are some technical difficulties which do not allow us to use the three-dimensional version of the method at the present time. As a compromise, we use a "three-dimensional tracking with two-dimensional distribution". This approach has a limited range of application, but anyway, even outside this range, one can get the essential information.

The algorithm we use can be presented as consisting of three independent parts: the simulation itself (outside the hidden region), building the level lines in the amplitude space, and the simulation of a particle leaving the hidden region (i.e. restarts). The first part represents the physical nature of the phenomenon under investigation and must be three-dimensional because of the important role of the longitudinal motion. Concerning the second part, we can integrate the distribution with respect to the third amplitude and build the boundary similar to that in the two-dimensional case. This means that the boundary is a cylinder within the three-dimensional amplitude space. Nevertheless, each outflight includes six values: all the amplitudes and phases (or coordinates and momenta). What is the effect of such simplification of the boundary? The finite statistics of the outflights can lead to losing some ways (see Fig. 4). For example, reproducing the probability

of being captured in the three-dimensional resonance, whose location with respect to the third axis is far from the core, can be incorrect. Besides, the lifetime can be determined by an aperture for the third dimension, but we keep low third amplitude for all the steps.

Nevertheless, there are areas of parameters where the system becomes really two-dimensional (or "almost two-dimensional"). Particularly, the distribution is exactly symmetrical with respect to arbitrary rotations in the plane (A_x, A_z) for round beams. In this case, we build the distribution in the plane (A_r, A_s), where $A_r = \sqrt{A_x^2 + A_z^2}$. Besides, the system becomes "almost two-dimensional" in the case, where the dispersion at the IP is so high, that the synchrotron transverse beam size is much greater than the betatron one (so-called *monochromatization*[3]). In this case, the horizontal displacement of the particle is mainly defined by the longitudinal motion, and we have to build the distribution in the plane (A_s, A_z). The probability of the particle going to the aperture through large amplitude A_x vanishes in this case, although the resonances are really three-dimensional.

The significance of the longitudinal motion remains essential even without dispersion at the IP due to modulation of the betatron phases. However, the betatron motion seems to be more important and the distribution must be produced in the plane (A_x, A_z). The case, where the synchrotron and betatron beam sizes at the IP becomes comparable, is most difficult. Here all three dimensions are of the same importance and the two-dimensional distribution can result in serious errors in the lifetime determination. Nevertheless, even under such conditions the new method can be helpful. The thing is that all the errors caused by two-dimensional simplification of the distribution give only the increase in the lifetime. Therefore, we can use the method to quickly search for "bad" regions of the parameters (i.e. the regions, where the lifetime is short), while in "good" regions we should use a conventional tracking technique to correctly define the lifetime. The topology of such "bad" regions in the space of various parameters can be an important source of information for future investigations.

V. SOME RESULTS OF TECHNIQUE APPLICATION

The study of beam-beam effects with monochromatization for the Novosibirsk B-Factory Project has given impetus to the development of the proposed technique. As it was shown (see Gerasimov[3]), for flat beams the width of the resonance $l \cdot Q_x + m \cdot Q_z + n \cdot Q_s = k$ depends on the monochromatization parameter λ (it is defined as the ratio of synchrotron and betatron beam sizes at the IP) as follows:

$$\Delta A_z \sim \lambda^{-l/2}. \qquad (22)$$

This formula mathematically represents the fact that significance of the horizontal betatron motion decreases (i.e. the system becomes "almost two-dimensional") in case of increasing the synchrotron beam size at the IP. However, there were some doubts concerning the dispersion at the IP, since a series of strong synchro-betatron resonances arised. The simulation results obtained in 1990–1991 by using a new technique essentially clarified the situation.

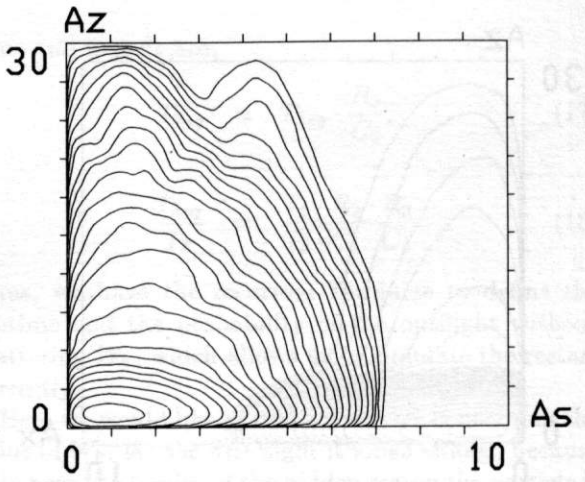

Figure. 11. Equilibrium distribution for VEPP-4M working point: $\{Q_x\} = 0.53$, $\{Q_z\} = 0.57$, $Q_s = 0.02$, $\xi_x = 0.005$, $\xi_z = 0.06$, $\sigma_x/\sigma_z = 80$, $\lambda = 2$.

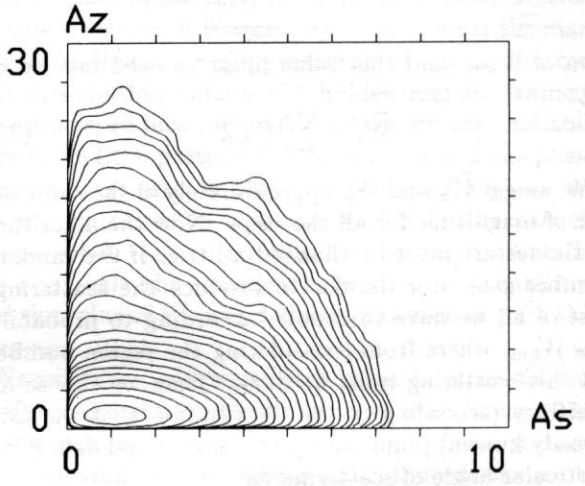

Figure. 12. The same working point as in Fig. 11, but monochromatization parameter $\lambda = 5$. The widths of resonances $l \cdot Q_x + m \cdot Q_z + n \cdot Q_s = k$ with $l \neq 0$ are decreasing here due to increasing of λ.

It is likely that VEPP-4M is the first collider with big dispersion at the IP. This dispersion arises constructively because of a magnet spectrometer for scattered electrons[4] and was considered earlier as a disadvantage. However, we expect now that the permissible tune shift parameter ξ will be sufficiently high. The simulation results for VEPP-4 are shown in Figs. 11, 12. The only distinction between these figures is the monochromatization parameter $\lambda = \sigma_{xs}/\sigma_{x\beta}$. As we can see, the widths of resonances with $l \neq 0$ really fall down with the increase in λ.

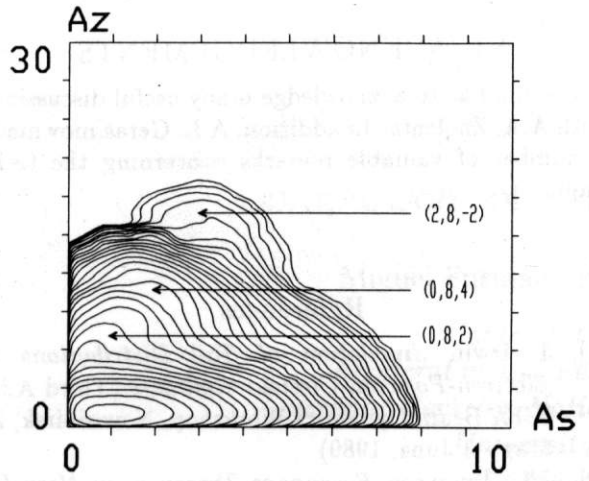

Figure. 13. The B-Factory working point without PC's: $\{Q_x\} = 0.08$, $\{Q_z\} = 0.11$, $Q_s = 0.02$, $\xi_x = 0.01$, $\xi_z = 0.05$, $\sigma_x^*/\sigma_z^* = 300$, $\lambda = \sigma_{xs}^*/\sigma x\beta^* = 10$. Here asterisk (*) denotes the values at the main IP. Resonances $l \cdot Q_x + m \cdot Q_z + n \cdot Q_s = k$ are shown as (l, m, n).

A large number of bunches in the B-Factory leads to parasitic crossings (PC's). As a rule, there are two PC at a distance of about 2 meters from the main IP, all the next bunches are shielded by a vacuum chamber. In spite of considerable separation (20–40 beam sizes), the PC can essentially disturb the opposite beam due to high value of a beta-function (see Fig. 13, where there are no PC's, and compare with Figs. 14 and 15, where they are present). The direction of the separation is also very important. The technique was used to search for the minimum separation value which is allowed for both horizontal and vertical separations. The specific instability, which results in losing the particle when it achieves a certain threshold in the vertical amplitude, was discovered for the vertical separation (see Fig. 14). This threshold can be several times smaller than the separation value! In case of the horizontal separation, the PC's have much less influence (see Fig. 15). The lifetime versus the separation value is shown in Fig. 16 for both cases (the vertical aperture is $30\sigma_z$, the horizontal aperture is $10\sigma_x$, all the particles were lost at the vertical aperture).

The technique was also used in simulations for the Novosibirsk φ-Factory Project with round beams. The high intensity and low energy of the beams led to strong longitudinal beam-beam effects[5]. Particularly, strong flows to high amplitudes (both betatron and synchrotron) could arise due to these effects (see Fig. 17). In order to suppress such flows, an interesting idea of negative momentum compaction[6] was suggested by V.V. Danilov and E.A. Perevedentsev. The simulation results for the same working point as in Fig. 17 and inverse sign of the momentum compaction factor are shown in Fig. 18.

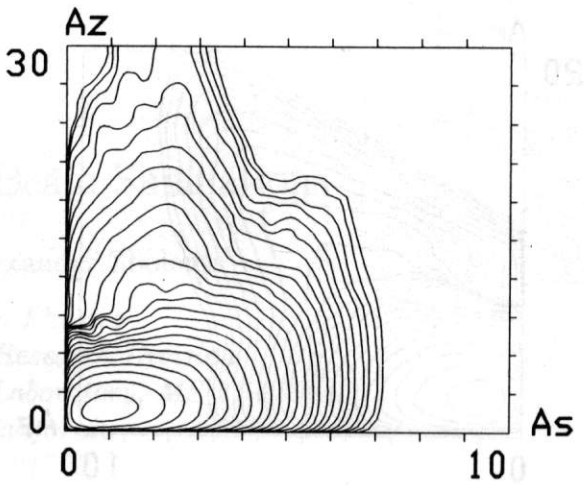

Figure. 14. The same working point as in Fig. 13 with account of two PC's (vertical separation on $50\sigma_z$). An instability arises, which results in short lifetime.

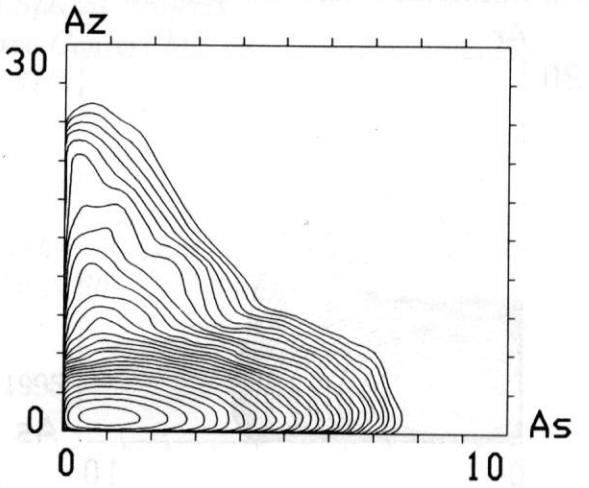

Figure. 15. The same working point, but horizontal separation on $20\sigma_x$ instead of the vertical one. Pay attention that σ_x and σ_z becomes almost equal at the PC.

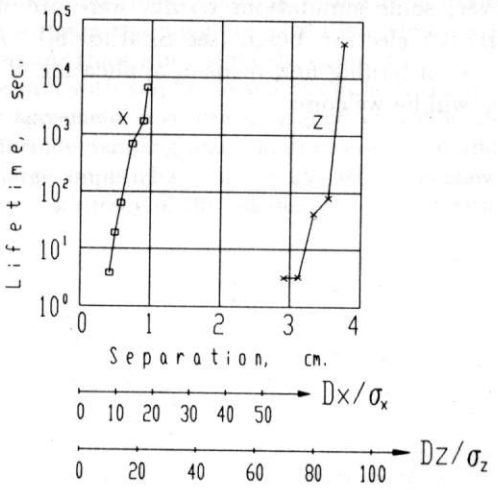

Figure. 16. Lifetime versus the separation value (horizontal or vertical) at the PC.

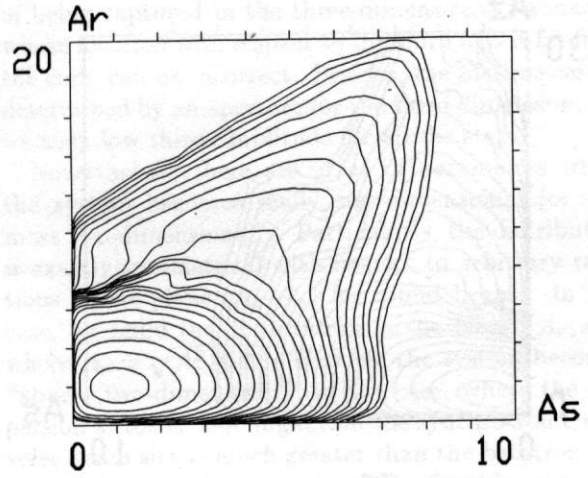

Figure. 17. Equilibrium distribution for φ-Factory with round beams. $\{Q_{x,z}\} = 0.04$, $Q_s = 0.02$, $\xi_{x,z} = 0.2$. The strong flow to large amplitudes arises due to longitudinal beam-beam effects.

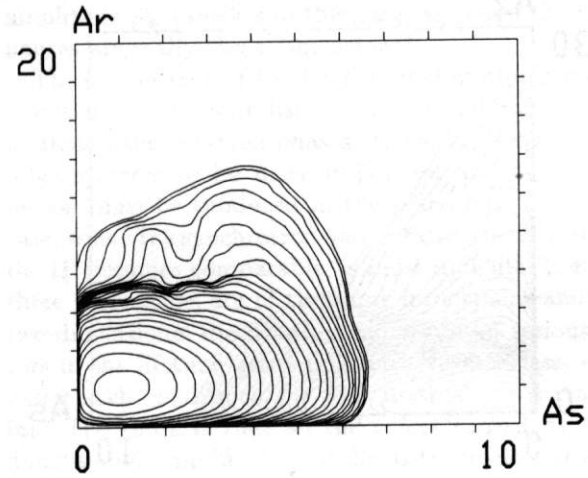

Figure. 18. The same working point as in Fig. 17, but momentum compaction factor is negative.

Moreover, some simulations results were obtained for the HERA electron beam (see Shatilov[8]). Any suggestions concerning new fields of application of the technique will be welcome.

VI. ACKNOWLEDGEMENTS

I would like to acknowledge many useful discussions with A.A. Zholents. In addition, A.L. Gerasimov made a number of valuable remarks concerning the technique.

References

[1] J. Irwin *Simulation of Tail Distributions in Electron-Positron Circular Colliders* (Third Adv. ICFA Beam Dynamics Workshop, Novosibirsk, 29 May - 3 June, 1989)

[2] J.L. Tennyson *Resonance Transport in Near Integrable Systems with Many Degrees of Freedom*, Physika D, v.5 (1982) p.123

[3] A.L. Gerasimov et al. *Beam-Beam Effects with Big Dispersion Function at the Interaction Point*, NIM **A305** (1991) 25

[4] V.M. Aulchenko et al. *Scattered Electrons Registration System of KEDR Detector for Two-Photons Process Investigation* (INP 91-49, Novosibirsk, 1991)

[5] V.V. Danilov et al. *Longitudinal Beam-Beam Effects for an Ultra-High Luminosity Regime* (IEEE Part.. Acc. Conf., San-Francisco, May 6-9, 1991)

[6] V.V. Danilov et al. *Negative Momentum Compaction in the Longitudinal Beam-Beam Effects* (Int. Conf. on High Energy Acc., Hamburg, July 20-24, 1992)

[7] D.N. Shatilov *Beam-Beam Simulations at Large Amplitudes and Lifetime Determination* (INP 92-79, Novosibirsk, 1992)

[8] D.N. Shatilov *Beam-Beam Simulations for the HERA Electron Beam* (DESY HERA 93-12, Hamburg, 1993)

[9] T. Chen et al. *Simulation of the Beam Halo from the Beam-Beam Interaction* (Phys. Rev. E, v.49, No3, p.2323, 1994)

[10] J. Tennyson *Undocumented code "TRS"*, 1989

[11] M. Furman et al. *Comparisons of Beam-Beam Code Simulations* (CBP Tech Note-59, 1995)

Comparison of Beam-Beam Simulations*

Miguel Furman and Alexander Zholents

Center for Beam Physics
Accelerator and Fusion Research Division
Lawrence Berkeley National Laboratory, MS 71-259
University of California
Berkeley, CA 94720

and

Tong Chen

Accelerator Theory and Special Projects
Stanford Linear Accelerator Center, MS 26
Stanford, CA 94309

and

Dmitry Shatilov

Budker Institute of Nuclear Physics
630090 Novosibirsk 90
Russia

August 22, 1995

Abstract

We carry out a methodical comparison among the four beam-beam codes TRS, BBTRACK3D, LIFETRAC and TAIL under a restricted set of conditions for which such a comparison is meaningful. We first study the convergence rate of five slicing algorithms as the number of kicks goes to infinity and provide a criterion for the minimum number of kicks required for acceptable accuracy in a given situation. We then focus on turn-by-turn single particle tracking in 6-dimensional phase space in weak-strong mode for a thick-lens beam-beam interaction in the absence of damping and quantum excitation effects and lattice nonlinearities. When the codes make use of the the same thick-lens slicing algorithm, the results agree within computer accuracy. We also compute the tune shift with amplitude and compare the results with those from the first-order analytic calculation. The agreement is surprisingly good except when synchrotron sidebands are prominent. We then go on to include damping and quantum excitation and compute the 2-D particle distributions out to reasonably large amplitudes. The results, which we show in the form of contour level plots, agree within the statistical accuracy of the calculations. This article summarizes Ref. [1].

*Work supported by the Director, Office of Energy Research, Office of High Energy and Nuclear Physics, High Energy Division, of the US. Department of Energy under Contracts no. DE-AC03-76SF00098 and DE-AC03-76SF00515.

1. Introduction

It is sometimes apparent that beam-beam simulations do not enjoy the same degree of respectability in today's accelerator physics community that other tools, such as single-particle tracking, do. One often hears, for example, that beam-beam simulations are better able to explain observed phenomena a posteriori rather than to predict them. Undoubtedly, the fundamental reason for this state of affairs is the complexity of the beam-beam interaction. A complete calculation would require the solution of Maxwell's and Newton's equations simultaneously for many billions of particles for millions of turns. It is clear that such a task is impossible with computers that are available today or that will be in the foreseeable future.

Nevertheless, much is known qualitatively and quantitatively about the beam-beam interaction in various regimes, and several codes have been developed that embody different approximations. Although the ultimate test of any beam-beam code is the correct and complete prediction of collider beam dynamics, it seems important for the time being to compare these codes with each other and with analytical results, and ensure that there is agreement whenever these comparisons are meaningful.

At its core, many of these codes have a common element: a thin-lens kick produced by a gaussian particle distribution. In this note we carry out a comparison among four beam-beam codes that involve this thin-lens kick. We start with the simplest case, namely the turn-by-turn tracking of a single particle colliding once per turn against an opposing gaussian bunch, and we compare the six-dimensional coordinates of the particle at every turn, in the absence of radiation damping, quantum excitation and lattice nonlinearities. We carry out the comparison for thin-lens and thick-lens beam-beam interaction, for five "slicing" algorithms, with or without synchrotron oscillations, for several initial conditions (but not in all possible combinations). When the codes do the same thing, the results indeed agree with each other within computer precision. We also compare the results for the calculated tune shift with amplitude with analytical results for the case of a thin lens. In the final step, we carry out a longer term simulation and produce the two-dimensional particle distribution in amplitude space with three of the codes. The agreement is very good, and the relatively small discrepancies are likely due to the difference in the algorithms used at this stage of the comparisons.

In all calculations presented here we use the "weak-strong" description of the beam-beam interaction. In this scheme the "strong" beam is passive and is represented by a gaussian lens (thin or thick) that is not altered by the other beam. The "weak" beam is dynamical, and we observe its behavior as a function of time as it collides repeatedly against the strong beam. In most, but not all, of the simulations carried out here, we use beam parameters that correspond closely to the PEP-II B factory [2], in which the electron beam plays the role of the strong beam and the positron that of the weak.

The four beam-beam codes we consider here are: TRS [3], LIFETRAC [4], TAIL [5] and BBTRACK3D [6]. The code TRS is a multiparticle strong-strong code that involves the soft-gaussian approximation. It is geared to assessing the luminosity performance of an e^+e^-collider. The codes LIFETRAC and TAIL are single-particle weak-strong codes geared to assessing the beam lifetime. The code BBTRACK3D is a single-particle weak-strong code geared to studying the dynamics of a single particle with specified initial conditions. Among its options, it allows different forms for the particle density of the strong beam, the gaussian being only one of them.

2. Slicing algorithms

We assume that the longitudinal distribution of the opposing bunch is described by a gaussian density

$$\hat{\rho}_\ell(z) = \frac{e^{-z^2/2\sigma_z^2}}{\sqrt{2\pi}\sigma_z} \tag{1}$$

where the caret "^" is meant to emphasize unit normalization. For the purposes of tracking simulations, we replace this density by a weighted superposition of N_s delta functions,

$$\hat{\rho}_\ell(z) \to \hat{\rho}_s(z) \equiv \sum_{k=-L}^{L} w_k \delta(z - z_k) \tag{2}$$

where $N_s \equiv 2L+1$ (we assume, as is customary, that N_s is an odd integer; if this is not the case, our calculation needs slight modifications). Each delta function gives rise to a kick at a location z_k weighted by w_k; these locations and weights must be determined according to a certain algorithm. The symmetry $\hat{\rho}_\ell(-z) = \hat{\rho}_\ell(z)$ implies that the kick locations and weights must obey the basic constraints $z_{-k} = -z_k$ and $w_{-k} = +w_k$. In addition, we require that the accumulated effects of the kicks should be the same as in the original distribution, *i.e.*, $\int dz \hat{\rho}_\ell(z) = \int dz \hat{\rho}_s(z) = 1$, which implies

$$\sum_{k=-L}^{L} w_k = 1 \tag{3}$$

For the thin-lens case ($N_s = 1$) there is a single kick at the center of the bunch with $z_0 = 0$ and $w_0 = 1$. For the thick lens case, on the other hand, there is, of course, an infinite number of possible algorithms to decide the weights and locations of the kicks consistent with the basic constraints. Here we examine only five possibilities. For the case $N_s = 5$ we list the kick locations and weights for all five algorithms in Table 1.

Algorithm #1 (equal spacing). In this case [7] the kicks are equally spaced and the weights are proportional to the gaussian density at z_k, namely

$$\frac{z_k}{\sigma_z} = \frac{2k}{N_s - 1}\left(1 + \frac{N_s - 3}{12}\right), \qquad w_k = \frac{\hat{\rho}_\ell(z_k)}{\sum_{m=-L}^{L} \hat{\rho}_\ell(z_m)} \qquad (k = 0,\ \pm 1, \cdots,\ \pm L,\ N_s \geq 3) \tag{4}$$

Algorithm #2 (equal areas). In this case the gaussian distribution (1) is divided up into N_s "slices" of equal area (implying equal charge), and the kicks are located at the center of charge of each slice. The equality of the area of the slices implies that the weights are all equal, namely $w_k = 1/N_s$. Standard formulas for the area under a gaussian curve imply that the kick locations are given by

$$\frac{z_k}{\sigma_z} = \sqrt{2}\,\mathrm{erf}^{-1}\left(\frac{2k}{N_s}\right) \qquad (k = 0,\ \pm 1, \cdots,\ \pm L,\ N_s \geq 3) \tag{5}$$

Algorithm #3. This case [8, 9] is similar to the previous one, except that the kick locations are given by

$$\frac{z_k}{\sigma_z} = N_s\left[\hat{\rho}_\ell(l_k) - \hat{\rho}_\ell(l_{k+1})\right], \qquad k = 1, \cdots,\ L \tag{6}$$

where the l_k's are the edges of the slices. By arguments similar to those in the previous case, it is easy to see that, for $k > 0$,

$$\frac{l_k}{\sigma_z} = \sqrt{2}\,\mathrm{erf}^{-1}\left(\frac{2k-1}{N_s}\right) \qquad (k = 1,\ 2, \cdots,\ L+1,\ N_s \geq 3) \tag{7}$$

For $k < 0$, the l_k's are the mirrors of those for $k > 0$ (note that there is no $k = 0$ edge, and that the $k = \pm(L+1)$ edges are at $\pm\infty$). As in all cases, the central kick is at $z_0 = 0$, and the kicks for $k < 0$ are symmetrically located with respect to those for $k > 0$. The weights are the same as in the previous case, namely $w_k = 1/N_s$.

Algorithm #4. This is a modified combination of algorithms #1 and #3 in which

$$\frac{z_k}{\sigma_z} = \frac{1}{w_k}\left[\hat{\rho}_\ell(l_k) - \hat{\rho}_\ell(l_{k+1})\right], \qquad k = 1, \cdots,\ L \tag{8}$$

where the l_k's are the same as above, and where the locations for $k < 0$ are the mirror images of those for $k > 0$. The weights are proportional to $\sqrt{\hat{\rho}_\ell(z)}$, namely

$$w_k = \frac{\sqrt{\hat{\rho}_\ell(z_k)}}{\sum_{m=-L}^{L} \sqrt{\hat{\rho}_\ell(z_m)}} \qquad (k = 0,\ \pm 1, \cdots,\ \pm L,\ N_s \geq 3) \tag{9}$$

In practice, the z_k's and w_k's are most easily found by iteration. It turns out that, of all five slicing algorithms described here, this algorithm #4 has the fastest rate of convergence as $N_s \to \infty$ (see the discussion below).

Algorithm #5. This algorithm consists of choosing the z_k's and w_k's in such a way that the area enclosed by the two functions $\int_0^z dz' \hat{\rho}_\ell(z')$ and $\int_0^z dz' \hat{\rho}_s(z')$ is minimal. This requirement leads to a set of nonlinear equations for the z_k's and w_k's which, as in algorithm #4, is most easily solved by iteration.

Table 1: Kick locations and weights for $N_s = 5$.

	Algorithm #1	Algorithm #2	Algorithm #3	Algorithm #4	Algorithm #5
	−1.166667	−1.281552	−1.399809	−1.59898	−1.44156
	−0.5833333	−0.5244005	−0.5319032	−0.67872	−0.63623
z_k's	0.0	0.0	0.0	0.0	0.0
	0.5833333	0.5244005	0.5319032	0.67872	0.63623
	1.166667	1.281552	1.399809	1.59898	1.44156
	0.1368561	0.2	0.2	0.17350	0.14943
	0.2280002	0.2	0.2	0.23222	0.22577
w_k's	0.2702873	0.2	0.2	0.26056	0.24960
	0.2280002	0.2	0.2	0.23222	0.22577
	0.1368561	0.2	0.2	0.17350	0.14943

Convergence rate of the five slicing algorithms. A reasonable requirement for any given algorithm is that the results should converge to a limit as $N_s \to \infty$. A reasonable requirement for all algorithms is that they should converge to the same answer in this limit. It remains an open problem to establish the optimal thick-lens slicing algorithm among the infinite number of possibilities. By "optimal algorithm" we mean that which yields, for a given finite number of kicks, the closest answer to the $N_s = \infty$ limit for a particular problem. This is clearly a very difficult problem: one cannot even set forth a universal criterion for such an optimization because such a criterion necessarily depends on many variables of the problem at hand, such as the working point, beam aspect ratios, etc.

In this section we try to solve a more modest problem: we study the convergence rate of the five slicing algorithms presented above as the number of kicks $N_s \to \infty$. Although this is clearly a more restricted problem than the one stated in the previous paragraph, the answer is still quite interesting because it shows clear systematics. As we show below, algorithm #4 emerges as the clear favorite among the five. Within this limited context, we also give an answer to the important practical question of how many kicks are enough for a given situation.

We proceed as follows: we first generate a weak bunch of 1,000 particles distributed gaussianly in the 6-D normalized phase space $(X_1, \ldots, X_6) \equiv (x/\sigma_{x+}, x'/\sigma_{x'+}, y/\sigma_{y+}, y'/\sigma_{y'+}, z/\sigma_{z+}, \Delta p/\sigma_{p+})$ where the subscript "+" is meant to emphasize that this is the weak (positron) beam. The coordinates are generated in an uncorrelated fashion, so that we may think of the distribution as that corresponding to a gaussian beam matched to the bare lattice at the IP. We then push this distribution once through the thick beam-beam lens produced by the strong beam for a given slicing algorithm and for a given number of kicks, and compare the resultant distribution with the one obtained by pushing the *same* initial distribution according to the "$N_s = \infty$" case which, for practical purposes, we define to be algorithm #4 with 300 kicks. Note that our criterion does not depend on any lattice parameter; it is designed to judge the beam-beam interaction by itself, as an isolated entity.

We compare the algorithms quantitatively by defining a dimensionless parameter Q for each algorithm as the sum of the rms deviations of the four transverse phase space coordinates of the final distribution from

those obtained from the $N_s = \infty$ case,

$$Q = \sum_{n=1}^{4} \sqrt{\langle (X_n - X_{n,\infty})^2 \rangle} \tag{10}$$

where $\langle \cdots \rangle$ is the average over the 1,000 particles. Obviously, the smaller is Q the better is the slicing algorithm. We present here only one case, corresponding to a flat beam with PEP-II-like parameters [2], listed in Table 2. Other cases, with qualitatively similar results, are described in Ref. [1].

Table 2: Parameters for the convergence rate tests.

β^*_{x+}/σ_{z+}, β^*_{y+}/σ_{z+}	37.5, 1.5
$\beta^*_{x-}/\beta^*_{x+}$, $\beta^*_{y-}/\beta^*_{y+}$	1.333, 1.333
σ_{x-}/σ_{x+}, σ_{y-}/σ_{y+}, σ_{z-}/σ_{z+}	1, 1, 1
σ_{x-}/σ_{y-}	25
ξ_{x+}, ξ_{y+}	0.03, 0.03

Figure 1 shows the results of plotting Q *vs.*the number of kicks N_s for the five algorithms. It is apparent that algorithm #4 has systematically the fastest convergence rate of the five. It is curious that algorithm #1 does not converge uniformly, although it becomes competitive with #4 for $\gtrsim 50$ or more kicks.

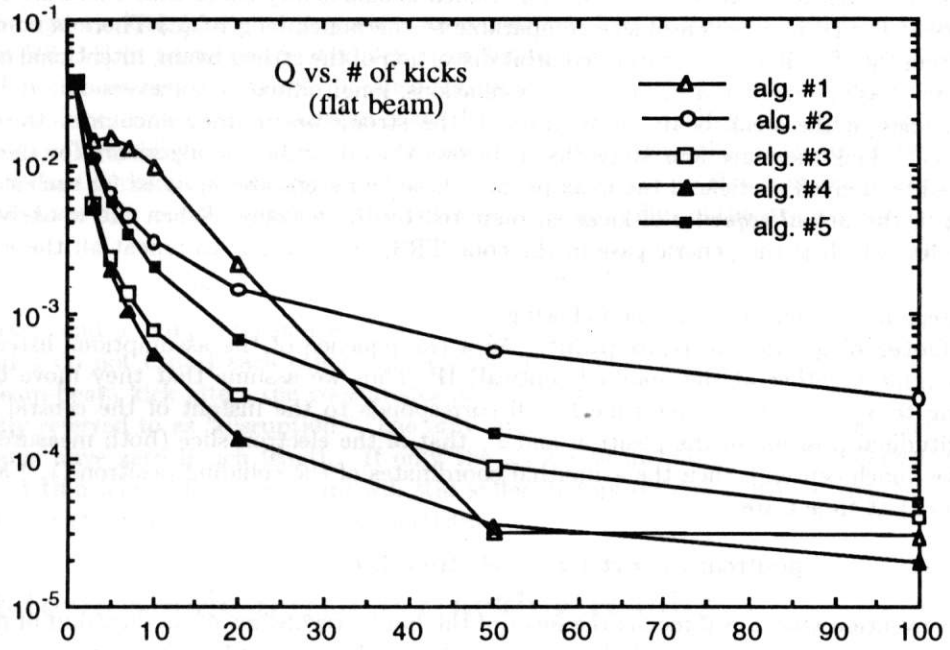

Figure 1: Convergence of the slicing algorithms: Q plotted vs. number of kicks N_s for flat beams (PEP-II-like parameters; see Table 2).

A criterion for the adequate number of kicks. It is important to decide how many kicks are enough for a given problem because, all other things being equal, the CPU time used in the calculation is proportional to N_s. We now provide a criterion for the minimum value required for N_s for issues pertaining to the beam

core (such as the beam blowup due to the beam-beam interaction, or, equivalently, the luminosity). The reasoning is as follows: due to the effects of radiation damping and quantum excitation, the rms beam size in the transverse dimension fluctuates by

$$\frac{\delta\sigma}{\sigma} \simeq \frac{1}{\sqrt{\tau}} \tag{11}$$

where τ is the damping time (in units of turn number) corresponding to the dimension considered. Because of these fluctuations, it is not justified to increase the accuracy of the beam-beam element beyond that corresponding to a value of Q given by

$$Q \simeq \frac{4}{\sqrt{\tau}} \tag{12}$$

(the factor 4 accounts for the four terms in Eq. (10)). Thus once we know the convergence rate of a given algorithm, the criterion is the following: the minimum value of N_s that gives the correct answer (within the statistical accuracy of the calculation) is that for which Q takes on the value given by Eq. (12).

For the case of PEP-II, with $\tau = 5400$, this yields $Q \simeq 0.05$. Therefore, as one can see from Fig. 1, any of the five algorithms gives the correct answer for $N_s = 3$. For other situations there are big differences in the number of slices required by each algorithm to converge to a result with a given accuracy [1]. Nevertheless, algorithm #4 has consistently the fastest convergence rate among the five possibilities shown here.

3. The thick lens beam-beam interaction

In all cases described in this article we make the following assumptions: (a) The particles are relativistic so that we can neglect their self-interactions. (b) The bunch is sufficiently short that there are no nontrivial lattice elements at the IP in a region of size comparable to the bunch length. (c) There is no dispersion in this region around the IP. (d) There is no closed orbit distortion of the strong beam, intentional or accidental. (e) There are no phasing errors and no collective oscillations, longitudinal or transverse.

As the particles in the weak beam move through the strong beam, they encounter the N_s kicks in sequence. For each kick there are four steps (listed below) that describe the algorithm for the beam-beam kick experienced by a given particle in the weak beam. These four steps are repeated for each slice and must be carried out in the *actual sequence* of kicks encountered by the particle. When the weak beam consists of many particles, which is the generic case in the code TRS, one also has to repeat all these steps for all particles.

The four steps for a single kick are the following:

Step 1: Determine the collision point. As a consequence of the assumptions listed above, the bunch centers come together at the nominal (optical) IP. Thus we assume that they move towards each other according to $s_\pm = \pm ct$, so that time $t = 0$ corresponds to the instant of the central collision. If z_+ is the longitudinal position of the positron and z_- that of the electron slice (both measured relative to their respective bunch centers), then the azimuthal coordinates of the colliding positron (s_+) and opposing electron slice (s_-) at time t are

$$\text{positron: } s_+ = ct + z_+; \quad \text{electron slice: } s_- = -ct - z_- \tag{13}$$

(we take the convention that $z > 0$ means the head of the bunch regardless of its direction of motion). The collision point between the positron and the opposing slice is determined by setting $s_+ = s_- \equiv s_c$, which implies

$$\text{collision point: } s_c = \tfrac{1}{2}(z_+ - z_-) \tag{14}$$

Step 2: Determine the transverse coordinates. In all codes considered here the longitudinal as well as the transverse coordinates of the particles are *referred to the bunch center*. Since the beam-beam kick is represented by a thick lens whose strength varies during the course of the collision (due to the s dependence of the transverse size of the opposing bunch), we have to find the actual transverse coordinates

of the colliding particle. As a consequence of the assumptions listed above, the transformation from the bunch center to the actual collision point is a simple drift:

$$x \to x + s_c x', \qquad y \to y + s_c y' \tag{15}$$

while the slopes x' and y' remain unchanged.

Step 3: Actual kick. In this step the slopes of the particle are changed according to

$$x' \to x' + \Delta x'\left(x, y, \sigma_{x-}(s_c), \sigma_{y-}(s_c)\right), \qquad y' \to y' + \Delta y'\left(x, y, \sigma_{x-}(s_c), \sigma_{y-}(s_c)\right) \tag{16}$$

while x and y remain unchanged. In computing $\Delta x'$ and $\Delta y'$ we use x and y from Step 2 and the actual beam sizes of the opposing bunch at the collision point, given by

$$\sigma_{x-}(s_c) = \sigma_{x-}(0) \times \sqrt{1 + \left(s_c/\beta^*_{x-}\right)^2}, \qquad \sigma_{y-}(s_c) = \sigma_{y-}(0) \times \sqrt{1 + \left(s_c/\beta^*_{y-}\right)^2} \tag{17}$$

In all calculations discussed here we assume that the transverse distribution of the strong bunch is gaussian. Thus a particular slice of electrons centered at the origin and having horizontal and vertical rms sizes $(\sigma_{x-}, \sigma_{y-})$ is described by the transverse particle density

$$\rho_t(x, y) = \frac{\Delta N_-}{2\pi\sigma_{x-}\sigma_{y-}} \exp\left(-\frac{x^2}{2\sigma^2_{x-}} - \frac{y^2}{2\sigma^2_{y-}}\right) \tag{18}$$

which is normalized to the number of electrons ΔN_- contained in the slice (for the k-th slice, $\Delta N_- = w_k N_-$, where N_- is the total number of electrons in the bunch).

The electromagnetic kick ($\Delta x'$, $\Delta y'$) received by a positron from a thin-slice electron bunch is written in concise form [10, 11] in terms of the complex error function $w(z)$[1] In tracking codes it is important to compute this function as fast as possible because this is the most CPU-intensive part of any beam-beam simulation that assumes a transverse gaussian shape for the bunches. In Ref. [1] we describe four methods of computing $w(z)$. They all yield results that are accurate to better than 1 part in 10^6. However, there are major differences in the computational speed of the different methods; we shall not address this issue here.

Step 4: Restore the coordinates to the reference point. This is the inverse of Step 2, namely

$$x \to x - s_c x', \qquad y \to y - s_c y' \tag{19}$$

while the slopes x' and y' remain unchanged.

Steps 2 and 4 do not cancel each other out because the slopes have changed in Step 3; therefore, in general, the beam-beam kick alters the coordinates as well as the slopes of the particles. For this reason, Step 4 is usually referred to as "disruption." The only circumstance in which there is no disruption occurs when *both* beams have zero bunch length. If only the strong beam has zero bunch length (*e.g.*, if it is represented by a thin lens), the weak beam will still suffer disruption due to the s_c dependence in Step 3 arising from the synchrotron oscillations of its particles.

4. Short-term single-particle tracking results

Here we carry out turn-by-turn tracking for an individual particle at a time with given initial coordinates for a certain number N of turns. *For all cases in this section we completely neglect damping and quantum excitation* in order to eliminate numerical discrepancies arising from random number generators.

We assume that the lattice is decoupled and is described by a pair of 2×2 linear transport maps with given tunes. Similarly, we also assume that the longitudinal dynamics is described by a linear 2×2 map with a given synchrotron tune. We carry out a weak-strong calculation where the dynamical (or weak) beam is

[1]The function $w(z)$ is not to be confused with the weights w_k of the previous section, nor is the complex number z with the longitudinal coordinate z.

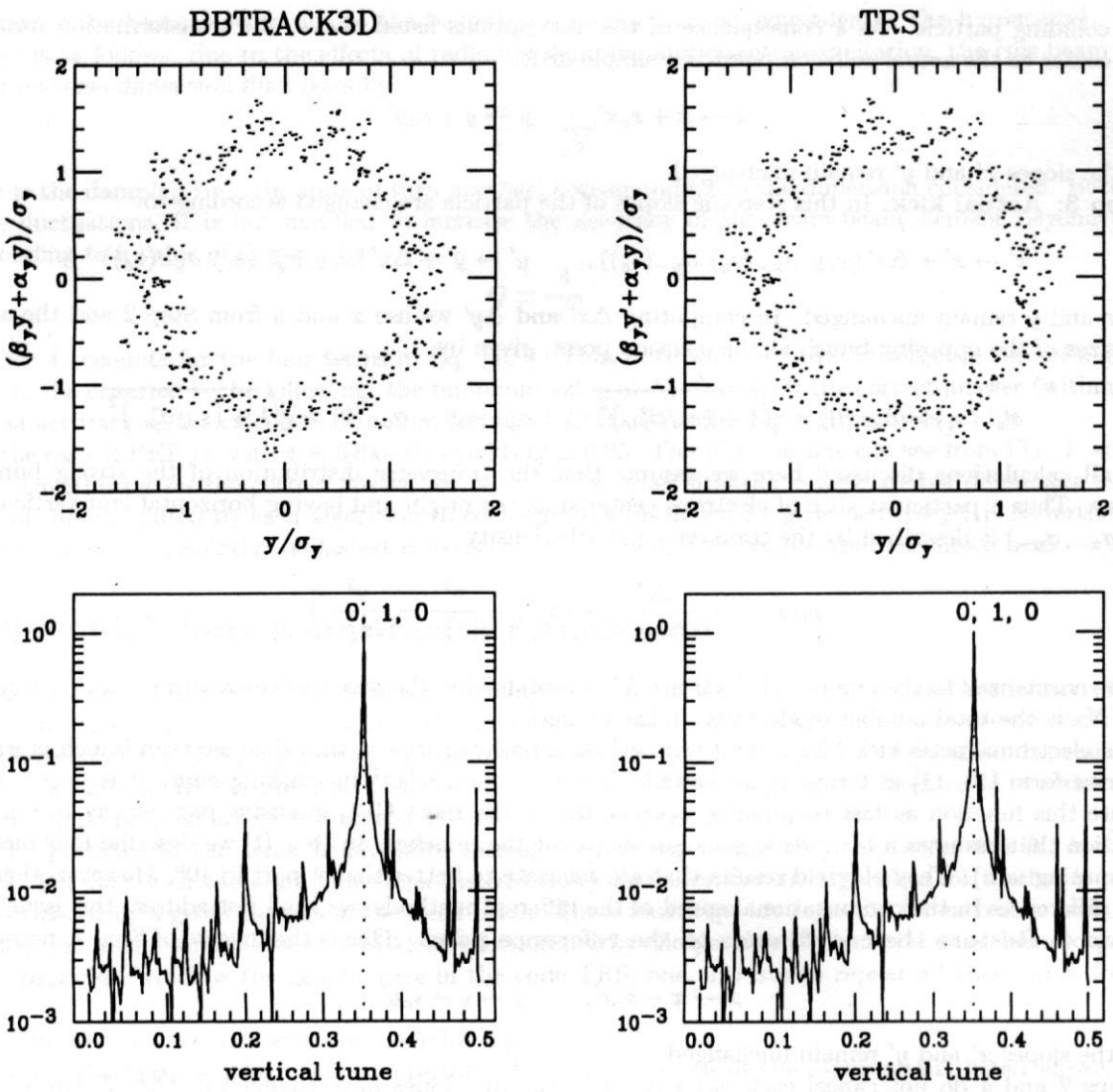

Figure 2: Single particle tracking (BBTRACK3D and TRS, $N = 512$, $N_s = 5$, slicing alg. #2).

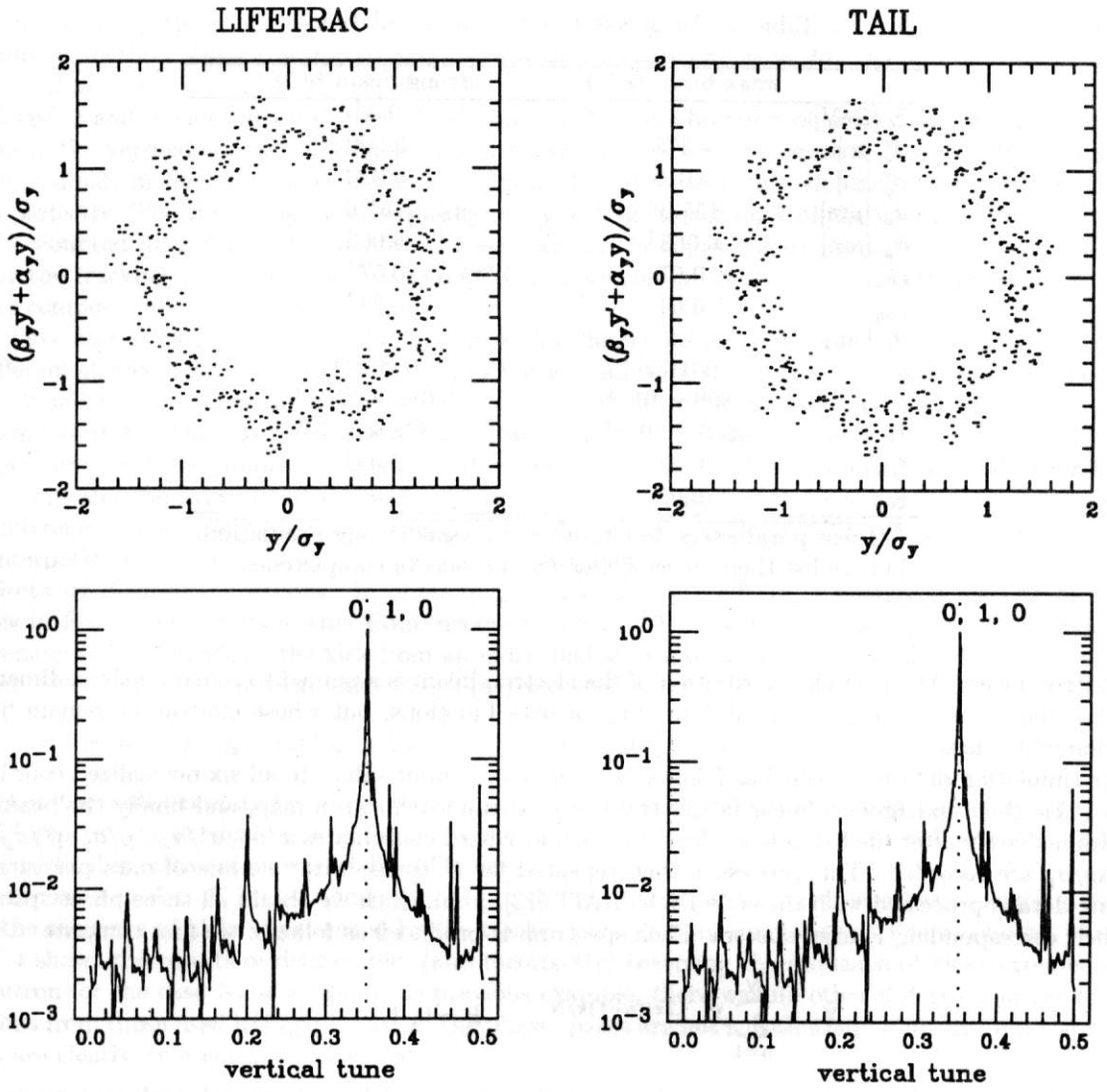

Figure 3: Single particle tracking (LIFETRAC and TAIL, $N = 512$, $N_s = 5$, slicing alg. #2).

Table 3: Parameters used in the simulations.

	weak beam (e^+)	strong beam (e^-)
E [GeV]	3.1	9.0 †
β_x^* [m]	0.375	0.500
β_y^* [m]	0.015	0.020
σ_x [μm]	151.6 †	151.6
σ_y [μm]	6.063 †	6.063
ν_{0x}	0.57	0.57 †
ν_{0y}	0.64	0.64 †
σ_z [cm]	1.0	1.0
ν_s	0.0372	0.0523 †
σ_p/p	0.809×10^{-3}	0.615×10^{-3} †
N	5.630×10^{10} †	3.878×10^{10} †
ξ_{0x}	0.03	0.03 †
ξ_{0y}	0.03	0.03 †

† These parameters do not enter the weak-strong simulation, but we list them nevertheless for the sake of completeness.

the positron beam. The particle distribution of the electron beam is assumed to remain a three-dimensional gaussian whose transverse size is modulated by the beta functions, but whose emittances remain fixed at their nominal values.

The simulation data is obtained as follows: we first assign input values to all six normalized coordinates. The particle then undergoes a linear lattice transport, then a synchrotron map, and finally the beam-beam kick. Immediately after the beam-beam kick, its six normalized coordinates x/σ_x, $x'/\sigma_{x'}$, y/σ_y, $y'/\sigma_{y'}$, z/σ_z and $\Delta p/\sigma_p$ are recorded. This process is then repeated for N turns, with one line of data per turn. The tracking data is processed with the code PORTRAIT [12], from which we obtain all three phase space plots and their corresponding Fourier spectra. Each spectrum is produced as follows: we first compute

$$\tilde{X}_k = \sum_{n=1}^{N} X_n \, e^{2\pi i (n-1)k/N}, \qquad k = 0,\, 1,\, \cdots,\, N-1 \tag{20}$$

where X_n represents here either x/σ_x or y/σ_y or z/σ_z at turn n. We then normalize the spectrum by the largest of the absolute values $|\tilde{X}_k|$'s, and plot these normalized absolute values *vs.* k/N. We only plot the spectrum for the modes $k = 0,\, 1,\, \cdots,\, N/2$ on account of the well-known reflection symmetry of $|\tilde{X}_k|$ about $k = N/2$.

In addition to the spectrum, PORTRAIT computes all three dynamical tunes ν_x, ν_y and ν_z by numerically integrating the three phases over the N turns. We then form the linear combinations $n\nu_x + m\nu_y + l\nu_z$ where n, m and l are positive or negative integers[2] up to a certain maximum absolute value, and we plot a vertical dotted line whenever $n\nu_x + m\nu_y + l\nu_z$ (aliased to the interval $[0, 0.5]$) coincides with a local peak of the spectrum that is higher than a given threshold value. In this way we can identify resonances, which are labeled by the three integers n, m and l on the plots.

The simulation parameters are listed in Table 3. The values in this table are like those considered for the PEP-II B factory [2]; for the nominal PEP-II bunch collision frequency of 238 MHz, these parameters imply a nominal luminosity of $\mathcal{L}_0 = 3 \times 10^{33}$ cm^{-2} s^{-1}.

Comparison of the four codes. We now compare the results of the four codes considered here. In all cases we track for $N = 512$ turns, use $N_s = 5$ kicks, and use slicing algorithm #2. We compute $w(z)$

[2] Except that, without any loss of generality, we choose $n \geq 0$.

by simply invoking the IMSL® library function CERFE [13] except that the code TAIL uses the Padé approximant method [14]. The initial values of the coordinates are $x_0 = 3\sigma_x$, $y_0 = 1.5\sigma_y$, $z_0 = 3\sigma_z$ and $x'_0 = y'_0 = \Delta p_0 = 0$.

In Figs. 2 and 3 we show only the vertical phase space and spectrum obtained from each of the codes. We choose the vertical spectrum because, in our experience, it is more sensitive than the horizontal (and the longitudinal) in showing differences in the results. It can be seen that the codes agree with each other almost perfectly. The tiny differences (typically in the 4th or higher digit of the values of the coordinates) can be accounted for by the differences in the accuracy of the input values and of the different computers used for the tracking (codes TRS and BBTRACK3D were run on the same computer and their results do agree to computer accuracy).

We have carried out many more simulations with different initial conditions, different number of slices and different slicing algorithms. Ref. [1] contains but a small sample of these. The excellent agreement seen in Figs. 2 and 3 is typical of the larger set.

Algorithms for the complex error function. In Ref. [1] we also present a systematic comparison of four algorithms for the computation of $w(z)$: table interpolation to 3rd and 4th order, the Padé approximant method [14], and the IMSL library function CERFE [13]. The result of this exercise is that there are only small differences in accuracy (smaller than 1 part in 10^6), but large differences in computational speed. The table interpolation to 3rd order is the fastest of the four methods.

Effects of deliberate errors. In order to get an idea of the effects of nontrivial algorithmic errors, we show in Fig. 4 the results arising from incorrect coding. The first set in this Figure corresponds to an older version of TRS in which the kick from an individual slice was incorrectly modulated by the local beta function: Step 3 of the beam-beam kick (Eq. (16)) was coded as

$$x' \to x' + (\beta_{x-}(s_c)/\beta^*_{x-})\,\Delta x', \qquad y' \to y' + (\beta_{y-}(s_c)/\beta^*_{y-})\,\Delta y' \qquad \text{(incorrect!)} \tag{21}$$

Other than this difference, all tracking conditions were identical to those used in Figs. 2 and 3. One can see clear differences: the vertical amplitudes reach out to ~ 3 in Fig. 4 rather than to ~ 1.5 in Figs. 2 and 3, and the vertical spectra are substantially different.

As discussed in Sec. 3, Step 4 ("disruption") of the algorithm for the thick lens beam-beam interaction makes the sequence of kicks experienced by the tracked particle noncommutative. The second set of results in Fig. 4 shows the results of deliberately (and incorrectly) reversing the sequence of kicks experienced by the positron for the case $N_s = 5$. As in the previous example, there was no other difference in the tracking conditions from those used in Figs. 2 and 3. The phase spaces are not substantially different, but the vertical spectra are clearly different at the low end.

5. Comparison with analytic results

In this section we compute the tune shift as a function of amplitude obtained from single-particle tracking with TRS and compare the results with first-order perturbation theory calculations. Again, we completely neglect radiation damping and quantum excitation and we use the thin-lens approximation, *i.e.* we take $N_s = 1$ slice in the beam-beam kick algorithm. Depending on the case studied, the particle may or may not perform synchrotron oscillations.

Case with no synchrotron motion. In this case the positron that is being tracked collides at the IP with a single-slice electron bunch. The rms beam sizes of the electron bunch at the IP σ_{x-} and σ_{y-} are understood to be evaluated at the IP.

The analytic calculation we use is described in Ref. [15], except for one detail which we will clarify below. The first step is to recall that the electromagnetic kick from one slice can be written as a two-dimensional vector as

$$(\Delta x', \Delta y') = -\frac{r_e N_-}{2\gamma_+}\,(\mathbf{E} + \mathbf{v}_+ \times \mathbf{B}) = -\frac{r_e N_-}{\gamma_+}\,\mathbf{E} \tag{22}$$

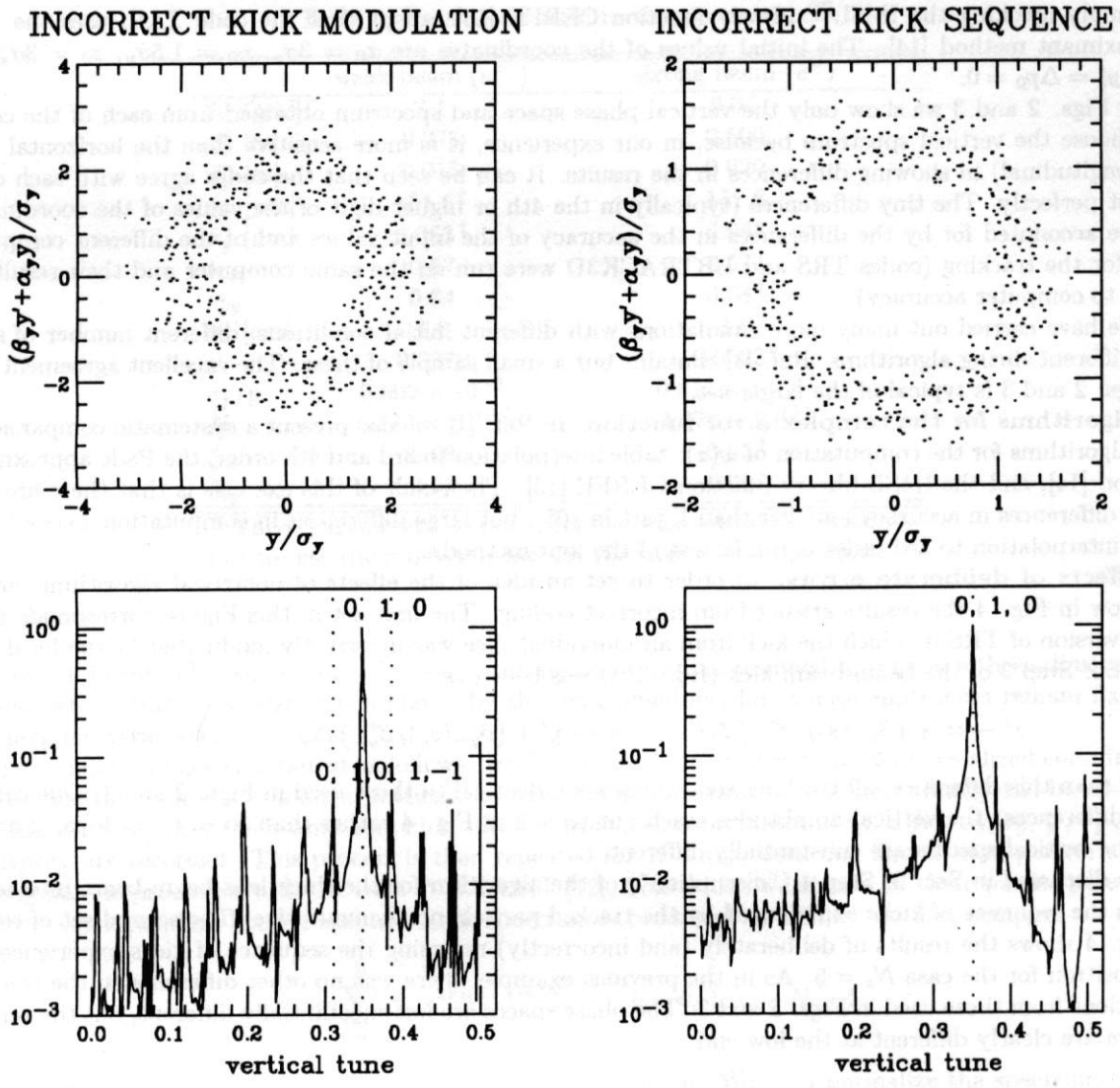

Figure 4: Single particle tracking with two deliberate errors: incorrect modulation of the kicks (Eq. (21), or inverted kick sequence (TRS, $N = 512$, $N_s = 5$, slicing alg. #2).

where the subscripts + and − refer to positrons and electrons, respectively. The electric field per unit charge produced by the electron beam, $\mathbf{E}(x, y, \sigma_{x-}, \sigma_{y-})$, is the solution of Poisson's equation, $\nabla \cdot \mathbf{E} = 4\pi\rho_t$, where $\rho_t(x, y, \sigma_{x-}, \sigma_{y-})$ is the transverse gaussian density, Eq. (18) (since the bunch is represented by a single slice, $\Delta N_- = N_-$). The fact that the magnetic and electric terms in the Lorentz force are equal is a consequence of the extreme relativistic approximation used (we also assume that the positron velocity $\mathbf{v}_+$ is antiparallel to the electron bunch velocity).

If we define the potential V as $\mathbf{E} = -\nabla V$, then the "phase averaged beam-beam parameter" (our nomenclature) of the kicked positron is given by [15]

$$\xi_i = -\frac{r_e N_-}{2\pi\gamma_+}\frac{\partial T_{00}}{\partial I_i}, \qquad i = x, y \tag{23}$$

where T_{00} is defined by

$$T_{00} = \int_0^{2\pi}\frac{d\theta_x}{2\pi}\int_0^{2\pi}\frac{d\theta_y}{2\pi}\, V\left(\sqrt{2\beta^*_{x+}I_x}\cos\theta_x, \sqrt{2\beta^*_{y+}I_y}\cos\theta_y\right) \tag{24a}$$

$$\equiv \left\langle V\left(\sqrt{2\beta^*_{x+}I_x}\cos\theta_x, \sqrt{2\beta^*_{y+}I_y}\cos\theta_y\right)\right\rangle \tag{24b}$$

Here the I's and θ's are the amplitudes and phases of the positron, respectively. The tune shifts of the positron $\Delta\nu_i$ are then obtained by solving the usual equations

$$\cos\left(2\pi(\nu_{0i} + \Delta\nu_i)\right) = \cos(2\pi\nu_{0i}) - 2\pi\xi_i \sin(2\pi\nu_{0i}), \qquad i = x, y \tag{25}$$

where the ν_{0i}'s are the "bare lattice" tunes.

In Ref. [15] the ξ's are assumed to be small enough that the approximation $\Delta\nu_i = \xi_i$ (which follows from Eq. (25) for small enough ξ) is valid. Hence in this approximation $\Delta\nu_i$ is given directly by Eq. (23). Our approach, which involves the extra step (25), can be thought of as a different perturbation expansion that reduces to the conventional one in the small-ξ limit, but that yields *the exact result when the perturbation force is linear.*[3]

It should be noted that $\sqrt{2\beta^*_{x+}I_x}$ and $\sqrt{2\beta^*_{y+}I_y}$ in Eq. (24) are nothing but the injection amplitudes x_0 and y_0 of the positron, respectively (we recall that in all our calculations the initial slopes vanish, $x'_0 = y'_0 = 0$). Therefore, by using the chain rule $\partial/\partial I_y = (\beta^*_{y+}/y_0)\partial/\partial y_0$ and $\mathbf{E} = -\nabla V$ we obtain

$$\xi_y = -\frac{r_e N_- \beta^*_{y+}}{2\pi\gamma_+ y_0}\frac{\partial}{\partial y_0}\left\langle V\left(x_0\cos\theta_x, y_0\cos\theta_y\right)\right\rangle \tag{26a}$$

$$= \left\langle 2\cos^2\theta_y\, \xi_{y\ell}\left(x_0\cos\theta_x, y_0\cos\theta_y\right)\right\rangle \tag{26b}$$

and similarly for ξ_x. We have defined the "local vertical beam-beam parameter" $\xi_{y\ell}(x, y)$ as

$$\Delta y'(x, y) \equiv -4\pi\xi_{y\ell}(x, y)\frac{y}{\beta^*_{y+}} \tag{27}$$

where $\Delta y'(x, y)$ is given by Eq. (22).

As an example, we have used the PEP-II–like parameters listed in Table 3. As before, we tracked the particle with TRS for $N = 512$ turns, used one kick ($N_s = 1$), and used the IMSL® library [13] to compute $w(z)$. Radiation damping and quantum excitation were wholly neglected. The tune was computed with PORTRAIT. The tracked particle was injected with $x_0 = z_0 = 0$, and the vertical amplitude was varied in the range $0 \le y_0 \le 10\sigma_y$. For the analytic calculation, we integrated numerically Eq. (26b). Results are shown in Fig. 5. The agreement is almost perfect.

[3] One of us (MF) is indebted to Étienne Forest for a discussion on this point.

In Ref. [1] we also carried out this exercise for a round beam. In this case the phase integrals can be carried out and the result expressed in closed form. The agreement between tracking and the analytic result is also excellent.

Case with synchrotron motion. In case when the positron is performing synchrotron oscillations, it collides against the opposing thin-slice electron bunch at a longitudinal coordinate $s_c = z/2$ (see Eq. (14)) where z is the positron's longitudinal coordinate at the time of the collision. Thus the vertical kick it receives at the collision point (x, y, s_c) is given by

$$\Delta y'(x, y, s_c) = -\frac{r_e N_-}{\gamma_+} E_y\left(x, y, \sigma_{x-}(s_c), \sigma_{y-}(s_c)\right) \tag{28}$$

and similarly for $\Delta x'$. Here E_y is computed by using the actual beam sizes $\sigma_{x-}(s_c)$ and $\sigma_{y-}(s_c)$ of the electron bunch at the collision point, given by Eq. (17). Therefore it seems clear that the generalization to the present case of the phased-averaged vertical beam-beam parameter is

$$\xi_y = \left\langle 2\cos^2\theta_y\, \xi_{y\ell}\left(x_0\cos\theta_x, y_0\cos\theta_y, (z_0/2)\cos\theta_z\right)\right\rangle \tag{29}$$

where the local vertical beam-beam parameter $\xi_{y\ell}$ is defined by

$$\Delta y'(x, y, s_c) \equiv -4\pi\xi_{y\ell}(x, y, s_c)\frac{y}{\beta_{y+}(s_c)} \tag{30}$$

with a similar expression for the horizontal counterpart. Note that the phase average $\langle\cdots\rangle$ is now three dimensional,

$$\langle\cdots\rangle = \int_0^{2\pi}\frac{d\theta_x}{2\pi}\int_0^{2\pi}\frac{d\theta_y}{2\pi}\int_0^{2\pi}\frac{d\theta_z}{2\pi}\,(\cdots) \tag{31}$$

and that the beta function in Eq. (30) has the appropriate s_c-dependence.

Case when the positron is close to the axis. Fig. 5 shows the tracking results and analytic calculation of the vertical tune plotted as a function of the longitudinal launching amplitude z_0 of the positron (z_0 is normalized to the rms bunch length of the opposing bunch). The particle is tracked with TRS for $N = 512$ turns, with $N_s = 1$, using the IMSL® library calculation of $w(z)$ [13]. The particle is launched close to the beam axis ($x_0 = 0$, $y_0 = \sigma_y/10$), with $x_0' = y_0' = \Delta p_0 = 0$, and z_0 is varied in the range $0 \le z_0/\sigma_z \le 20$.

The three cases displayed in Fig. 5 correspond to different ratios of the beta functions of the two beams (in all 3 cases, however, the beams have the same aspect ratio, $\sigma_x/\sigma_y = 25$). These are dubbed "symmetric," "nominal," and "high asymmetry." The nominal case is exactly the same as that displayed in Table 3. The number of particles per bunch in all three cases are adjusted so that the nominal beam-beam parameters remain fixed at 0.03. Table 4 lists the relevant parameters.

In the three cases the beta functions at the IP of the positron beam are held fixed, and so is the beta-function ratio for each beam, namely $\beta_x^*/\beta_y^* = 25$. Similarly, the beam aspect ratio at the IP is fixed: $\sigma_x/\sigma_y = 25$ for all cases. What changes from one case to the next is the ratio of the beta function of one beam relative to the other: the ratio β_-^*/β_+^* takes on the values 1, 1.333... and 2.666... for the symmetric, nominal and high asymmetry cases, respectively. If the positron did not perform synchrotron oscillations, it is a priori obvious that the tune shift would be the same in all three cases. However, the fact that the beta functions of the *electron beam* are different makes the modulation of the *positron* beam-beam parameter vary from case to case due to the differences in the hourglass effect [16]. In fact, for a flat beam, a simple analytic calculation for the vertical beam-beam parameter of a positron oscillating longitudinally with maximum amplitude z_0 and with $x_0 \simeq y_0 \simeq 0$ shows [16] that $\xi_{y+}(z_0)$ scales like $\xi_{y+}(z_0) \sim \beta_{y+}(z_0/2)/\sqrt{\beta_{y-}(z_0/2)}$. This scaling shows that $\xi_{y+}(z_0)$ grows linearly when $z_0 \gtrsim \beta_{y-}^*$. Also, if β_{y+}^* is kept fixed, as we do in Table 4, the tune shift is larger the larger is β_{y-}^*. Actually, if this scaling formula (properly normalized) is inserted into Eq. (25), the resultant vertical tune is in good qualitative agreement with the more accurate calculations shown in Fig. 5.

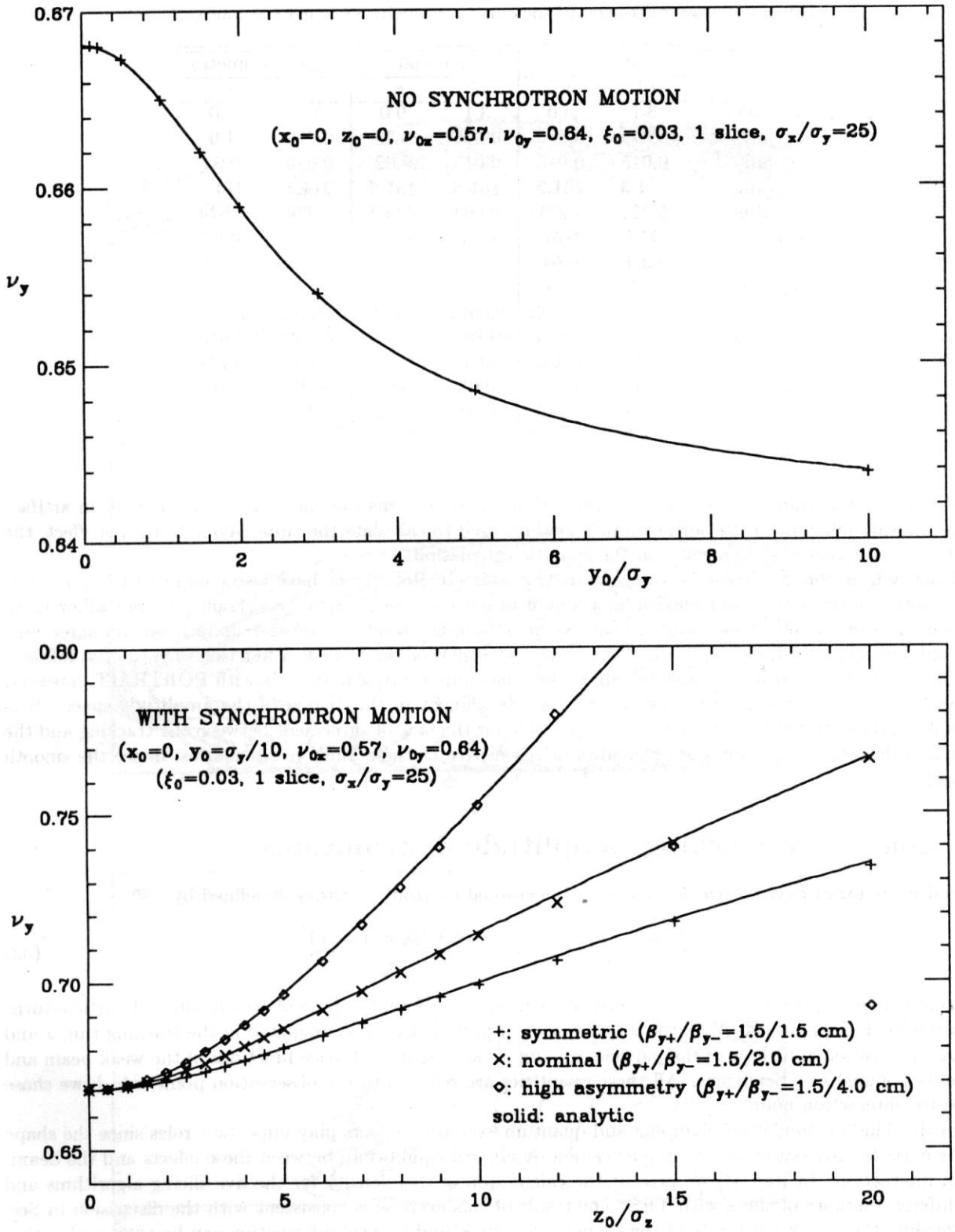

Figure 5: Top: vertical tune *vs.*vertical amplitude with no synchrotron motion; bottom: vertical tune *vs.*longitudinal amplitude for fixed (but small) vertical amplitude. Tracking results (crosses and diamonds) for a single positron colliding against a thin-lens electron beam were obtained with TRS with $N_s = 1$. In all cases the electron beam aspect ratio is $\sigma_x/\sigma_y = 25$; the differences between the three sets of data in the bottom figure are due to the hourglass effect.

Table 4: Parameters used in the three cases with synchrotron motion.

	symmetric		nominal		high asymmetry	
	e^+	e^-	e^+	e^-	e^+	e^-
E [GeV]	3.1	9.0	3.1	9.0	3.1	9.0
β_x^* [m]	0.375	0.375	0.375	0.50	0.375	1.0
β_y^* [m]	0.015	0.015	0.015	0.02	0.015	0.04
σ_x [μm]	131.3	131.3	151.6	151.6	214.4	214.4
σ_y [μm]	5.251	5.251	6.063	6.063	8.574	8.574
ν_{0x}	0.57	0.57	0.57	0.57	0.57	0.57
ν_{0y}	0.64	0.64	0.64	0.64	0.64	0.64
σ_z [cm]	1.0	1.0	1.0	1.0	1.0	1.0
ν_s	0.0372	0.0523	0.0372	0.0523	0.0372	0.0523
σ_p/p [10^{-3}]	0.809	0.615	0.809	0.615	0.809	0.615
N [10^{10}]	5.630	1.939	5.630	2.586	5.630	5.171
ξ_{0x}	0.03	0.03	0.03	0.03	0.03	0.03
ξ_{0y}	0.03	0.03	0.03	0.03	0.03	0.03

For the high asymmetry case, Fig. 5 shows that the tune turns over at $z_0/\sigma_z \gtrsim 12$. This is an artifact of the aliasing inherent in the turn-counting method used to calculate the tune. Aside from this effect, the results are in excellent agreement with the analytic calculation.

Case when the positron is away from the axis. In Ref. [1] we have also computed the tune shift when both the transverse and longitudinal amplitudes are nonzero. Space constraints do not allow us to present the results here. The result is that, when $z_0 > 0$, the tracking and the analytic results agree very well only for small values of y_0. In fact, the tracking results for the tune as a function of y_0 do not follow a smooth curve. In contrast, the analytic curves do behave smoothly. An analysis with PORTRAIT, however, shows that the synchrotron sidebands $\nu_y \pm \nu_s$ are prominent in this region of the amplitude space. It is virtually certain that these sidebands are responsible for the lack of agreement between the tracking and the analytic calculations (the analytic calculation is insensitive to these kinds of resonances, hence the smooth curves).

6. Long-term tracking: amplitude distributions

One-dimensional distributions. The one-dimensional horizontal density is defined by

$$\frac{1}{N_0}\frac{dN}{d\hat{A}_x^2}, \quad \text{with} \quad \hat{A}_x^2 \equiv \frac{x^2 + (\beta_x x' + \alpha_x x)^2}{\sigma_x^2} \tag{32}$$

with corresponding expressions for the vertical counterparts. Here N represents the number of particle-turns at normalized amplitude $\hat{A}$, N_0 is the total number of particle-turns accumulated in the tracking run, x and x' are the position and slope of the particle, α_x and β_x are the usual lattice functions of the weak beam and σ_x is its nominal rms beam size. All these quantities are referred to the observation point, which we chose to be the interaction point.

In this kind of simulation, damping and quantum excitation effects play important roles since the shape of the particle distribution is a consequence of a dynamical equilibrium between these effects and the beam-beam interaction. In Ref. [1] we present the calculation of this density for the five slicing algorithms and for different number of slices with TRS. The result of this exercise is consistent with the discussion in Sec. 2 regarding the convergence rate of the slicing algorithms, and no new information can be extracted within the accuracy of the calculation.

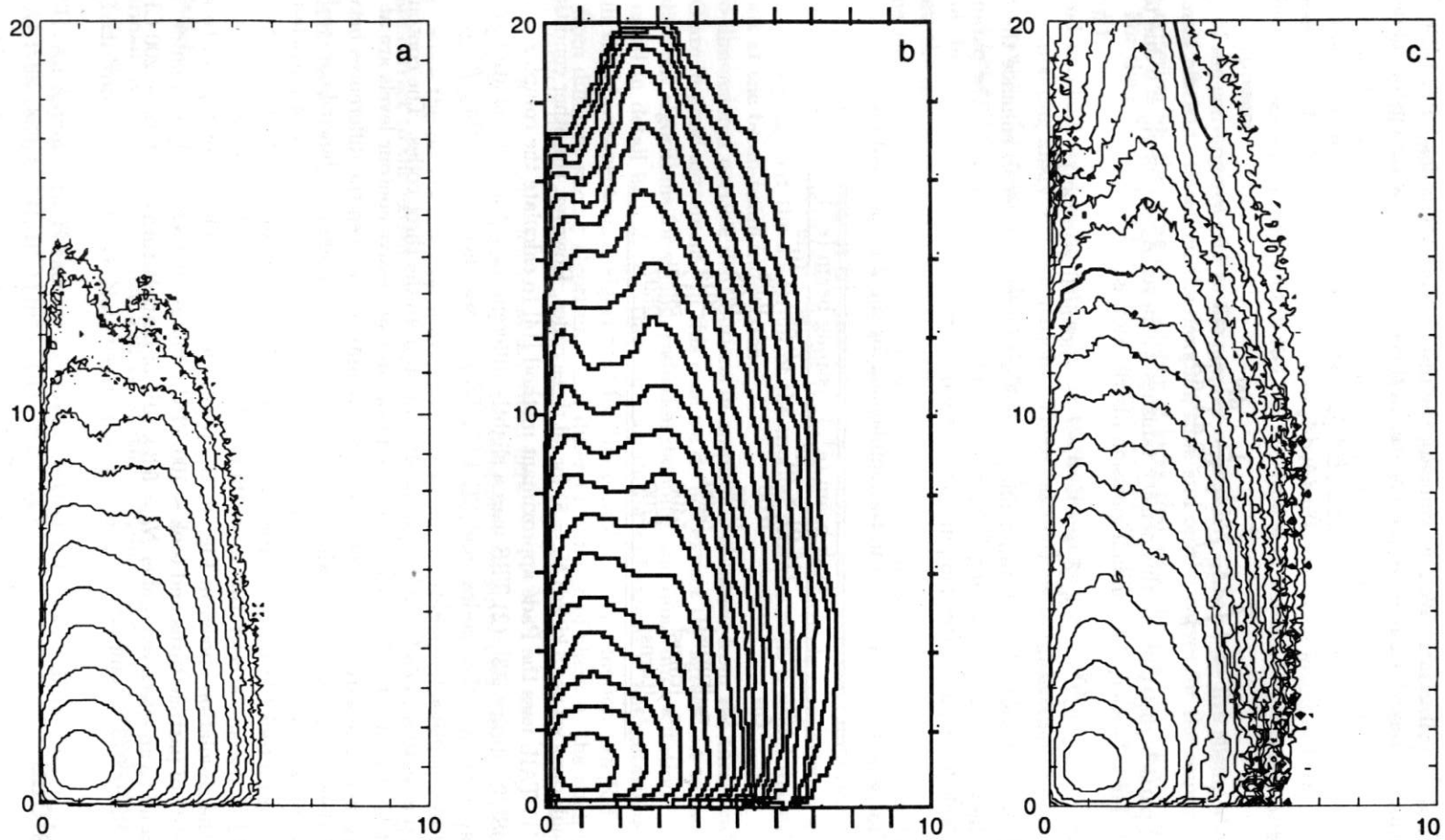

Figure 6: The 2-D amplitude distribution. (a): TRS; (b): LIFETRAC; (c): TAIL. All three cases use 5 kicks; other conditions are described in the text.

Two-dimensional distribution. We now compare the results from the codes TRS, LIFETRAC and TAIL for the 2-dimensional distribution in $(\hat{A}_x, \hat{A}_y)$ space. In this case, we follow the custom of dealing with the density

$$\frac{1}{N_0}\frac{dN}{d\hat{A}_x d\hat{A}_y} \tag{33}$$

which is normalized to unity,

$$\int_0^\infty d\hat{A}_x \int_0^\infty d\hat{A}_y \, \frac{1}{N_0}\frac{dN}{d\hat{A}_x d\hat{A}_y} = 1 \tag{34}$$

For any physical particle distribution, this density vanishes whenever $\hat{A}_x = 0$ or $\hat{A}_y = 0$ due to a zero of the volume element. For reference, the nominal gaussian distribution is

$$\frac{1}{N_0}\frac{dN}{d\hat{A}_x d\hat{A}_y} = \hat{A}_x \hat{A}_y \, e^{-(\hat{A}_x^2+\hat{A}_y^2)/2} \qquad \text{(nominal gaussian)} \tag{35}$$

For the simulation we choose a large beam-beam parameter of 0.08 in order to enhance the tails of the distribution. We achieve this value by scaling N by a factor of 8/3 relative to Table 3. The parameters that are different from Table 3, including the damping times, are displayed in Table 5.

Table 5: Parameters used in the simulations for the 2-D distributions.

	weak beam (e^+)	strong beam (e^-)
N	15.01×10^{10}	6.895×10^{10}
ξ_{0x}	0.08	0.08
ξ_{0y}	0.08	0.08
τ_x [turns]	5400	5014
τ_y [turns]	5400	5014
τ_z [turns]	2700	2507

In these 2-D simulations we use 5 kicks ($N_s = 5$) for all three codes. However, the other conditions are not exactly the same: (1) TAIL uses the Padé approximant method [14] to calculate the complex error function rather than the IMSL® library [13]; (2) TRS uses a slightly different algorithm for radiation damping and quantum excitation from the other codes; and (3) LIFETRAC uses slicing algorithm #5 as opposed to algorithm #2 used by the other two codes.

Figure 6 shows the contour plots for the resultant simulation from the three codes. The contour levels are as follows: the first level is at a height $1/\sqrt{e}$ below the peak, and successive contour levels are at a constant ratio e below each other. The agreement among the codes is quite good given the differences between them.

The code TRS does "brute force" tracking. For the particular simulation shown here, we used 1,024 particles and tracked them for 500,000 turns. Thus we accumulated a total number of particle-turns $N_0 = 0.512 \times 10^9$. The program took 818 CPU minutes to run on the Cray-2S/8128 at NERSC. On the other hand, LIFETRAC and TAIL use an "acceleration algorithm" [17] that optimizes the generation of the tails of the distribution. For the simulation shown in Fig. 6, the results from LIFETRAC correspond to an effective number $N_0 = 4 \times 10^{11}$ of particle-turns and took $\sim$ 100 CPU minutes on a VAX-6610 computer. The results from TAIL correspond to an effective number $N_0 = 6.3 \times 10^{11}$ of particle-turns and took $\sim$ 200 CPU minutes to run on an IBM RS6000/375 computer.

7. Conclusions

We have described a methodical comparison of four beam-beam codes with each other and with analytic calculations. We have carried out single-particle and multiparticle tracking calculations and have computed

the tune shifts with amplitude and the particle density distribution. In general, the agreement is almost perfect when the comparison is meaningful, and the tiny differences can be traced to round-off errors. We have studied the thin and thick lens approximations for the beam-beam interaction in weak-strong mode, different slicing algorithms, and different ways of computing the complex error function. This article is a brief summary of Ref. [1]; more details and more cases studied can be found in there. The good agreement exhibited by the cases shown here and in Ref. [1] are typical of a much larger set that space constraints do not allow us to present.

A study of the convergence rate as the number of kicks $N_s \to \infty$ of the five slicing algorithms shows that #4 is the most efficient. Based on the damping time and on the curves for the convergence rates, we have provided a criterion for the minimum number of kicks that must be used in a given situation for a given algorithm. For the case of the PEP-II nominal design, the adequate number of kicks is 3 for algorithm #4, and 15 for #1.

We found excellent agreement between the tracking results for the tune as a function of amplitude and the corresponding analytical calculations. These calculations were done for one slice, with or without synchrotron motion, for round and for flat beams. We found a discrepancy only in the case when the amplitudes of betatron and synchrotron oscillations are *both* large. In this case, however, the synchrotron sidebands of the vertical tune are prominent. Since the analytic calculation does not take these sidebands into account, the discrepancy is not meaningful.

By using the fourier spectrum of the single-particle motion as a probe, we uncovered errors in earlier versions of the code TRS. It turns out, however, that these errors lead to only minor effects in the multiparticle simulations carried out for PEP-II [2]. However, they might have been more important in other situations. One of our main motivations in carrying out the detailed single-particle comparisons was to look for these errors. It is gratifying that the spectrum of the motion provides such a useful magnifying glass through which to look at the beam-beam interaction.

The two-dimensional particle distributions in amplitude obtained from the three codes TRS, TAIL and LIFETRAC are in good agreement. In this case we do not expect the agreement to be perfect because the codes use different algorithms for slicing, radiation damping and quantum excitation.

As discussed in detail in Ref. [1], there are significant differences in computational speed (but not in accuracy) in the above-mentioned algorithms for the complex error function. In Ref. [1] we also discuss the effects from different slicing algorithms and different number of slices in the computation of the one-dimensional particle distributions; the conclusions from this particular exercise, however, are subsumed by those reached from the other calculations described here.

In summary, we have exhibited results in good agreement obtained with four different beam-beam codes. Although these codes are optimized for different purposes, it is clear that their basic "engines" are doing the same thing. Since the results also are in excellent agreement with analytical calculations, we conclude that the codes are correct to the extent that they involve the same approximations used in these calculations.

8. Acknowledgments

We are grateful to NERSC for supercomputer support.

References

[1] M. Furman, A. Zholents, T. Chen and D. Shatilov, "Comparisons of Beam-Beam Code Simulations," CBP Tech Note-59/PEP-II AP Note 95.04, July 13, 1995.

[2] "PEP-II: An Asymmetric B Factory - Conceptual Design Report," June 1993, LBL-PUB-5379/SLAC-418/CALT-68-1869/UCRL-ID-114055/ UC-IIRPA-93-01.

[3] J. L. Tennyson, undocumented code "TRS," 1989.

[4] D. Shatilov, "Beam-Beam Simulations at Large Amplitudes and Lifetime Determination," BINP 92-79, Novosibirsk (in Russian).

[5] T. Chen, J. Irwin and R. Siemann, "Simulation of the Beam Halo from the Beam-Beam Interaction," Phys. Rev. **E 49**, 2323 (1994); "Simulation of the Beam Halo from the Beam-Beam Interaction in LEP," SLAC-PUB-6432, Feb. 1994, to be published in the Proc. 4th annual LEP performance workshop, Chamonix, France, Jan. 1994; "Simulation of the Beam-Beam Lifetime for LEP," SLAC-PUB-6561, June 1994, to be published in the Proc. 4th EPAC, London, England, June 27-July 1st., 1994.

[6] M. A. Furman, "The Beam-Beam code BBTRACK3D" (to be documented).

[7] J. L. Tennyson, "Tune Considerations for APIARY 6.3D," ABC-28, August 1991.

[8] K. Hirata, H. Moshammer and F. Ruggiero, "A Symplectic Beam-Beam Interaction with Energy Change," Part. Accel. **40**, 205 (1993).

[9] S. Krishnagopal, "Beam-Beam Dynamics with Round Beam Profiles," Ph. D. dissertation, Cornell University, January 1991.

[10] M. Bassetti and G. A. Erskine, "Closed Expression for the Electric Field of a Two-Dimensional Gaussian Charge," CERN-ISR-TH/80-06.

[11] M. A. Furman, "Compact Complex Expressions for the Electric Field of 2-D Elliptical Charge Distributions," Am. J. Phys. **62** (12), Dec. 1994, 1134–1140.

[12] M. A. Furman, "The Tracking Analysis Program PORTRAIT" (to be documented).

[13] IMSL Math/Library® Reference Manual, v. 10.0.

[14] Y. Okamoto and R. Talman, "Rational Approximation of the Complex Error Function and the Electric Field of a Two-Dimensional Charge Distribution," CBN 80-13, Sept. 1980.

[15] R. Siemann, "The Beam-Beam Interaction in e^+e^- Storage Rings," Proc. Joint US-CERN School on Particle Accelerators: *Frontiers of Particle Beams, Factories with e^+e^- Rings*, Benalmádena, Spain, October 1992, pp. 327–363 (Springer Verlag Lecture Notes in Physics no. 425, M. Dienes, M. Month, B. Strasser and S. Turner, eds.)

[16] M. A. Furman, "The Hourglass Reduction Factor for Asymmetric Colliders," ABC-21/ESG Tech Note 161, April, 1991 (rev. Aug. 1991); "Hourglass Effects for Asymmetric Colliders," LBL-30833, Proc. 1991 Particle Accelerator Conf., San Francisco, May 6–9, 1991, p. 422.

[17] J. Irwin, "Simulation of Tail Distributions in Electron-Positron Circular Colliders," Proc. Third Advanced ICFA Beam Dynamics Workshop (Beam-Beam Effects in Circular Colliders), I. Koop and G. Tumaikin, eds., Novosibirsk, May 29–June 3, 1989, p. 123.

Decoherence of a Gaussian Beam due to Beam-Beam Interaction

G.V.Stupakov *, V.V.Parkhomchuk, V.D.Shiltsev †

May 15, 1995

Abstract

Using both analytical and numerical approaches, we compute the decoherence function that describes decay of the betatron oscillations of the centroid of an initially offset beam due to head-on beam-beam collisions. Based on this function, the decoherence time is estimated for the Superconducting Super Collider. We also discuss several definitions of the decoherence time arising in different beam dynamics problems.

1. Introduction

When a beam is kicked transversely, its centroid experiences decaying betatron oscillations. the decay is related to the tune spread in the beam, which – depending on a particular case – can be caused by nonlinearity of the lattice, chromaticity of the ring, or beam-beam interaction. decoherence due to the first two sources of the tune spread has been previously studied by Meller *et. al* [1]. However, for the Superconducting Super Collider (SSC) at its full energy of 20 TeV, the main source of the tune spread in the beam comes from the beam-beam interaction. For example, at 20 TeV an effective tune spread is about $\cdot 10^{-4}$ [2],$2 \cdot 10^{-5}$ due to residual chromaticity [3], and about $5 \cdot 10^{-6}$ due to the lattice nonlinearity [3]. The effect is also important in the 8 TeV Large Hadron Collider in CERN.

In this paper, we analyze the decoherence that is produced by head-on beam-beam collisions in the model of strong weak beams and give estimates of the decoherence time.

The importance of the decoherence phenomenon is associated with the fact that in the course of the damping of betatron oscillations the transverse emittance of the beam increases. Characteristic time associated with the damping determines a scale on which coherent oscillations transform to an increment of the emittance. This time is one of the key parameters required for the design of the feedback system needed to suppress emittance growth of the beam [2, 3, 4, 5]. We use two approaches to attack the problem. The first is based on an analytical consideration that reduces the problem of decoherence

*SLAC, Stanford, CA, USA
†Budker INP, 630090, Novosibirsk, RUSSIA

to calculation of a 3-dimensional integral. In addition, we performed a computer simulation in which an ensemble of particles was tracked a linear lattice subject to beam-beam interaction. Both methods gave results that agree fairly well with one another.

2. Analytical Consideration

Let us consider two colliding proton round beams with a Gaussian distribution function characterized by the rms beam width σ. due to beam-beam head-on collisions, a particle of a beam having the betatron amplitudes a_x and a_y in x and y directions, respectively, acquires a tune shift in x-direction, equal to [6]

$$\Delta\nu_x(\alpha_1,\alpha_2) = -\xi \int_0^1 du e^{-u(\alpha_1+\alpha_2)} I_0(\alpha_2 u)[I_0(\alpha_1 u) - I_1(\alpha_1 u)], \tag{1}$$

where $\alpha_1 = a_x^2/4\sigma^2$, $\alpha_2 = a_y^2/4\sigma^2$, $I_n(z)$ is the modified Bessel function of the n-th order, and ξ is the usual tune shift parameter, with $\xi = N_p r_p/4\pi\epsilon$, where N_p is the number of particles in the bunch, r_p is the classical proton radius, and ϵ is the normalized emittance. Note that $\Delta\nu_x$ is negative for collisions of particles having the same charge sign. Because of the axial symmetry of the problem, all of our equations remain valid when $x \to y$ and $y \to x$.

In terms of the variables α_1 and α_2, the distribution function of the Gaussian beam has the form

$$\rho(\alpha_1,\alpha_2) = 4e^{-2(\alpha_1+\alpha_2)}, \tag{2}$$

where $\rho(\alpha_1,\alpha_2)$ is normalized so that

$$\int_0^\infty \int_0^\infty \rho(\alpha_1,\alpha_2) d\alpha_1 d\alpha_2 = 1. \tag{3}$$

Using Eqs. (1) and (2) one can find a distribution function over the tune shift, $f(\Delta\nu_x)$, such that $f(\Delta\nu_x)d\Delta\nu_x$ gives the probability for a particle to have the tune shift $\Delta\nu_x$ within the range $d\Delta\nu_x$. The function $f(\Delta\nu_x)$ is given by the following integral:

$$f(\Delta\nu_x) = \int_0^\infty \int_0^\infty \rho(\alpha_1,\alpha_2)\delta(\Delta\nu_x - \Delta\nu_x(\alpha_1, d\alpha_2)) d\alpha_1 d\alpha_2. \tag{4}$$

Given $f(\Delta\nu_x)$, the average values $< \Delta\nu_x >$ and $< (\Delta\nu_x)^2 >$ are reduced to the following integrals

$$< \Delta\nu_x >= \int \Delta\nu_x f(\Delta\nu_x) d\Delta\nu_x = \int_0^\infty \int_0^\infty \rho(\alpha_1,\alpha_2)\Delta\nu_x(\alpha_1,\alpha_2) d\alpha_1 d\alpha_2, \tag{5}$$

$$< (\Delta\nu_x)^2 >= \int (\Delta\nu_x)^2 f(\Delta\nu_x) d\Delta\nu_x = \int_0^\infty \int_0^\infty \rho(\alpha_1,\alpha_2)\Delta\nu_x^2(\alpha_1,\alpha_2) d\alpha_1 d\alpha_2, \tag{6}$$

with the rms spread $\delta\nu_x$ given by

$$\delta\nu_x = \sqrt{< (\Delta\nu_x)^2 > - < \Delta\nu_x >^2}. \tag{7}$$

3. Decoherence Function

The most complete description of the decoherence process is provided by so-called decoherence function that describes evolution of the beam centroid of a kicked beam. Let $\eta = x_c/\sqrt{\beta}$, where x_c is the centroid offset and β is the beta function. The decoherence function $K(N)$ is defined in Ref. [6] as

$$K(N) = \frac{\eta(N)}{\Delta\theta\sqrt{\beta_0}}, \tag{8}$$

where n is the number of turns, $\Delta\theta$ is the initial kick angle, and β_0 refers to the location of the kick. A mathematical expression for the decoherence function that corresponds to an infinitesimally small initial kick has been derived in Ref. [7]. For our purposes it can be written as follows:

$$K(N) = \int_{-\infty}^{\infty} \sin\left(2\pi N(\nu_{x0} + \Delta\nu_x)\right) f(\Delta\nu_x) d\Delta\nu_x = Im e^{2i\pi N\nu_{x0}} \int_{-\infty}^{\infty} e^{2i\pi N\Delta\nu_x} f(\Delta\nu_x) d\Delta\nu_x, \tag{9}$$

where ν_{x0} is the unshifted tune of the beam. We restrict our attention here to considering only the modulus $\mathcal{K}(N)$ of the complex integral in Eq. (9); it has a meaning of the envelope (or amplitude) of the betatron oscillations produced by the initial kick,

$$\mathcal{K}(N) = \left| \int_{-\xi}^{0} e^{2i\pi N\Delta\nu_x} f(\Delta\nu_x) d\Delta\nu_x \right| =$$

$$= 4 \left| \int_0^{\infty} \int_0^{\infty} \exp\left(-2(\alpha_1 + \alpha_2) + 2\pi i N \Delta\nu_x(\alpha_1, \alpha_2)\right) d\alpha_1 d\alpha_2 \right|. \tag{10}$$

In Eq.(10) we explicitly took into account that the beam-beam interaction produces a tune shift in the range $-\xi < \Delta\nu_x < 0$. It is interesting to note that the tune spread $\delta\nu_x$ (see Eq. (7)) can be related to the second derivative of $\mathcal{K}(N)$ at $N = 0$,

$$\delta\nu_x = \frac{1}{2\pi} \sqrt{-\frac{d^2\mathcal{K}}{dN^2}}\Bigg|_{N=0}. \tag{11}$$

4. Results of the Calculations

We computed the decoherence function $\mathcal{K}(N)$ by two methods. In the first, we numerically integrated Eqs. (1) and (10), which together constitute a 3-dimensional integral. In the second, we performed a computer simulation in which an ensemble of up to $2 \cdot 10^5$

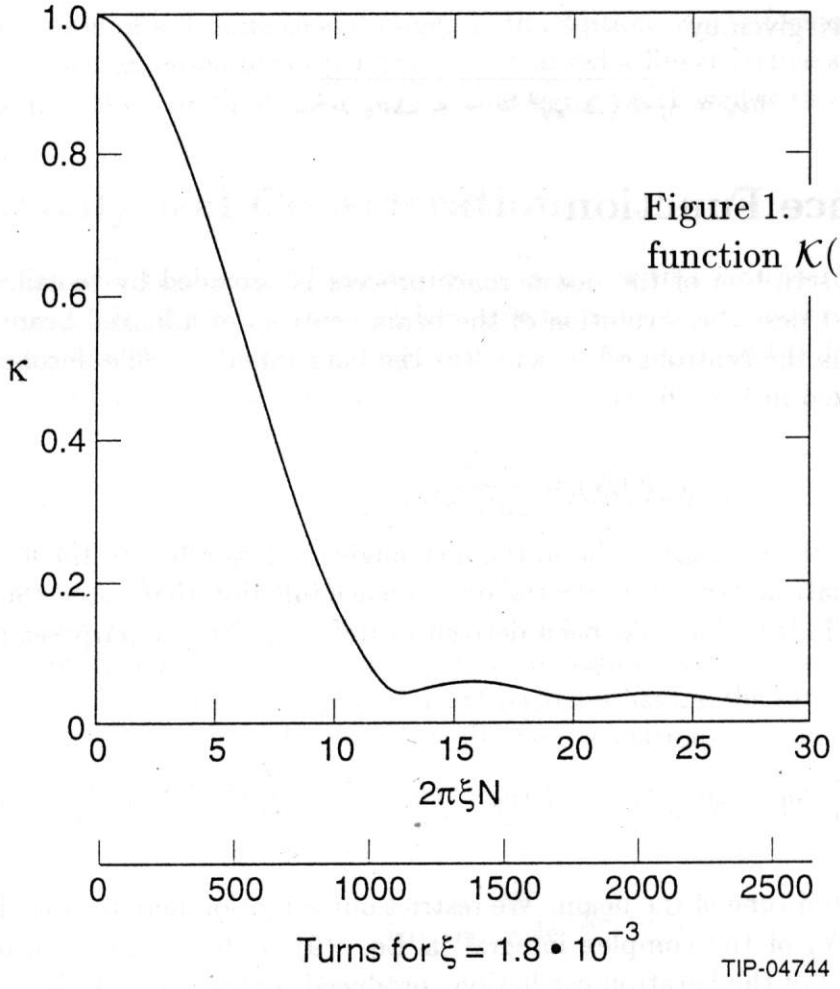

Figure 1. Decoherence function $\mathcal{K}(N)$ vs. $2\pi N\xi$.

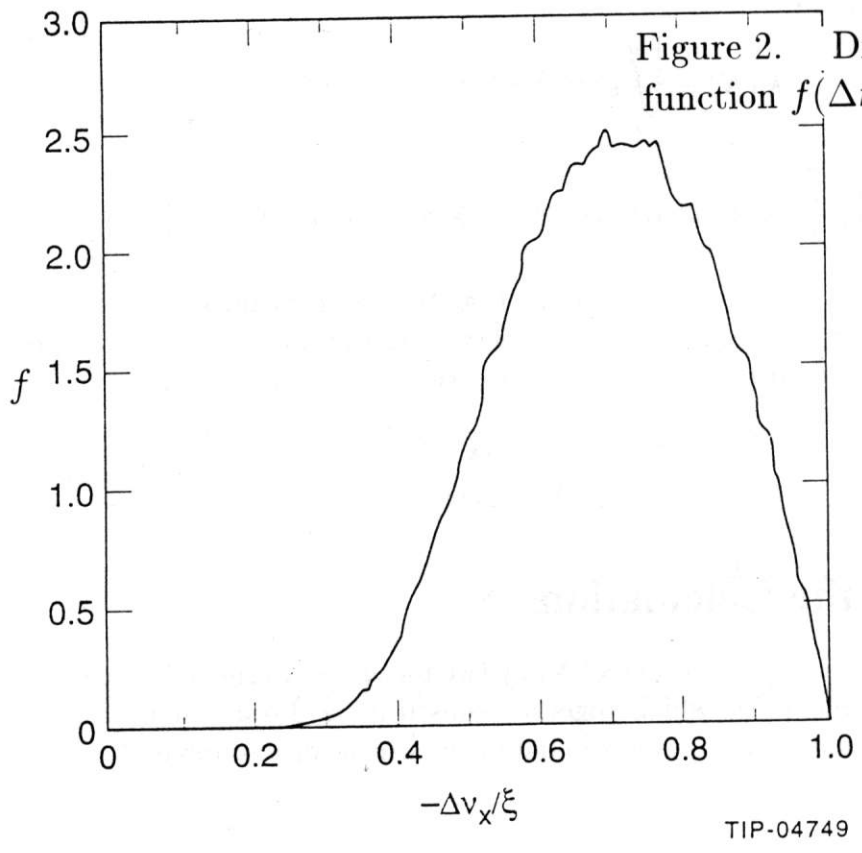

Figure 2. Distribution function $f(\Delta\nu_x)$.

particles with an initial Gaussian distribution function has been tracked several thousand turns subject to a standard linear transfer map, followed by a kick due to the beam-beam interaction. The distribution function $f(\Delta\nu_x)$ of the ensemble has been computed, and with the use of the first part of Eq. (10), $\mathcal{K}(N)$ has been calculated by means of numerical integration. Both methods agree with one another within several percent.

The function $\mathcal{K}(N)$ obtained as mentioned above is plotted in Fig.1 as a function of the variable $2\pi N\xi$. On the same plot we also show a scale with number of turns N corresponding to $\xi = 1.8 \cdot 10^{-3}$ – the nominal value of ξ for the SSC with two interaction regions.

Fig. 2 shows the distribution function $f(\Delta\nu_x)$ found from the tracking simulations. This curve is not ideally smooth (as it has to be) simply because of the limited number of particles used in the simulations. The average values characterizing this function are

$$< \Delta\nu_x >= -0.633\xi, \quad \sqrt{< (\Delta\nu_x)^2 >} = 0.655\xi, \quad \delta\nu_x = 0.167\xi. \tag{12}$$

For comparison, we have also computed decoherence curves for large amplitudes of the initial kick. These curves are plotted in Fig.3 (together with $\mathcal{K}(N)$ from Fig.1) for initial kicks equal to σ and 4σ. They demonstrate the general trend of slower decoherence for stronger kicks.

5. Decoherence Time

Having found the decoherence curve we are now in a position to estimate the decoherence time for the decay of an initial kick. Notice that there is no unique, rigorous definition of the decoherence time. In this section, we present several definitions that arise in different beam dynamics problems.

One can simply define the decoherence time (number of turns) N_{decoh}, as the time needed for the amplitude to go down to half of its initial value, $\mathcal{K}(N_{decoh} = 0.5$. From Fig.1, one finds the following estimate for N_{decoh} so defined:

$$N_{decoh} \approx \frac{1}{\xi}. \tag{13}$$

For the SSC collider, where $\xi = 1.8 \cdot 10^{-3}$, this gives $N_{decoh} = 600$ turns.

For a feedback theory, a more relevant definition is associated with the behavior of $\mathcal{K}(N)$ in the region of small N. This is easy justify if one takes into account that a strong feedback systems damps the beam oscillations much more quickly before they decohere.This implies that the only an initial phase of the decoherence process is involved in the residual emittance growth of the beam [4]. Because $\mathcal{K}(N)$ has a quadratic dependence in the limit $N \to 0$, an adequate definition of N_{decoh} in this case is

$$N_{dec} = \left.\frac{1}{\sqrt{-\mathcal{K}''}}\right|_{N=0} = \frac{1}{2\pi\delta\nu_x}, \tag{14}$$

so that $\mathcal{K}(N) = 1 - 1/2(N/N_{decoh})^2$ for $N \ll N_{decoh}$. Our calculations give

$$N_{decoh} = \frac{0.95}{\xi}, \tag{15}$$

which results in $N_{decoh} = 530$ for the SSC.

Yet another N_{decoh} is related to the effect of external noise acting on the beam (without feedback). Assume that at each turn the beam experiences random, uncorrelated kicks of amplitude a_m. Its displacement after N turns is given by

$$\Delta x_c(N) = \sum_{m=1}^{N} K(N-m)a_m. \tag{16}$$

Let us find the average square of the displacement:

$$< (\Delta x_c)^2 >= \sum_{m=1}^{N} K^2(N-m) < a_m^2 >=< a^2 > \sum_{m=1}^{N} K^2(m), \tag{17}$$

where we have employed the condition of uncorrelated kicks $< a_m a_n >=< a^2 > \delta_{mn}$. Now we define the decoherence time N_{decoh} so that

$$< (\Delta x_c)^2 >= \frac{1}{2} N_{decoh} < a^2 > . \tag{18}$$

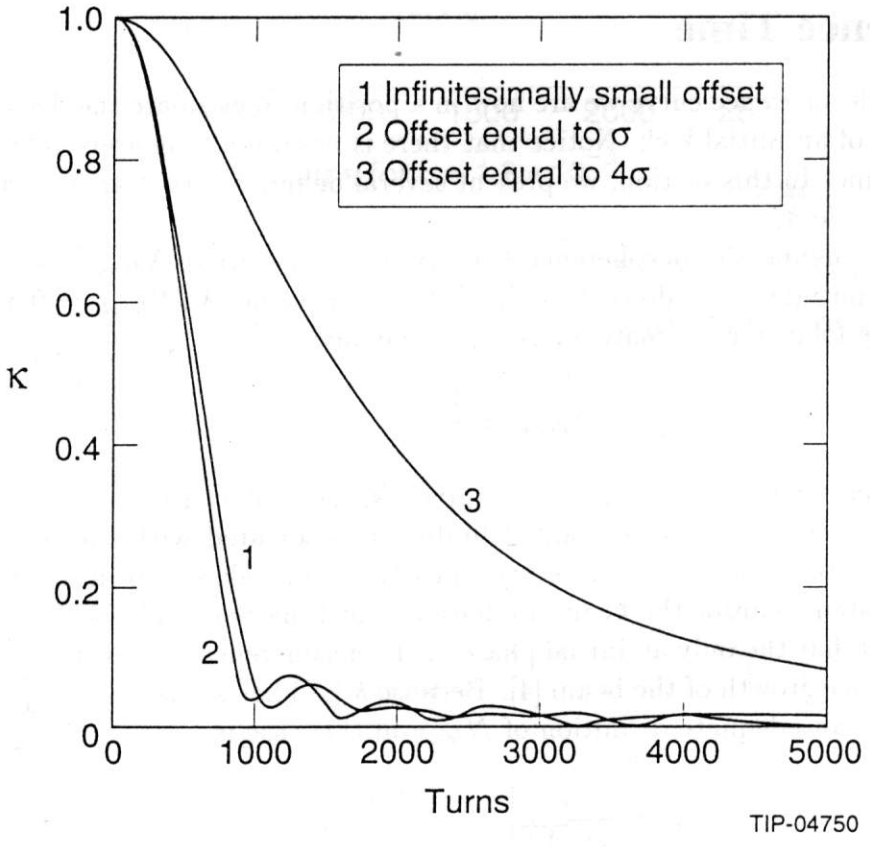

Figure 3. Decoherence curves for various initial offsets.

This gives us the relation,

$$N_{decoh} = 2\sum_{m=1}^{N} K^2(m) \approx \int_0^{\infty} \mathcal{K}^2(m)dm. \tag{19}$$

In Eq. (19) we have considered that $\mathcal{K}(m)$ is rapidly oscillating (with the betatron frequency) function, so that the average its square is equal to half of its amplitude squared. Our calculations give

$$N_{decoh} = \frac{0.81}{\xi}, \tag{20}$$

with $N_{decoh} = 450$ for the SSC. Our computer tracking confirmed Eqs. (18) and (19) within an accuracy of the statistics of the calculations.

6. Summary

In this paper, we have calculated the decoherence function for the head-on beam-beam collisions. This function gives the most complete description of the process, allowing, for example, calculation of the tune spread associated with the beam-beam interaction (see Eq.(11)). Via the Fourier transform, it is directly related to the distribution of the particles over the tune shift $\Delta\nu_x$. What is more important, this function gives us a natural characteristic time scale on which an initially driven betatron oscillation damps out. We have shown that, depending on the exact definition, the expression for N_{decoh} has a form, N_{decoh} =const/ξ, where ξ is the beam-beam tune shift and const$\approx$ 1. Our result generally agrees with the numerical study of the SSC beam decoherence [8].

7. Acknowledgment

The authors are thankful to E.Tsyganov, whose critical remarks initiated this work.

References

[1] R.E. Meller, et. al, "Decoherence of Kicked Beams" , SSC-N-360, 1987.

[2] V.A. Lebedev, V.V. Parkhomchuk, V.D. Shiltsev and A.N. Skrinsky, "Suppression of Emittance Growth Caused by Mechanical Vibrations of Magnetic Measurements in Presence of Beam-Beam Effects in the SSC", Preprint INP 91-120, Novosibirsk, 1991.

[3] W. Chou and J.O. Peterson, "The SSC Transverse Feedback System", SSCL-623, 1993.

[4] V.A. Lebedev, V.V. Parkhomchuk, V.D. Shiltsev and G.V. Stupakov, "Emittance Growth due to Noise and its Suppression with the Feedback System in Large Hadron Colliders", SSCL-Preprint-188, March 1993; and *Particle Accelerators*, vol.44, No. 3-4, pp. 147-164 (1994).

[5] V.V. Parkhomchuk and V.D. Shiltsev, "Is Transverse Feedback Necessary for the SSC Emittance Preservation? (Vibration Noise Analysis and Feedback Parameters Optimization)", SSCL-622, June 1993.

[6] G. Lopez, "Head-On and Long Range Beam-Beam Tune Shifts Spread in the SSC", SSCL-422, 1991.

[7] A. Chao and G.V. Stupakov, "Collective Effects and Beam Decoherence", SSCL-621, April 1993.

[8] E. Tsyganov et. al, "Decoherence of the SSC Beam Oscillation due to Head-On Beam-Beam Collisions", SSCL-Preprint-481, 1993.

COUPLING CORRECTION FOR THE BEAM-BEAM EFFECTS OPTIMIZATION*

D.V. Parkhomchuk

Budker Institute of Nuclear Physics, Novosibirsk, 630090, Russia

e-mail: D.V.Parkhomchuk@inp.nsk.su

1. Introduction

It is the well-known fact that beam-beam effects on the flat beams increase mainly vertical size of the beams. In the absents of beam-beam effects vertical size is generated by betatron coupling, and the horizontal size by quantum excitations. So while the horizontal beam size is defined by magnetic structure and RF acceleration parameters, we have a plenty of methods of placing skew-quadrupoles to generate the same initial vertical beam size. The question is what configuration of coupling should we choose (or avoid) to optimize beam-beam effects.

2. Simulation technique

It's clear that one cannot solve this problem analytically, so the simulation program was written. The program makes the tracking through linearized accelerator structure (VEPP-4M was taken) with variously placed skew-quadrupoles and one interaction point, where beam-beam kick was calculated by complex function Erf, assuming that the beam is short (thus kick doesn't depend on longitudinal motion). Longitudinal motion and beam profile tilt angle were taken into account. Quantum excitation is defined as a random horizontal kick for turn, that produce the calculated horizontal beam size. The excitation of the vertical beam size occurs in skew-quadrupoles.

3. Checkings

The comparison with analytical estimates [1] of vertical beam size was made, to ensure that simulation mechanism is adequate.

$$\begin{bmatrix} \dfrac{<x_\beta^2>}{\beta_x} \\ \dfrac{<x_\beta y_\beta>}{\sqrt{\beta_x\beta_y}} \\ \dfrac{<y_\beta^2>}{\beta_y} \end{bmatrix} = D \begin{bmatrix} \alpha_y \Delta\nu^2 + (\alpha_x+\alpha_y)|Q|^2 & 2\alpha_y Q_1 \Delta\nu & (\alpha_x+\alpha_y)|Q|^2 \\ \alpha_y Q_1 \Delta\nu & 2(\alpha_x+\alpha_y)Q_1^2 & -\alpha_x Q_1 \Delta\nu \\ (\alpha_x+\alpha_y)|Q|^2 & -2\alpha_x Q_1 \Delta\nu & \alpha_x \Delta\nu^2 + (\alpha_x+\alpha_y)|Q|^2 \end{bmatrix} \begin{bmatrix} H_{xx} \\ H_{xy} \\ H_{yy} \end{bmatrix}$$

$$\Delta\nu = \nu_x - \nu_y - m$$

* Work supported by the National Science Foundation under contract NKQ000 №51954

Where:

$$Q = Q_1 + iQ_2 =$$

$$= \int_{\theta_r}^{\theta_r+2\pi} d\theta \left\{ \exp\left[i \int_{\theta_r}^{\theta} d\theta \left(\frac{R}{\beta_x} - \frac{R}{\beta_y} - \Delta\nu \right) \right] \right\} \frac{\sqrt{\beta_x \beta_y}}{4\pi R} \left[S_Q - \frac{S_M R}{4} \left(\frac{\beta'_x}{\beta_x} - \frac{\beta'_y}{\beta_y} \right) - \frac{i}{2} S_M R \left(\frac{1}{\beta_x} - \frac{1}{\beta_y} \right) \right]$$

$$H_{ij} = C_L \frac{\gamma^5}{2\pi R} \oint \frac{ds}{|\rho|^3 \sqrt{\beta_i \beta_j}} \left[\eta_i \eta_j + \left(\beta_i \eta'_i - \frac{1}{2} \beta'_i \eta_i \right) \left(\beta_j \eta'_j - \frac{1}{2} \beta'_j \eta_j \right) \right]$$

with i,j = x,y; β_i, the betatron function; R, the average machine radius; ρ, the radius of curvative in a bending magnet; γ, the beam energy in units of rest energy; and $C_L = 55 r_e \hbar / 48\sqrt{3} m_e = 2.16 \cdot 10^{-19} m^3 / s$. $S_Q(\theta) = (\partial B_x / \partial x) R^2 / B\rho$ and $S_M(\theta) = B_z R / B\rho$, strength of skew quadrupole and solenoid fields; $B\rho$, the particle rigidity.

In this terms a skew-quadrupole generate a certain Q. So having a basis of a pair of skews we can suppress any coupling by making Q=0. The example of such compensation is given in the picture.

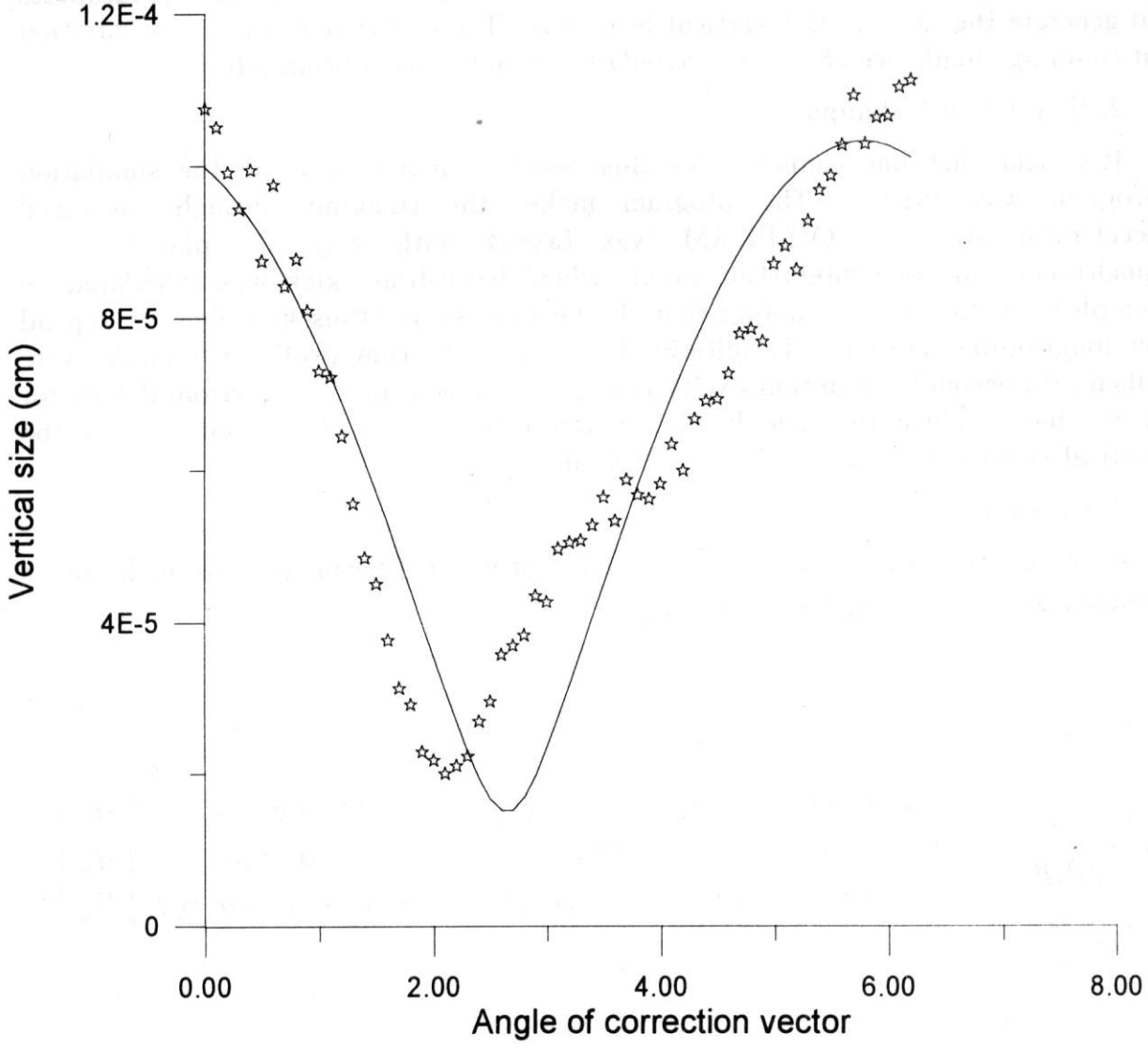

On the picture is shown the behavior of vertical beam size when there is the coupling error in the ring, and we rotate the correction vector Q with the same modules as error by the pair of skews. In one point we see the compensation, there correction vector is opposite to error vector.

So we can partly compensate the random coupling error or coupling caused by detector's solenoids by pair of skew. The picture shows rather well agreement tracking with analytical formulas for vertical size in coupled lattice without beam-beam effects.

4. Results

The different skew placement at different working point was treated to find out the "bad" and "good" type of coupling. It was not find out any preferable coupling configuration, when the coupling produced by each coupling element is less than total coupling ('no compensation' case). But when there is the compensation (the total coupling is less than the coupling of some elements) one can notice the difference. Let us look at the graphs:

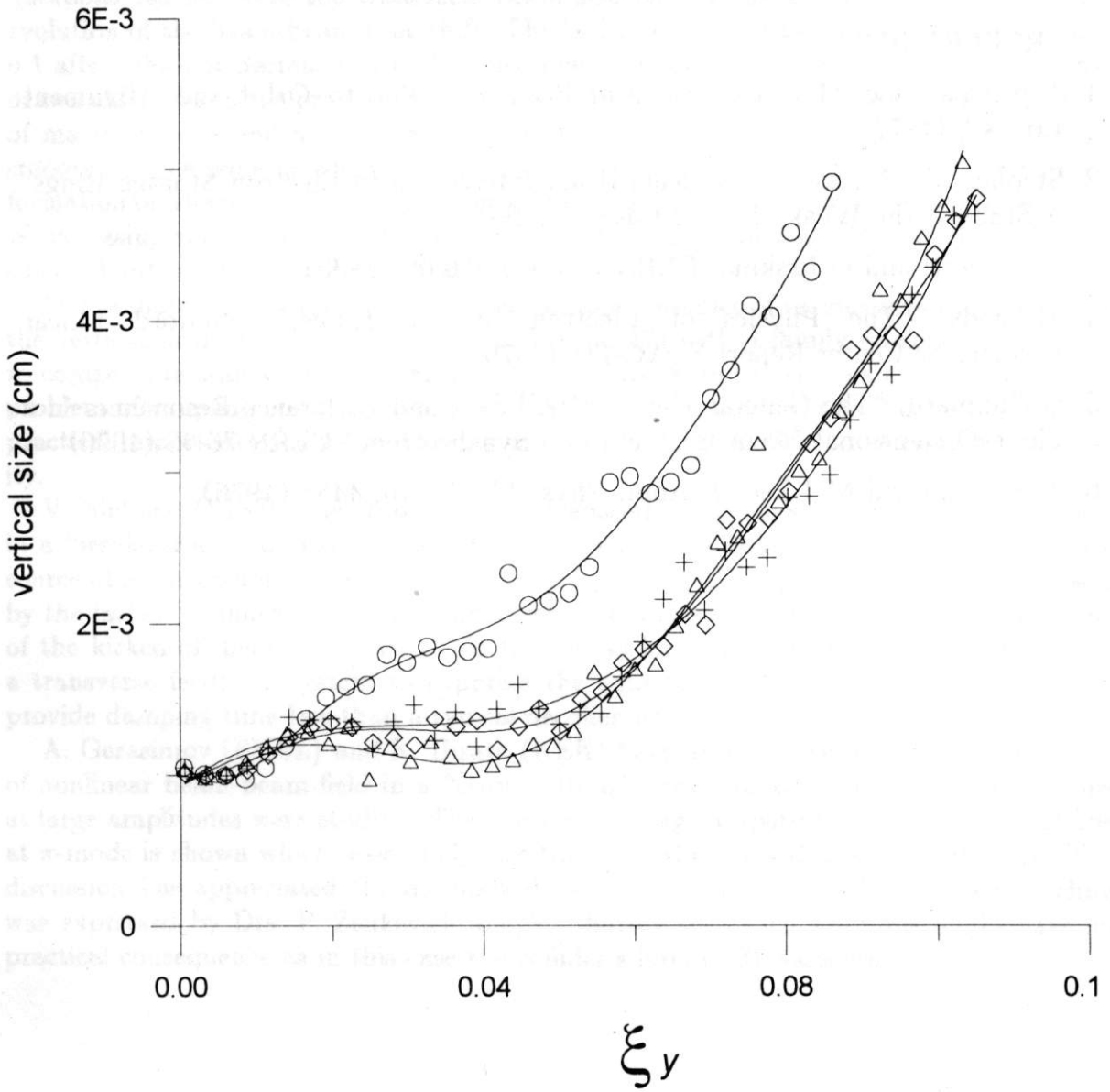

Here we can see the dependence of the vertical beam size on the strength of beam-beam effects with different coupling configuration. Three of them are slightly different, but the fourth is extremely bad - the vertical size blow up at relatively low linear tune shift. As I mentioned above it is a case of 'coupling compensation'. Presently such a situation takes place on VEPP4-M, and to improve it, the localization of coupling errors is investigated now.

5. Conclusion

So one can extract the useful advice from here. It's obvious that beam-beam effects cause the shifts of coupling vectors of elements. So if one makes the compensation by elements whose coupling is more than final coupling, the shifts of them produce large shift of final coupling and compensation is destroyed.

If there are coupling errors or solenoids, coupling must be corrected by skews or solenoids which are close to the place of error and have the collinear (opposite) to the error coupling vectors, because in that case the shifts of those vectors don't produce large shift of total vector.

REFERENCES

1. A.W.Chao and M.J.Lee, "Vertical Beam Size due to Orbit and Alignment Errors," (1977).
2. Stephen Val Milton, "The Beam-Beam Interaction in Electron Storage Rings: A Study if the Weak/Strong Case," (1990).
3. M.Bassetti and G.Erskine. CERN ISR-TH/80-06 (1980).
4. M.Sands, "The Physics of Electron Storage Rings," Stanford Linear Accelerator Center Report SLAC-121 (1970).
5. G.Guignard, "The General Theory of All Sum and Difference Resonances in a Three-Dimensional Magnetic Field in a Synchrotron," CERN 76-06 (1976)
6. A.W.Chao and M.J.Lee, J. Appl. Phys. 47, No. 10, 4453 (1976).

The program of the beam-beam effects study on the VEPP-4M

G.M.Tumaikin

Budker Institute of Nuclear Physics (BINP),
630090, Novosibirsk, Russia, e-mail: tumaikin@inp.nsk.su

The program of the beam-beam effects study on the collider VEPP-4M, that was put into operation after reconstruction, is discussed. There are two motives for this work: first, the increasing of the VEPP-4M luminosity and, second, getting the necessary experience for the φ-, $c-\tau$- and b-factories future projects.

INTRODUCTION

The study of the beam-beam effects in BINP was begun about 30 years ago on electron beams collider VEP-1, when for the first time the influence of nonlinear resonances on beam size and lifetime was investigated. Then experiments were continued on electron-positron colliders VEPP-2, VEPP-2M and VEPP-4 in Novosibirsk, as well as in facilities of other physical centers: ACO (ORCE), Adone (Frackati), SPEAR (Standford), DORIS (Hamburg) etc. The review of results of these experiments was submitted in series of papers[1].

Simultaneously with experimental researches for expired 30 years the large work on theoretical study of beam-beam effects is conducted. Two approaches are here allocated: analytical, based on Hamiltonian formalism, and computer simulation. In the few last years the computer simulation was more successful.

Nevertheless, the wide circle of problems for experimental and theoretical study is marked. The decision of these problems is necessary as for increasing of luminosity on existent collider generation, as for building of the future one.

The program of work on the VEPP-4M discussed below has by purpose the study of small part of unsolved problems.

1. DESCRIPTION OF THE VEPP-4M

The VEPP-4 accelerator facility includes the injection facilities and the collider VEPP-4M. The collider after stoppage in 1985 was considerably modernized[2]. First, the optics of the experimental insertion was considerably changed for the conducting of the experiments on two-photon physics, that permits now to measure energy of scattered electrons (positrons) in process $e^+e^- \to e^+e^- + X$ with high accuracy. Second, the β-function in collision point is reduced, and the multibunch mode with orbit separation in parasitic crossings (PC's) is arranged to increase the luminosity. In the interaction point (IP) the new detector KEDR is placed, enabling carry out the wide program on b-meson physics and two-photon physics.

The main parameters of the VEPP-4M are represented below.

Energy, GeV	6
Circumference, m	366
Bending radius, m	45.5
Betatron frequencies Q_x, Q_z	8.53, 7.57
Compaction factor	0.017
Horizontal emittance, mm * mrad	0.3
Vertical emittance, mm * mrad	0.001
Energy spread, %	0.1
SR loss, MV/turn	4
Synchrotron oscillation damping time, msec	2
Harmonic number	222
Bunch length, cm	4
Space charge parameters ξ_x, ξ_z	0.005, 0.05
Number of particles per bunch	$2 * 10^{11}$
Number of bunches per beam	2
Beam current, mA	50
Luminosity	$7 * 10^{31}$

The interaction point

A number of collision points	1
Vertical β-function, cm	5
Horizontal β-function, cm	70
Dispersion function, cm	80

The parasitic crossings

Type of separation - vertical electrostatic bump.

A number of crossings	3
Vertical β-function, cm	1200, 290
Horizontal β-function, cm	460, 1400
Dispersion function, cm	78,-125

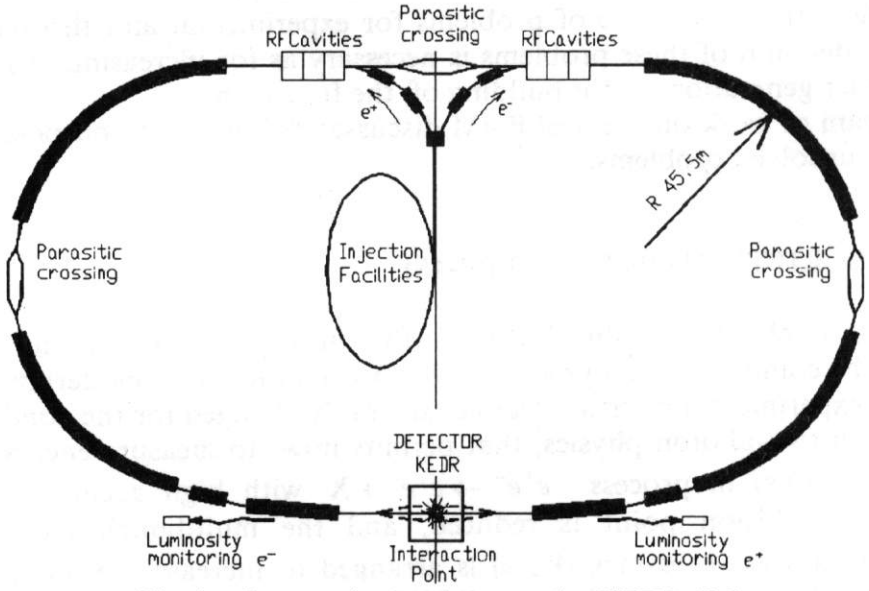

Fig.1. Interaction points on the VEPP-4M.

2. PROGRAM OF EXPERIMENTS

It is assumed to do the work in following directions which are briefly stated below.

2.1. COUPLING OPTIMIZATION FOR THE ACHIEVEMENT OF THE UTMOST SIGNIFICANCE OF SPACE CHARGE PARAMETERS ξ

Usually in electron-positron colliders in the IP's the following equations are valid:

$\sigma_x^* >> \sigma_z^*$, $\xi_z >> \xi_x$, where * denotes "in the IP".

Hence, beam-beam effects mainly increase the vertical beam size, that conducts to reduction of the luminosity and the lifetime.

It is known, that the initial vertical beam size at small currents is basically defined by the magnetic field distortion. It is possible to allocate the following main causes of excitation of initial beam size:

- quantum fluctuations of synchrotron radiation in locations with large vertical dispersion function,
- coupling resonances $n\nu_z \pm m\nu_x = k$,
- vertical dispersion in collision point,
- vertical distortion of the orbit with presence of the chromaticity.

It is expected, that the displacement of these elements concerning IP strongly influences the dynamics of counter beams even in the case of the same initial vertical beam size.

Thus, the goal is to find such a way of achieving initial vertical size at which the beam-beam effects will be minimal. To resolve this problem it is necessary to reduce the coupling, and then to find the optimum parameters of skew-quadrupoles.

2.2. INFLUENCE OF LARGE RADIAL DISPERSION

The other goal is the study of the beam-beam effects in the mode with a large dispersion function in the IP. It is important to understand which value of ξ can be obtained and how the beams will behave in the case where the betatron horizontal beam size is substantially less than the synchrotron one.

This study is necessary for the projects of the b- and $c-\tau$- factories with monochromatization of the interaction energy, where the particles are distributed by energy over the interaction region. The modern optics of VEPP-4M allows us to change the betatron-synchrotron size ratio at the IP within wide limits.

2.3. PARASITIC CROSSINGS

The third goal is the study of the PC's influence and determination of the optimal orbit separation. This task is connected with the arranging of the multibunch mode in the VEPP-4M. It is known, at present time the arranging of the multibunch mode is the main method of increasing the luminosity in existing and future colliders.

3. RESEARCH DESIGN AND METHODS

3.1. SIMULATION

The program of research work comprises three problems. They are the investigation of the beam-beam effects in the high dispersion function mode and the study of coupling and PC's influence.

All problems will be solved by numerical simulation which in the first place includes the calculation of the beam size, luminosity, and the lifetime. The simulation will be mainly performed in the weak-strong model. To fulfill this research work, we have a series of programs used earlier. We are going to use the fast tracking technique emerged from a concept proposed earlier by J.Irwin[3]. It has been developed later by D.Shatilov[4,5] for calculation of the lifetime and for beam halo determination. This technique allows us to reduce the required CPU time by several orders of magnitude against the brute-force technique.

The conditions of the problems require new programs, in particular, to study the strong-strong beam regime. The program for study of influence of various methods of vertical beam size generation on beam-beam effects in the weak-strong model is prepared. The first results show that the beam-beam effects dynamics depends on the method of generation of initial size[6]. The program for study of coherent interaction of counter bunches (strong-strong model) in view of PC's influence[7] is developing.

3.2. EXPERIMENT

The appropriate techniques and apparatus have been developed. They comprise:

a) luminosity monitoring by single and double bremsstrahlung and by the small angles scattering;
b) beam size measurement by synchrotron radiation;
c) equilibrium orbit measurement;
d) measurement of optic parameters (β-function and ψ-function);
e) automatic measurement of betatron oscillation frequency;
f) dynamic aperture measurement.

ACKNOWLEDGEMENTS

The author thanks all participants of executed program, especially D.Shatilov, E.Simonov, D.Parkhomchuk and S.Karnaev.

The author expresses a deep gratitude to Soros Fund for support of this work (Grant number NQKOOO).

REFERENCES

1. G.M.Tumaikin, A.B.Temnykh *Beam-beam Interaction and Luminosity Limit in Storage Rings* Proc. of the XIII Int. Conf. on High Energy Accelerators, Novosibirsk, 1986, v.2, p.88
2. I.Ya.Protopopov *Electron-Positron Colliding Beams in Novosibirsk. Status and Projects* Proc. of the XIII Int. Conf. on High Energy Accelerators, Novosibirsk, 1986, v.1, p. 63 (in Russian)
3. J.Irwin *Simulation of Tail Distributions in Electron-Positron Circular Colliders* Third Adv. ICFA Beam Dynamics Workshop, Novosibirsk, 29 May - 3 June, 1989
4. D.N.Shatilov *Beam-beam Simulations at Large Amplitudes and Lifetime Determination* INP 92-79, Novosibirsk, 1992
5. D.N.Shatilov, these proceedings
6. D.V.Parkhomchuk, these proceedings
7. E.A.Simonov, these proceedings

Invariants for Nonlinear Accelerator Optics and Round Colliding Beams

V.V. Danilov and E.A. Perevedentsev
Institute of Nuclear Physics, 630090, Novosibirsk, Russia
E-mail: danilov@inp.nsk.su

Abstract

A model accelerator lattice composed of cells each consisting of a thin nonlinear lens and a drift space is studied. The corresponding one-dimensional nonlinear map of the "accelerator" type is proved to have an exact invariant, provided that the nonlinear kick function(s) are of a special form.

The proposed 1- and 2-cell lattices have invariants expressed as polynomials up to the sixth order in momentum. The results obtained for one-dimensional motion are partially carried over to the two-dimensional case, particularly, to the systems preserving angular momentum. Among those the round colliding beams are considered.

An example of elimination of chaotic trajectories in the motion by adding one lens is presented supporting interest in using integrable systems for improving the dynamic aperture and raising the threshold of the beam blow-up due to the beam-beam effects.

1. Introduction

Recent studies in mathematical physics show a growing interest in integrable systems. In accelerator physics, an integrable system means a one-turn map with the necessary number of commuting and independent integrals of motion. If the manifold of particle motion in the phase space is closed (the motion is finite), we can describe this motion in terms of invariant Liouville tori.

This integrable system is an analogue of a linear system, but its frequencies depend on the values of the integrals of motion. No chaotic trajectories will appear in this map.

It was shown in paper [1], that an accelerator lattice composed of cells consisting of thin nonlinear lenses and drift spaces can have a map with simple (polynomial) integrals.

This paper contains all the results of [1] re-derived by means of a new approach, and furthermore new one-dimensional integrable systems are obtained. Using this approach, we can "cure" certain nonlinear maps from chaos. In other words, we can modify certain nonlinear maps by adding one lens of the special form (which depends on the initial map), such that the stochastic trajectories disappear. The new map is still nonlinear, but integrable. As an example, the Hénon map is "cured" from chaos. This new approach gives a possibility of obtaining integrable systems even for the beam-beam effects.

The results are then extended to the two-dimensional case, and a lattice is presented which can be used as a prototype lattice for a real accelerator.

2. Basic Cell Map

In this paper we construct model accelerator lattices consisting of one or two cells with a drift space and a nonlinear lens. In the map considered, we put $p = x'$, where x' is the particle trajectory slope, and take the drift length $l = 1$ to simplify formulas. The map corresponding to one cell is:

$$\begin{aligned} \overline{x} &= x + p, \\ \overline{p} &= p + f(\overline{x}). \end{aligned} \tag{1}$$

Here x, p are the initial values and $\overline{x}$, $\overline{p}$ are the final values of the coordinate and momentum. $f(\overline{x})$ is the kick function of the nonlinear lens to be found jointly with the desired invariant.

The equation for an invariant I is:

$$I(x,p) \equiv I(x+p, p+f(x+p)) \,. \tag{2}$$

It is more or less evident that it is too difficult (or impossible) to find a general solution of this functional equation, so we have to look for invariants with simple dependence on the coordinate and momentum (see, for example [2, 3]).

Let us fix some general properties of an invariant of 1-cell map (assuming that it exists). For this purpose it is convenient to use the variables $x, \overline{x} \equiv x + p$ instead of x, p ($\overline{x}$ means the coordinate at the end of drift space).

The first remarkable property of an invariant of one cell is that **it is a symmetrical function** of x and $\overline{x}$ *i.e.* it does not change when permuting x and $\overline{x}$. Let us prove this.

At the beginning of the drift space we have the coordinate x while $\overline{x}$ is the coordinate at the end of it. If we start the motion from the end of the drift space in backward direction (with the reversed sign of p), we have the same motion (because this transformation is equivalent to reversal of time) with the initial coordinate $\overline{x}$ and the final one $x \equiv \overline{x} + (-p)$. This reversed motion starts from the beginning of the drift space (we mean that the end of the drift space is the beginning of it for motion with time reversal), so this reversed motion has the same trajectory in the phase space and the same invariant (but the initial and final coordinates are permuted), hence we get:

$$I(x,\overline{x}) \equiv I(\overline{x},x) \,. \tag{3}$$

Let us note that this property holds only if we take the beginning (or the center) of the drift space as the initial point for the map. In the linear case this property is related to the symmetry of the optical functions about the center of the drift space in such a cell.

Let us obtain the second important property of this invariant. Directly from definitions of the invariant and variables we have:

$$\begin{aligned} I(x,\overline{x}) = I(x, x+p) = I(\overline{x}, \overline{x}+\overline{p}) \,, \\ I(x,\overline{x}) = I(\overline{x}, x) = I(\overline{x}, \overline{x}-p) \,. \end{aligned} \tag{4}$$

After comparison of the first and second lines in (4) we have:

$$I(\overline{x}, \overline{x}+\overline{p}) = I(\overline{x}, \overline{x}-p) \,, \tag{5}$$

here $\overline{p} = p + f(\overline{x})$ is the momentum after kick.

Thus, we can obtain the invariant behind the lens from the invariant before the lens by changing p to $-\overline{p}$. In other words, **transformation of the invariant on the lens** (adding its kick to the momentum) **is equivalent to sign reversal of the momentum argument** in this invariant.

These two properties are necessary and sufficient for a function I to be an invariant. It means that if we can find a function with these two properties, we have an integrable system automatically, while the kick of the nonlinear lens is no more arbitrary, its coordinate dependence is determined by the second property (5) of our invariant).

The theory just developed will now be illustrated by an example, which is significant in itself.

Note that an arbitrary function quadratic in momentum has the second property (5). Let it be $H(x,p)$:

$$H(x,p) = A(x)p^2 + B(x)p + C(x)\,.$$

For the new $\overline{p} = p + B(x)/A(x)$,

$$H(x,\overline{p}) = A(x)\overline{p}^2 - B(x)\overline{p} + C(x)\,.$$

We can see that this function expressed in the new momentum has the same form but with the opposite sign of the momentum.

Let us make a very important notice: substitution of $p + g(x)$ instead of p (where $g(x)$ is an arbitrary function of the coordinate) does not change the second property (5) of the invariant, but we have to change the kick function of the lens.

So if we have the second property (5) for p, we have the same property for the variable $\overline{x} = p + x$, and the quadratic invariant in p is also quadratic in $\overline{x}$ (it comes from the definition of $\overline{x}$). Finally we come to a very simple conclusion: every function quadratic in $\overline{x}$ and symmetrical in x and $\overline{x}$ yields an invariant.

A general form of this function is:

$$I(x,\overline{x}) = ax^2\overline{x}^2 + bx\overline{x}(x+\overline{x}) + cx\overline{x} + d(x^2+\overline{x}^2) + e(x+\overline{x}), \tag{6}$$

here a, b, c, d, e are arbitrary constants.

Let us obtain the lens kick from I. We have to change x to $\overline{x} - p$ to obtain the invariant at the end of the drift space in the form:

$$I = A(\overline{x})p^2 - B(\overline{x})p + C(\overline{x}).$$

From the second property (5) of our invariant we have:

$$I(\overline{x}, \overline{x} - p) = I(\overline{x}, \overline{x} + \overline{p}), \tag{7}$$

where $\overline{p} = p + f(\overline{x})$ is the momentum after the kick. After substituting $p = \overline{p} - f(\overline{x})$ into the invariant at the end of the drift space and using the previous equation we get:

$$A(\overline{x})(\overline{p} - f(\overline{x}))^2 - B(\overline{x})(\overline{p} - f(\overline{x})) + C(\overline{x}) = A(\overline{x})(\overline{p})^2 + B(\overline{x})\overline{p} + C(\overline{x}). \tag{8}$$

This equation yields:

$$f(\overline{x}) = -B(\overline{x})/A(\overline{x}). \tag{9}$$

So we have got the general rule: if we take the invariant after the lens, the kick of this lens is equal to the certain function whose addition to the momentum is equivalent to the sign reversal of the momentum in the invariant.

In general, the second property (5) holds for all functions of the form:

$$f_0(x) + f_1(x)(p^2 - F(x)p) + f_2(x)(p^2 - F(x)p)^2 + \ldots, \tag{10}$$

here $f_0, f_1, f_2, \ldots$ are arbitrary functions of the coordinate.

Let us introduce a notion which will often be used later: F in (10) will be called a Sign Reversal Function (SRF). We can check the second property of the invariant in (10) by substituting $p + F(x)$ instead of p.

As we noted earlier, if we put p in the form $p = p' + G(x)$, this property remains for p' too, but the new F in (10) now is:

$$F_{new}(x) = F(x) - 2G(x) .$$

For the variable $\overline{x} = p + x$ the Sign Reversal Function $F_{\overline{x}}$ is:

$$F_{\overline{x}} = F(x) + 2x . \tag{11}$$

For the invariant (6) the SRF for $\overline{x}$ is:

$$F_{\overline{x}} = -\frac{bx^2 + cx + e}{ax^2 + bx + d} .$$

So the perfect kick of the lens must be:

$$F(x) = -2x - \frac{bx^2 + cx + e}{ax^2 + bx + d} . \tag{12}$$

The same formulas were obtained in [1] in other way[1].

Now we can present one more system with a new invariant:

$$I(x, \overline{x}) = (ax\overline{x}(\overline{x} - x) + b(x + \overline{x})(\overline{x} - x) + c(\overline{x} - x))^2, \tag{13}$$

here a, b, c are arbitrary constants.

This invariant has the form (10) and it is a symmetrical function of $x, \overline{x}$. The kick of the lens for this case is:

$$F(x) = -2x + \frac{ax^2 - c}{ax + b} . \tag{14}$$

It was shown in [1], that the invariants of the third degree in momentum cannot appear in 1-cell maps. Now one can be assured that polynomial invariants with odd highest powers in momentum do not exist at all. We can note that such functions do not have the second property (5) of one cell invariant, because we can never reverse the sign of the highest odd power of momentum by adding any function of coordinate to the momentum. It proves the above statement about polynomial invariants with an odd highest power in momentum.

Moreover, after investigation of invariants of higher order in momentum, a preliminary conclusion can be drawn: it is doubtful that other invariants with finite order in momentum exist, besides (6) and (13).

[1]Recently we became aware of previous work by E.M. McMillan et al. [4], where the rational nonlinear kick (12) and the symmetric form of the invariant (6) were studied in certain particular cases. We are grateful to B.V. Chirikov for this reference and for the useful discussion.

3. Two-Cell Map

Let us take the function $J(x, \overline{x})$, which has the form (10) for x and $\overline{x}$ (or, in other words, this function has only the second property of the invariant for a 1-cell map for both variables x and $\overline{x}$, and is allowed to be non-symmetrical). The Sign Reversal Functions can be different for x and $\overline{x}$.

Let us transform this function over the two cells. Transformation over the drift space means just simply expressing the new x, p in terms of the old ones. Transformation over the lens again means expressing the new momentum $\overline{p}$ via p, and we require that this transformation be equivalent to replacing p by $-\overline{p}$ (it follows from the definition of the SRF F).

Now we have to use the indices of variables which mean the cell number for example, $\overline{x}_1$ means the coordinate at the end of the first drift space. It is evident that the coordinate at the end of the drift space is equal to the coordinate at the beginning of the next cell ($\overline{x}_0 \equiv x_1$, etc.).

Let us start from the beginning of the first cell and transform J to the beginning of the second one:

$$J(x_0, \overline{x}_0) \equiv J(\overline{x}_0 - p_0, \overline{x}_0) \equiv J(\overline{x}_0 + p_1, \overline{x}_0) \equiv J(\overline{x}_1, x_1) \; . \tag{15}$$

So the transformation of the function J over one cell is equivalent to interchanging of the variables $x, \overline{x}$. If J happens to be a symmetric function of $x, \overline{x}$ then it is an invariant for the map of the first cell alone.

Now we transform it over the second cell in the same way (as we have seen, it means just interchanging the variables):

$$J(\overline{x}_1, x_1) \equiv J(x_2, \overline{x}_2) \equiv J(x_0, \overline{x}_0) \; . \tag{16}$$

The last relation shows that J is an invariant function for the 2-cell map.

Thus, **an arbitrary function of two variables which has the form (10) in both variables generates an integrable map for the 2-cell lattice.**

This transformation over two cells was made in [1] in a direct way for quadratic polynomials in p (for them the property (10) is satisfied automatically). It was found there that the transformation of coefficients of these polynomials is the identity transformation for the 2-cell map. Now it is proved in the general way.

Let us consider an example. From the previous section we know that an arbitrary quadratic function in $\overline{x}$ has the second property of the invariant of 1-cell map. So any function, quadratic in x and $\overline{x}$, generates all the simplest integrable 2-cell maps. The general form of this invariant is:

$$I(x, \overline{x}) = ax^2\overline{x}^2 + bx\overline{x}^2 + cx^2\overline{x} + dx\overline{x} + ex^2 + f\overline{x}^2 + gx + h\overline{x}, \tag{17}$$

here a, b, c, d, e, f, g, h are arbitrary constants.

Taking here the Sign Reversal Function for $\overline{x}$ and subtracting $2x$ (see (10,11)), we obtain the kick of the first lens:

$$f_1(x) = -\frac{cx^2 + dx + h}{ax^2 + bx + f} - 2x \; . \tag{18}$$

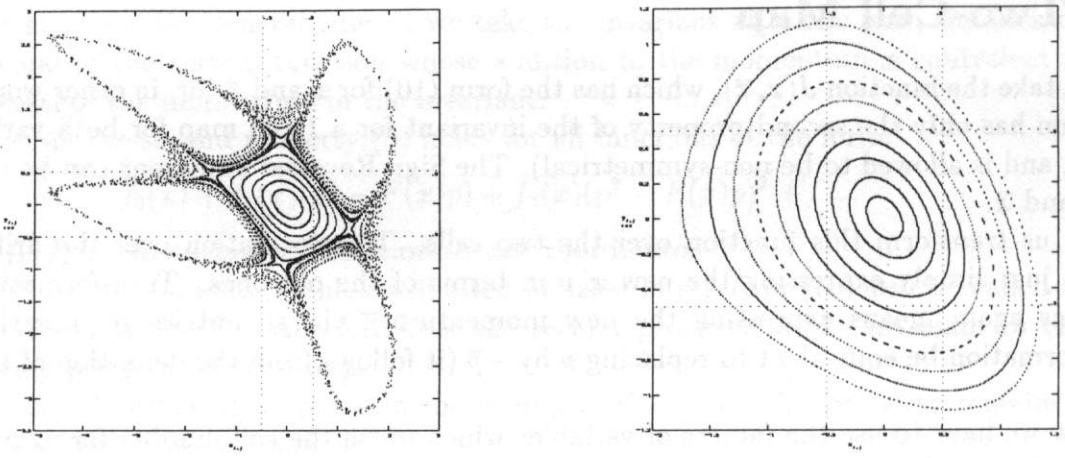

Figure 1. *left*) The Hénon map with $f_1 = -0.15x^2 - 0.6x, \quad f_2 = -0.6x$.
right) The map corrected by (19) with the same f_1 and $f_2 = \frac{-0.3x^2-0.6x}{0.15x+1}$.
For both examples $a, b, h = 0,\ e, f = 1$ in (17).

The same function for the variable x, minus $2x$, gives the second kick:

$$f_2(x) = -\frac{bx^2 + dx + g}{ax^2 + cx + e} - 2x\ . \tag{19}$$

There is an intersting combination of parameters for this case. If we set $a, b, h \equiv 0$, we have a combination of the sextupole and the quadrupole as one of the lenses (namely, the first one). If we put another lens in this 2-cell lattice as the quadrupole, we obtain a particular case of the Hénon map with two identical linear cells and a superimposed sextupole in one of them. We can "cure" this non-integrable map by changing the second lens so that it would take the form (19). In Fig. 1 one can see three phase space portaits: the Hénon map on the top and the integrable one on the bottom left as resulted from this correction. The difference of the second lens for these two cases begins from the second order in the coordinate.

Now let us assume that we have two arbitrary lenses in two cells. Can we make the corresponding map integrable by varying one of the lenses? If we know the solution to such problem, we notice that it is close to the problem of the "beam blow-up" due to the beam-beam effects: we can make the whole map, including the nonlinear kick from the opposite bunch, *integrable* (without elimination or cancellation of nonlinearities).

Some combination of parameters in the map related to the invariant (17) gives an example of elimination of overlapping resonances by means of *small correction* in one of the lenses, so as to bring it to the form (19) (see Fig. 2).

It is easy to obtain a formal series for solving the problem, mentioned above.

Let us consider the 2-cell lattice where one of the two lenses has an arbitrary kick function $f(x)$. The Sign Reversal Function F for the variable $\overline{x} = p + x$ in (10) is equal to $f + 2x$.

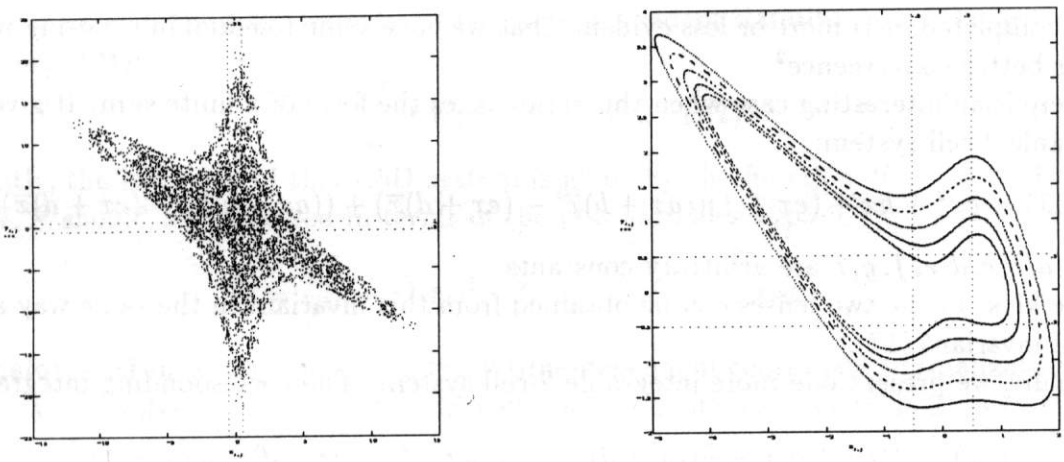

Figure 2. *left*) A globally chaotic map with $f_1 = \frac{-0.8x^3-1.2x^2+0.85x}{0.4x^2+0.77x+1}$ and $f_2 = \frac{-0.8x^3+0.141x^2+0.85x}{0.4x^2-0.34x+1}$.
right) The map corrected by (19) with with the same f_1 and $f_2 = \frac{-0.8x^3-0.09x^2+0.85x}{0.4x^2-0.34x+1}$.

So, for the reasons discussed above, our invariant must have the form (10):

$$I(x,\overline{x}) = f_0(x) + f_1(x)(\overline{x}^2 - F(x)\overline{x}) + f_2(x)(\overline{x}^2 - F(x)\overline{x})^2 + \ldots, \qquad (20)$$

here $f_0, f_1, f_2, \ldots$ are still arbitrary functions of the coordinate.

Let us choose f_i such that the invariant becomes a quadratic function in x in the coefficients of all the powers of $\overline{x}$. The coefficient of zeroth power of $\overline{x}$ is equal to $f_0(x)$, so this function must be quadratic:

$$f_0(x) = qu_0(x).$$

Then, the coefficient of $\overline{x}$ is $-f_1(x)F(x)$, so we put:

$$-f_1(x)F(x) = qu_1(x),$$

here qu_1 is an arbitrary quadratic function. Then from the next step we can find $f_2(x)$:

$$f_1(x) + f_2(x) \cdot F(x)^2 = qu_2(x)\ .$$

Now we can solve for $f_2(x)$ the above relation(s). We can perform this step-by-step operation for all powers of $\overline{x}$ so that from each relation for the i-th power we get f_i.

If this series converges, we have the second property of the invariant for x automatically, because it is constructed as a quadratic function. The analysis of convergence of this series

is not completed, it is more or less evident, that we have some freedom in choosing functions qu_i for better convergence[2].

There is an interesting case when this series takes the form of a finite sum. It gives a new integrable 2-cell system:

$$I(x,\overline{x}) = gx^2 + hx + (ex+f)((ax+b)\overline{x}^2 - (cx+d)\overline{x}) + ((ax+b)\overline{x}^2 - (cx+d)\overline{x})^2, \quad (21)$$

where a, b, c, d, e, f, g, h are arbitrary constants.

The kicks of the two lenses can be obtained from this invariant in the same way as in the case of invariant (17).

Finally, we present one more integrable 2-cell system. The corresponding integral is:

$$I(x,\overline{x}) = [((ax+b)\overline{x} - \frac{1}{2}(cx+d)) \cdot ((ax+b)\overline{x}^2 - (cx+d)\overline{x} + ex + f)]^2\,, \quad (22)$$

here a, b, c, d, e, f are arbitrary constants. The squared expression is a quadratic function in x, so $I(x,\overline{x})$ has the second property for x automatically. One can check, that the Sign Reversal Function for $\overline{x}$ is:

$$F(x) = \frac{ax+b}{cx+d}\,.$$

So, expression (22) gives the invariant of one more family of integrable 2-cell systems.

4. Invariants Quadratic in Momentum

Previous sections dealt with the systems where the time dependence was represented by delta-functional non-linear kick functions, and the invariants were quadratic in momentum only at the kick moment. Here we construct a family of continuous time-dependent 1D Hamiltonians which have a quadratic invariant, and thus the respective motion in 1.5D is integrable. Starting from a Hamiltonian which is independent of the time variable T (with the particle mass $m = 1$):

$$H(X,P) = \frac{P^2}{2} + U(X)\,, \quad (23)$$

we can apply a time-dependent (canonical) transformation of the dynamic variables along with a relevant transformation of the time variable $T(t)$: $X(T), P(T) \xrightarrow{T(t)} x(t), p(t)$, so that the Hamiltonian will take the form:

$$\mathcal{H}(x,p,t) = \frac{p^2}{2} + \mathcal{U}(x,t)\,. \quad (24)$$

Transformation 1° is additive, use is made of any (differentiable) coordinate displacement function of time $D(t)$:

$$\begin{aligned} t &= T\,, \\ x &= X + D(t)\,, \\ p &= P + \dot{D}(t)\,, \end{aligned} \quad (25)$$

[2]There is a great difference between the algebraic approach presented here and the algorithm by J.R. Cary et al. [5] for iterative elimination of resonance islands by introducing nonlinear corrections into a known map of one period. Convergence of this procedure is also problematic.

here 'dot' stands for the time derivative. The time-dependent Hamiltonian of the new system has the form (24):

$$\mathcal{H} = \frac{p^2}{2} + U(x - D(t)) - x \cdot \ddot{D}(t)\,. \tag{26}$$

Apparently, the invariant of this 1.5D system is given by the function $H(X,P)$ of Eq. (23) where X, P should be expressed in terms of the new variables x, p:

$$H = \frac{1}{2}(p - \dot{D}(t))^2 + U(x - D(t)) = const\,. \tag{27}$$

Transformation 2° applies an arbitrary time-dependent coordinate normalization function $A(t)$ and involves a corresponding transformation of the time variable $T \to t$:

$$\begin{aligned} dt &= A^2 dT\,, \\ x &= AX\,, \\ p &= A\dot{X} + \dot{A}X = \frac{P}{A} + \dot{A}X\,, \end{aligned} \tag{28}$$

where 'dot' denotes differentiation with respect to the new time t and use is made of the Hamiltonian equation $dX/dT = P$ in the last line. By its definition, $p = \dot{x}$, while the second Hamiltonian equation:

$$\dot{p} = \frac{\dot{P}}{A} - P\frac{\dot{A}}{A^2} + \dot{A}\dot{X} + \ddot{A}X = -\frac{U'}{A^3} + \ddot{A}X$$

yields the desired time-dependent Hamiltonian function:

$$\mathcal{H} = \frac{p^2}{2} + \frac{1}{A^2}U(\frac{x}{A}) - \frac{\ddot{A}}{A} \cdot \frac{x^2}{2}\,. \tag{29}$$

Again the invariant of this 1.5D integrable system is available from (23): using (28) we express X, P via x, p and obtain:

$$H = \frac{1}{2}(Ap - \dot{A}x)^2 + U(\frac{x}{A}) = const\,. \tag{30}$$

This expression is a generalization of the Courant-Snyder invariant of the linear systems[3].

Any combination of transformations 1° and 2° also provides an integrable system of the form (24), we present in Appendix an expression of the invariant combined from (27) and (30). Note that any integrable system produced with this technique involves three arbitrary functions: $U(X), D(t)$ and $A(t)$. One can prove directly that they form a complete set of freedoms for a 1.5D integrable system with the invariant quadratic in momentum, see Appendix.

Transformation 2° will be applied in the following section to the 2D systems preserving angular momentum, in particular to the problem of round colliding beams.

[3]Indeed, Hill's equation $\ddot{x} + g(t)x = 0$ implies $U = g(t)x^2/2$ in (24). Taking $U(X) = X^2/2$ in (23) we immediately obtain from (29): $\ddot{A} + g(t)A = A^{-3}$, *i.e.* the well-known equation for the betatron amplitude function, hence $A(t) = \sqrt{\beta}$, and (30) takes the usual form of the Courant-Snyder invariant. We see that x, p correspond to the conventional betatron variables, t is the machine azimuth, while X, P are the normalized betatron variables and T stands for the betatron phase advance.

5. 2D Systems with Conservation of Angular Momentum

It is generally known that two-dimensional motion in the central force has an additional integral in the form of angular momentum $M = x\,p_y - y\,p_x$, and thus is reducible to the 1D problem in the polar coordinates. The equivalent 1D Hamiltonian can be expressed in terms of $r = \sqrt{x^2 + y^2}$, $p_r = \dot{r}$ with addition of the fictitious 'centrifugal' potential $U_{cf} = M^2/2r^2$:

$$\mathcal{H} = \frac{p_r^2}{2} + \mathcal{U}(r,t) + \frac{M^2}{2r^2} \tag{31}$$

Aiming at integrable two-dimensional systems of physical interest we need an invariant which exists for any value of M, *i.e.* for all particles with different angular momenta. In particular, our system must be integrable at $M = 0$.

Let us carry the results of Section 2 over 2D systems preserving angular momentum. The mapping consisting of the drift space and any kick force in the form (12) corresponds to the integrable 1D motion and fits to the case $M = 0$. However, integrable 2D systems with any $M \neq 0$ can be sought as a subset of these 1D systems, namely the two-dimensional kick (12) must be radial in order to preserve angular momentum. If we now interprete (12) as a radial component of a two-dimensional vector, then we can directly check that among all the rational forms (12), those with $b = e = 0$ correspond to integrable motion with $M \neq 0$, hence:

$$f_r = -2r - \frac{cr}{ar^2 + d}\,. \tag{32}$$

So the 1D case is partially extended to the 2D motion with axial symmetry. The obtained force (32) is interesting for the round colliding beams problem in that it corresponds to the kick from infinitely short opposing bunch in both limiting cases $r \to 0$ and $r \to \infty$.

Turning back to the continuous Hamiltonian systems, we seek possible extensions of the integrable 1D systems to the 2D systems with conservation of angular momentum. We can write an analogue of the time-dependent Hamiltonian (29) of the integrable 1D motion for these effectively one-dimensional systems in terms of r, p_r, M, ϕ:

$$\mathcal{H} = \frac{p_r^2}{2} + \frac{1}{A^2} U_{eff}\left(\frac{r}{A}\right) - \frac{\ddot{A}}{A} \cdot \frac{r^2}{2} \tag{33}$$

with $U_{eff} = U + U_{cf} = U + \dfrac{M^2}{2r^2}$.

Note the remarcable property of the centrifugal potential U_{cf}: being proportional to r^{-2}, it keeps its form irrespectively of the normalization transformation $R = r/A$ with any function A at any value of angular momentum M!

Thus we conclude that all the 1D formalism in Section 4 is immediately applicable to the 2D systems preserving angular momentum; the only modification is in addition of U_{cf} to $U(R)$, but this has no effect on the decision whether a system in question is or is not integrable, namely, whether its Hamiltonian has the form (33).

6. Round Colliding Beams

Consider the particle motion in the fields of opposing bunch[4] with the Gaussian density distribution in all the three dimensions, $\sigma_{x,y} = \sqrt{\beta_{x,y}\epsilon_{x,y}}$, σ_l are the transverse and longitudinal r.m.s. bunch sizes, respectively. The concept of Round Colliding Beams [6] envisages equal β-functions $\beta_x = \beta_y = \beta$ and equal emittances $\epsilon_x = \epsilon_y = \epsilon$ in both degrees of freedom. Let us show how the appropriate arrangement of the machine optics may bring this problem closer to integrability.

The radial force F_{rb} from the strong bunch should account for its variable cross-section (due to variable β-function) and for the relative speed of collision which is twice the speed $v \approx c$ of individual motion of the bunch and the test particle[5]:

$$F_{rb} = \frac{M^2}{r^3} - k\,\frac{1-\exp(-\frac{r^2}{2\beta\epsilon})}{\frac{r}{\sqrt{\beta}}}\cdot\frac{\exp[-\frac{(s-2ct)^2}{2\sigma_l^2}]}{\sqrt{\beta}} - g(t)r\,, \tag{34}$$

here k is proportional to the strong bunch intensity, s is the longitudinal position of the test particle in the weak bunch with respect to its centre, $g(t)$ denotes an (optional) axisymmetric focusing in the Interaction Region (IR). The time $t = 0$ corresponds to the moment when the central test particle ($s = 0$) meets the centre of the strong bunch.

On the other hand, the Hamiltonian of integrable system (33) yields the certain form of the force to be compared with (34):

$$f = \frac{M^2}{r^3} - U'(\frac{r}{A})\frac{1}{A^3} + \frac{\ddot{A}}{A}r \tag{35}$$

Using the free functions A, g we can make these two forms identical for the central particles with $s = 0$. From the radial dependence of F_{rb}, A must be proportional to the optical function in the IR: $A(t) = \sqrt{\beta(t)/\beta_1}$. Then the conventional equation for $\sqrt{\beta}$ yields the equation for A:

$$\ddot{A} + g(t)A = \frac{1}{\beta_1^2 A^3}\,. \tag{36}$$

The longitudinal modulation of F_{rb} can always be packed into the proper definition of the β-function:

$$\beta(t) = \beta_0 \exp(\frac{2t^2}{\sigma_l^2})\,, \tag{37}$$

and the needed focusing $g(t)$ in the IR will result from substitution of $A(t) = \sqrt{\beta(t)/\beta_1}$ into (36). The potential function $U(R)$, $R = r/A$ can be found from:

$$U'(R) = k\,\frac{\beta_0}{\beta_1}\,\frac{1-\exp(-\frac{R^2}{2\beta_1\epsilon})}{R} + \frac{R}{\beta_1^2}\,. \tag{38}$$

[4]We treat here the head-on collision in the weak-strong model, and disregard the synchrotron motion of the test particle and the longitudinal beam-beam effects [7].

[5]To simplify the formalism, we will use scaling of lengths and time units corresponding to $c = 1$.

Thus the exact invariant for this problem is available, and the beam-beam dynamics with round colliding beams in the weak-strong model is reduced to an integrable motion for central test particles ($s = 0$) by means of the appropriate focusing in the interaction region.

The focusing function $g(t)$ is determined by the longitudinal distribution profile in the strong bunch. The longitudinal Gaussian in (34) was inessential in the above consideration[6], we may take any other reasonable longitudinal distribution and adjust to it the form of the β-function imposing the appropriate focusing $g(t)$ in the IR. Specifically, the Lorentz bell $(\tau^2 + t^2)^{-1}$ in the longitudinal profile with $\beta_1 = \beta_0 = \tau$ will result in $g(t) \equiv 0$.

Since the Gaussian longitudinal profile is the most natural, we draw some practical recommendations for this case. Apparently, the case $g(0) = 0$ is attractive, and from (37) we find a relation between the bunch length and the minimum β-value: $\sigma_l = \sqrt{2}\beta_0$. This provides for integrability of motion of the central test particles ($s = 0$). For the off-centre particles the exact invariant is not available, however for $s \leq \sigma_l$ we can expect an "almost integrable" system where the perturbative analysis is possible.

The integrable single-pass system just considered is relevant to linear collider problems. For circular colliders the opposing beam force should be transformed into a periodic function of time with the account of optics in between the repetitive passages through the IR. Although this difference may result in small deviation from integrability (the obtained exact invariant will be lost), the perturbation can always be done practically negligible and the beam-beam dynamics will be almost integrable.

7. 2D Case

It was shown in [1], that we can carry over all the results of 1D case to two dimensional motion by introducing the 2D map in complex variables:

$$\begin{aligned} z_n &= z + p^* , \\ p_n^* &= p^* + F(z_n) , \end{aligned} \tag{39}$$

here $z = x + iy$ and $p = p_x + ip_y$ are composed from the horizontal and vertical coordinates and their respective momenta. The complex kick function $F = f_x - if_y$ is combined from the components f_x, f_y of a potential force corresponding to the symplectic two-dimensional kick. Moreover, F is assumed to be an analytic function of z which corresponds to the (paraxial) Lorentz force from the fields satisfying the Maxwell equations in free space. This case of Laplacian fields is the most interesting in accelerator optics applications.

The transformation between lenses in this map (39) does not correspond to the drift space. From the first line of (39) we have:

$$\begin{aligned} x_n &= x + p_x , \\ y_n &= y - p_y . \end{aligned} \tag{40}$$

Of course, we can construct this transformation by means of linear optics.

We have to substitute z instead of x and p^* instead of p in the 1-cell invariants of 1D case and we obtain two invariants of the 2D case, namely, the real and imaginary parts of the complex invariant.

[6]Note that the Gaussian profile in the transverse distribution *was* essential.

Let us prove that the real and imaginary parts $I_1 = \mathrm{Re}I$, $I_2 = \mathrm{Im}I$ of the complex invariant $I(z, p^*)$ are functionally independent and have a vanishing commutator.

Then for the function $I(z, p^*)$ which is analytic with respect to its both complex variables the Cauchy-Riemann conditions[7]

$$\frac{\partial I_1}{\partial x} = \frac{\partial I_2}{\partial y}, \quad \frac{\partial I_1}{\partial y} = -\frac{\partial I_2}{\partial x}, \quad \frac{\partial I_1}{\partial p_x} = -\frac{\partial I_2}{\partial p_y}, \quad \frac{\partial I_1}{\partial p_y} = \frac{\partial I_2}{\partial p_x} \tag{41}$$

yield the relation between the gradients of I_1 and I_2:

$$\nabla I_1 = \left(\frac{\partial I_1}{\partial x}, \frac{\partial I_1}{\partial p_x}, \frac{\partial I_1}{\partial y}, \frac{\partial I_1}{\partial p_y}\right) = \left(\frac{\partial I_2}{\partial y}, -\frac{\partial I_2}{\partial p_y}, -\frac{\partial I_2}{\partial x}, \frac{\partial I_2}{\partial p_x}\right) = \mathcal{T}\nabla I_2 . \tag{42}$$

The *real* matrix $\mathcal{T}$ in (42):

$$\mathcal{T} = \begin{pmatrix} 0 & 0 & 1 & 0 \\ 0 & 0 & 0 & -1 \\ -1 & 0 & 0 & 0 \\ 0 & 1 & 0 & 0 \end{pmatrix}$$

has only *imaginary* eigenvalues and eigenvectors. If we assume that the two gradient vectors are "parallel": $\nabla I_1 \propto \nabla I_2$, then from relation (42) we see that either of them should be an eigenvector of $\mathcal{T}$. But they are *real* by definition, hence the gradient vectors can never be parallel. Thus we conclude that I_1 and I_2 are independent functions.

Now let us calculate the commutator of I_1, I_2:

$$[I_1, I_2] = \frac{\partial I_1}{\partial p_x}\frac{\partial I_2}{\partial x} - \frac{\partial I_2}{\partial p_x}\frac{\partial I_1}{\partial x} + \frac{\partial I_1}{\partial p_y}\frac{\partial I_2}{\partial y} - \frac{\partial I_2}{\partial p_y}\frac{\partial I_1}{\partial y} . \tag{43}$$

Substitution of (41) into (43) yields: $[I_1, I_2] \equiv 0$, *Q.E.D.*

All maps of the form (39) have an essential fault: at small amplitudes their x- and y-frequencies are on the sum resonance. This fact results from the special form of the linear transformation of coordinate and momentum between lenses (see (40)).

One can use multi-cell lattices with larger number of lenses and with various linear transformations between them. More examples can be found in [8]. Such systems can be taken as a prototype of an "integrable accelerator".

8. Conclusion

The canonical theory can provide a general solution for a map preserving a given invariant (by means of separation of variables in the equation for the generating function of the desired transformation). However it is a problem to find the maps which correspond to the accelerator optics among all those maps.

The main result of the present paper is the construction of feasible 1D maps of the accelerator lattice type having invariants of simple form. Since these solutions can be extended to the 2D case, an implementation of the integrable lattices in practical lattice design is possible

[7]The relations between the partial derivatives w.r.t. the momenta have opposite signs because the complex invariant depends on the complex conjugate variable p^*.

in order to improve the dynamic aperture and, it is hoped, to cure resonance overlapping and global stochasticity. An integrable 2D lattice is constructed in view to give a guideline for designing an "integrable machine" optics.

An important special case of 2D systems with conservation of angular momentum is considered in detail and applied to the beam-beam problem with round colliding beams. This system is shown to be integrable with the appropriate arrangement of linear focusing in the interaction region.

Acknowledgments

We wish to thank J. Gareyte and B. Zotter for their interest in this work, we are grateful to the SL/AP Group at CERN for their hospitality and support during the part of this work.

References

[1] V.V. Danilov and E.A. Perevedentsev, "Integrable Nonlinear Map of the Accelerator Lattice Type", CERN SL/Note 94-21(AP).

[2] E.T. Whittaker, "A treatise on the Analytical Dynamics of Particles and Rigid Bodies", Cambridge, Cambridge University Press (1964).

[3] A. Lichtenberg and M. Lieberman, "Regular and Stochastic Motion", Springer-Verlag, New York (1983).

[4] E.M. McMillan, "Some Thoughts on Stability in Nonlinear Periodic Focusing Systems", Preprint UCRL-17795, Univ. of California, Lawrence Radiation Laboratory, Berkeley, California (1967).
L.J. Laslett, E.M. McMillan and J. Moser, "Long-Term Stability for Particle Orbits", Preprint NYO-1480-101, AEC Computing and Appl. Math. Center, Courant Inst. of Math. Sci., New York Univ., (1968).

[5] C.C. Chow and J.R. Cary, "Integrable Nonlinear Accelerator Lattices", Phys. Rev. Lett., **72**, p. 1196, (1994).

[6] L.M. Barkov et al., "ϕ-factory project in Novosibirsk", *in Proceedings of the 14th Int. Conf. on High Energy Accelerators*, Tsukuba, Japan, 1989, Particle Accelerators, **31**, (1990) 177.
A.N. Filippov et al. "Proposal of the round beam lattice for VEPP-2M collider", *in Proceedings of the 15th Int. Conf. on High Energy Accelerators,* Hamburg, **2** (1992) 1145.

[7] V.V.Danilov et al., "Longitudinal Beam-Beam Effects for an Ultra-High Luminosity Regime", *in Proceedings of the 1991 IEEE Part.Acc.Conf.,* San Francisco, **1** (1991) 526.
V.V.Danilov et al., "Longitudinal Effects in Beam-Beam Interaction for an Ultra-High Luminosity Regime", *in Proceedings of the Workshop on Beam-Beam and Beam-Radiation Interactions,* Los Angeles, May 13-16, 1991. World Scientific, Singapore, 1992.

[8] V.V. Danilov and E.A. Perevedentsev, "On Invariants and Integrability in Nonlinear Accelerator Optics", CERN SL/Note 94-74(AP).

Appendix: General Form of the Invariant Quadratic in Momentum

Consider a general form of invariant quadratic in momentum p, assuming that the coefficients A, B, V are arbitrary functions of time t and coordinate x:

$$I = \frac{1}{2}(Ap - B)^2 + V\,,$$

$A \neq 0$. Equating its total time derivative to zero, we account for the Hamiltonian equations of motion $\dot{x} = p$, $\dot{p} = f$, where the unknown force f depends on t, x

$$\frac{dI}{dt} = (Ap - B)\big(A_x p^2 + (A_t - B_x)p + Af - B_t\big) + V_x p + V_t \equiv 0\,,$$

the subscripts here denote the respective partial derivatives. The vanishing coefficients of each power of p yield a set of equations in partial derivatives for the four unknown functions: f is to be found along with A, B, V.

First of all, $A_x = 0$, and $A = A(t)$ is an arbitrary function of time. Then we take $A_t - B_x = 0$, whence:

$$B(x,t) = \dot{A}x + A^2\dot{D}\,,$$

with an arbitrary $D(t)$; dots denote the time derivatives. We choose here the special form of arbitrary additive function of time for future convenience.

The last two equations form a set of equations specifying the unknowns f and V:

$$\begin{aligned} A(Af - B_t) + V_x &= 0 \\ -B(Af - B_t) + V_t &= 0 \end{aligned}$$

The force f is thus expressed via V, B, A:

$$f = -\frac{V_x}{A^2} + \frac{B_t}{A}\,, \tag{44}$$

and V is determined by the homogeneous equation in partial derivatives of the 1st order:

$$B\,V_x + A\,V_t = 0$$

Its characteristic curve $x(t)$ is then obtained from the equation:

$$\frac{dx}{dt} = \frac{B}{A} = \frac{\dot{A}x + A^2\dot{D}}{A}\,.$$

Integration gives the lines of constant level of V:

$$X \equiv \frac{x}{A(t)} - D(t) = const\,.$$

Hence,

$$V(x,t) = U\Big(\frac{x}{A(t)} - D(t)\Big)\,,$$

where $U(X)$ is an arbitrary function.

Thus we conclude, that the general solution to our problem of integrable system in 1.5D with quadratic invariant is generated with three arbitrary functions: $A(t)$, $D(t)$, $U(X)$. The corresponding force f is then found from (44):

$$f = -\frac{1}{A^3}U' + \frac{1}{A}(\ddot{A}x + (A^2\dot{D})\dot{}) .$$

The Hamiltonian of this system can be found from the expression for f:

$$\mathcal{H}(x,p,t) = \frac{p^2}{2} + \frac{1}{A^2}U(\frac{x}{A} - D) - \frac{A\ddot{A}}{2}(\frac{x}{A})^2 - (A^2\dot{D})\dot{}\,\frac{x}{A} ,$$

and the final form of the desired invariant is:

$$I = \frac{1}{2}(Ap - \dot{A}x - A^2\dot{D})^2 + U(\frac{x}{A} - D) .$$

Magnetic Structure of The Novosibirsk TAU-CHARM Factory

V.Yakimenko
Budker Institute of Nuclear Physics,
630090 Novosibirsk, Russia

September 14, 1995

1. Introduction

The main purpose of the C-TAU factory project is attaining high luminosity for a beam energy ranging from 700 to 2500 MeV. To carry out this project, it is planned to construct two intersecting rings, the lengths of which should provide a sufficiently high bunch collision frequency, on the one hand, and allow us to place on a track the systems required to control the colliding beam sizes, on the other hand. Such a storage ring allows us to pass easily to the colliding beam energy monochromatization regime by introducing the vertical dispersion and creating the vertical size mainly at the expense of pulse spread with a small betatron vertical size.

To perform the experiments with the longitudinally polarized beams at the interaction point, we need special optics. Beam polarization in the storage ring at this energy using radiation polarization is inefficient because of high values of the perimeter of the storage ring and current. That is why in the polarized beam experiments we are going to inject the polarized beams from a special storage ring with short polarization time. The injected electrons and positrons will be vertically polarized. Spin rotators installed in the arcs will provide the electron and positron beams of arbitrary spiraling at the interaction point.

To obtain the maximum luminosity, the most interesting possibility is the organization of the interaction point with a small β-function by a powerful longitudinal field. The symmetrical focusing in both directions satisfies well the idea of operating with round beams and allows us to obtain the space charge parameter $\xi > 0.1$.

Energy (Gev)	2.1
Circumference (m)	773.036
Ring radius (m)	89.63
Interbunch distance (m)	8.14
Straight section lenght (m)	100
Beam radius at IP (μ m)	33
Number of rings	2
Number of bunches per beam	95
Number of particle per bunch	2×10^{11}
b-function at IP (cm)	1
Beams emittance ($\epsilon_x = \epsilon_y$) (cm/rad)	10^{-5}
RMS bunch length (cm)	0.8
Compaction factor	$0.001 \div 0.0017$
Betatron tune ν_x	29.077
Betatron tune ν_y	31.077
Vertical damping time (s)	0.11
RF voltage (kV)	1000
RF frequency (MHz)	700
Energy loss per turn (keV)	100
Energy spread	5×10^{-4}
Harmonic Number	1805
Tune shift parameter $\xi_x = \xi_y$	0.1
Design Luminosity ($cm^{-2}s^{-1}$)	10^{34}

The C-TAU factory beam parameters should meet the requirement for maximum high luminosity of $1.0 \cdot 10^{34} cm^{-2}c^{-1}$. In addition to such a maximum luminosity regime, it is intended to obtain the beam parameters required for the so-called monochromatization and longitudinally polarized colliding beams. To operate in the mentioned regimes, we need the systems of beam emittance control.

In the energy monochromatization regime, the value of a vertical energy dispersion is chosen according to the energy spread. In this case, the value of monochromatization is determined by the ratio of the vertical betatron size and the vertical energy one.

It is necessary to completely reconstruct the experimental straight section to obtain the ultra monochromatic colliding beams $\sigma_M \approx 6$ keV. The strong quadrupoles and weak dipoles should be used for beam separation and control of the vertical dispersion function at the interection point. The length of such section is estimated to be more than 30 m. The beam parameters in this case are presented in table:

Number of particles in bunch	1.510^{11}
Interbunch distance (m)	16.28
Beta-function at IP (cm) β_x/β_y	20 / 2
The value of ξ_{max}/ξ_D	0.05 / 0.01
Beam emittance ϵ_x/ϵ_y (cm)	10^{-5} / 10^{-9}
Beam current (A)	0.4
Energy resolution σ_M (keV)	6
Luminosity $(cm^{-2}s^{-1})$	5.010^{31}

2. Storage Ring Magnetic System

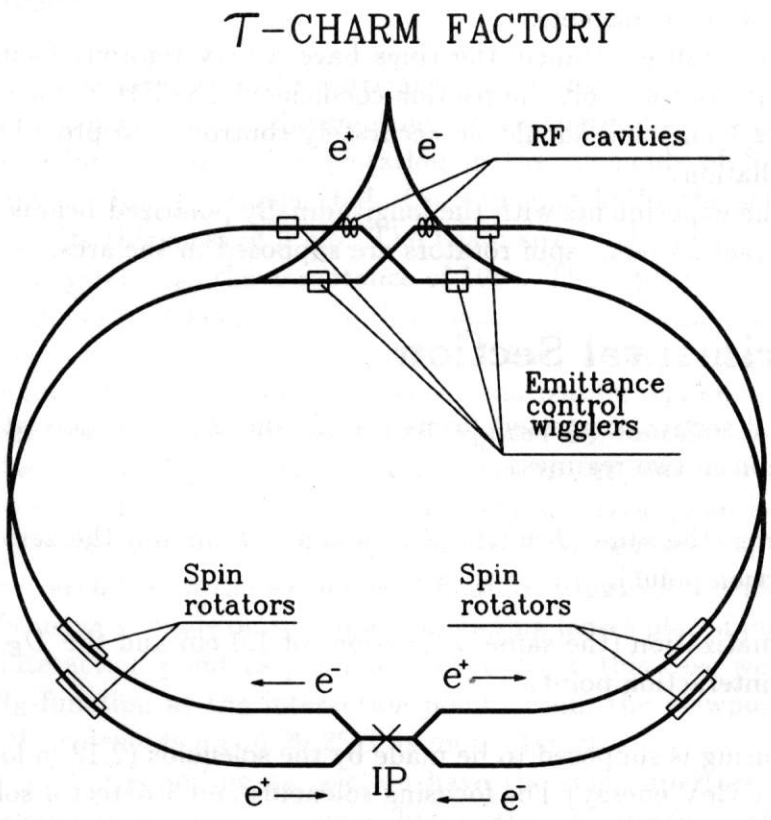

A magnetic system of the C-TAU factory comprises two storage rings of the same perimeter, which are placed one above another and intersecting at the interaction point. The magnetic system of each storage ring can be divided into four parts: two arcs consisting of the same periodicity elements and one spin rotator, and experimental and technical sections. Several bending magnets responsible for setting the dispersion function D_E to zero are in the experimental and technical sections.

In the experimental section, only the magnets and lenses focusing the beams at the interaction point and providing the optics matching with the arcs are placed. The beam collision is a head-on collision. After collision, the beams are separated by the electrical

field in the horizontal and the magnetic one in the vertical. The monochromatization is achieved by creating the vertical dispersion function at the interaction point (this is achieved by changing the lens gradients between the magnets separating the orbits in the vertical) and decreasing the vertical emittance. Since the D_E-function rotation by π is taken into account, the magnetic field distribution in the final focusing soleniods is made to be symmetrical with respect to the interaction point. This results in that the beam trajectory becomes S-shaped and the beams exchange the places after collision. The beam from the upper half-ring goes to the lower one and vice versa.

The inlet systems accelerating the resonators and the systems of control of the vertical and horizontal emittances are placed in the technical section, where the inverse beam transition occurs: from the upper half-ring to the lower one for one beam and vice versa for another. The emittances are controlled by the D_E-function at the sites of superconducting wiggler-magnets.

To obtain the small emittance, the rings have a very rigorous focusing ($\nu \approx 30$), giving a small value of the orbit compaction coefficient. The latter is necessary to obtain short bunches ($\approx$ 1 cm) and should be accurately controlled to provide the stability of synchrotron oscillations.

To perform the experiments with the longitudinally polarized beams of arbitrary spirality at the interaction pont, spin rotators are supposed in the arcs.

3. Experimental Section

The experimental section suggested forms the β- and D_E-functions at the interaction point for operation in two regimes:

- round beams (the same β-functions of about 1.0 cm and the zero D_E-function at the interaction point);
- monochromatization (the same β-functions of 1.0 cm and the D_E- function of $\approx$5 cm at the interaction point).

The final focusing is supposed to be made by the solenoids (2.18 m long, with a 9.6 T field, and at a 2.1 GeV energy).The focusing solenoids and a detector solenoid (1m long, with a 1.0 T field) turn the beam axis to one side exactly by π total, without introducing the coupling into the betatron oscillations at an equilibrium energy. The experimental section is symmetrical relative to the interaction point, except the separating magnets with the opposite-sign fields. This is required in the monochromatization regime to obtain the D_E-functions of different signs at the input of the focusing solenoids which turn the D_E-function by π .

The plates of electrostatic separation in the horizontal (2.0 m long, with a 100 kV/cm field) are supposed to be installed immediately after the focusing solenoids. The beam separation at the first spurious interaction point (which is immediately after the plate ending) is about 1.0 cm or has the order of 3σ . Prior to the second spurious interaction

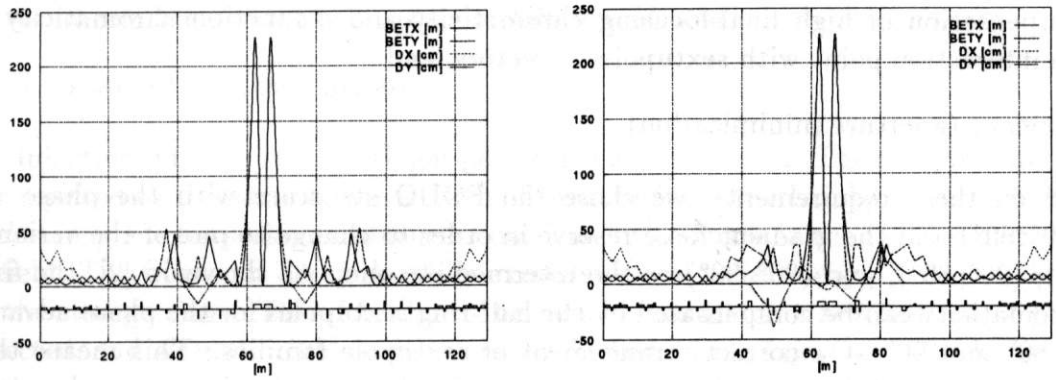

Figure 1: The experimental section with the zero D_E-function (from the left) and D_E = 5 cm (from the right)

point, the beams are separated in the vertical by a septum-magnet. Since the betatron oscillation phase advance between the spurious interaction points (before and after the main interaction point) is close to π (rotation in the solenoids of final focusing and detector), their interaction is compensated. On a magnet knife, the separation is equal to ± 5 cm, allowing its thickness of 3 cm. The beam size in the magnet is about 1 mm, and the separation system has the acceptance of 10σ . The septum-magnet, the vertical magnet restoring the orbit plane, and the three lenses between them are responsible for the parallel transfer of the orbit plane by ± 0.5 m. Thus, in the regular section the orbit structures are separated by 1.0 m. In the monochromatization regime, the two additional lenses between the magnets help to obtain the required D_E-functions at the interaction point. Setting the vertical D_E-function to zero occurs in the magnet restoring the orbit plane in both regimes. The plates of the electrostatic separation can be replaced by an RF cavity, which forms a transverse electrical field of 500 kV/cm, 20 cm long. As an alternative to the variant with the solenoids of final focusing, we consider the variant at which the final focusing is made on the superconducting lenses placed inside the detector as close to the interaction point as possible. However, in this case we fail to keep the control of the D_E-function at the interaction point. From the viewpoint of optics, the field increase in the solenoids up tp 20-25 T is more attractive.

All the lenses of the experimental section have the same aperture as the lenses of the periodicity elements, except the lens splitting the D_E-functions after the focusing solenoids. A substantial change in the focusing force is achieved by changing the lens length.

4. Periodicity Element

A magnetic structure is determined by the following requirements:

- emittance minimization,
- minimization of the orbit compaction coefficient,

- compensation of high final-focusing chromaticity and β-function chromaticity at the interaction point with sextupole correctors, and
- efficiency (aperture minimization).

Based on these requirements, we chose the FODO structure with the phase advance (60°; 60°) and the gradient force reserve in order to change to one of the variants: (60°; 90°), (90°; 60°), and (90°; 90°) or the intermediate one. As shown in [2], the final focus chromaticity can be compensated by the half-ring sextupoles for the phase advance between 60° and 90° at a correct arrangement of sextupole families. This means that with the change in the phase advance, we ought to recommutate the sextupole power supply polarities or they should be supplied separately.

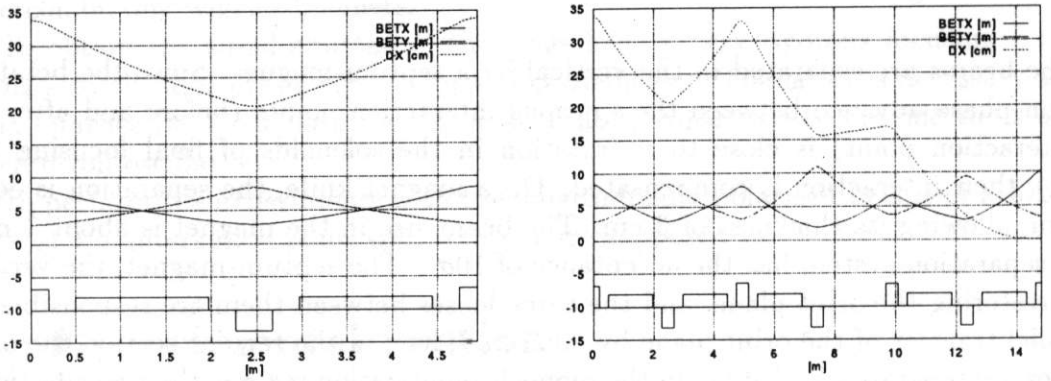

Figure 2: Periodicity element (from the left) and section of setting the D_E-function to zero (from the right)

5. Section of Setting the D_E-Function to Zero

The section of setting the D_E-function to zero consists of three periodicity elements with one "forgotten" magnet. By changing the gradients, we can provide the matching of optic functions for the phase advance on the periodicity element ranging from 60 deg. to 90 deg. without changing the ring geometry.

6. Technical Section

In the technical section, the following problems are solved:

- injection into the storage ring;
- control of horizontal emittance;
- dispersionless section with a set of the RF cavities;

- achromatic parallel orbit-plane displacement; and
- control of vertical emittance.

Injection into the storage ring is performed in the vertical. The electrons and positrons are injected by the same schemes, each of them includes the Lambertson magnet and two kicker magnets for prekick and correction. The kick is made in the vertical by the magnetic field. The front and decay duration exceeds several times the gap between the bunches in the storage rings. Therefore, both the bunch, into which a new portion of particles is injected, and several neighbouring ones are kicked during injection. The kicker-magnets with a ferrite filler and a metallized (for impedance decrease) glass or ceramic chamber are supposed to be used.

The magnetic structure is optimized to minimize the angle created by the kicker-magnet. The injection sections are at the inputs of the half-ring. The correction kicker-magnet is placed in a vacant gap of the section of setting the D_E-function to zero so that the vertical betatron phase advance from the kicker-magnet of the prekicker be exactly π. The injected bunch is carried over the orbit by the Lambertson magnet, 1 m long, with a 8 cm aperture, and the C-shaped magnet, 1.5 m long, around a preceding lens at a 30 cm distance in the horizontal. An approximate phase advance equality by $\pi/2$ between the Lambertson magnet knife and the correctors is attained automatically.

The emittance control is supposed to be made by using two analogous sections (all the elements of one section are turned by $\pi/2$), which are mirror-symmetrical relative to the superconducting wigglers installed in the middle. The field direction in the wigglers is vertical for both sections and coincides in the main pole with that in the bending magnets. This is necessary for operation with the polarized beams, makes easy the manufacture of similar wigglers, and does not produce a vertical "fan" of rigorous synchrotron radiation. The structure of each section allows us to control (in the vertical and the horizontal) the D_E-function in the wiggler from 0 to 1 m, making possible the emittance control independent of the synchrotron losses. This solution allows us to minimize the adverse increase in the emittance at the expense of a large dispersion function in the deflecting magnets, which is substantial in the monochromatization regime in the case, where the vertical emittance minimization is required.

Each structure has four FODO cells with eight magnets of the same length from each side (Fig. 3). The magnets deflect an equilibrium-orbit wave with the amplitude of no less than 5 cm:$(H, -H, -2H, 2H, 2H, -2H, -2H, 2H)$. The dispersion function is controlled by changing the gradients of the lenses (phase advance between the magnets). The magnet fields are unchanged, so the orbit distortions remain constant. The field in these magnets is due to a compromise between a desire to obtain a high value of the D_E-function and the one to minimize the contribution of the dispersion function deflecting magnets. ???

The sign alternation and setting the field integral to zero in the deflecting magnets keep the spin vertical in the wiggler, minimizing the beam polarization distortion during the vertical dispersion function deflection.

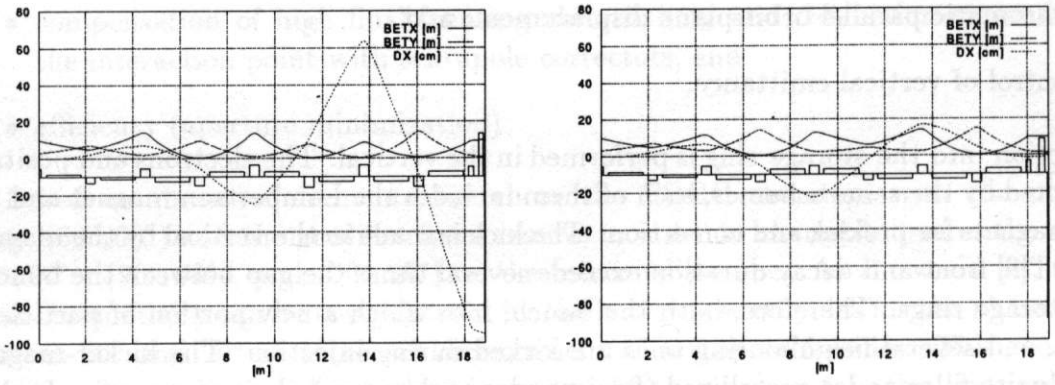

Figure 3: A half of a dispersion function control insertion for the maximum value of D_E (from the left) and zero D_E (from the right) in the superconducting wiggler

The dipole and quadrupole magnets are as those in the periodicity elements of the arcs.

The RF cavity sections and the section of achromatic parallel orbit-plane displacement by 1 m are approximately in the middle of the technical section. The section of displacement compensates the analogous effect in the experimental section.

7. Spin Rotator

The spin rotators are optimized for minimization of orbit disturbance in the regime of operation with the nonpolarized beams. The spin rotators turn the spin orientation by $\pi/2$ relative to the longitudinal axis. Their position in the arcs is chosen so that the remaining magnets turn the spin relative to the vertical axis by $\pi/2$ at the experimental energy. Thus, depending on the sign of the first turn the spin either parallel to the velocity vector or antiparallel to it at the interaction point. With a substantial change in the energy of the polarized beam experiment, the spin rotators should be rearranged.

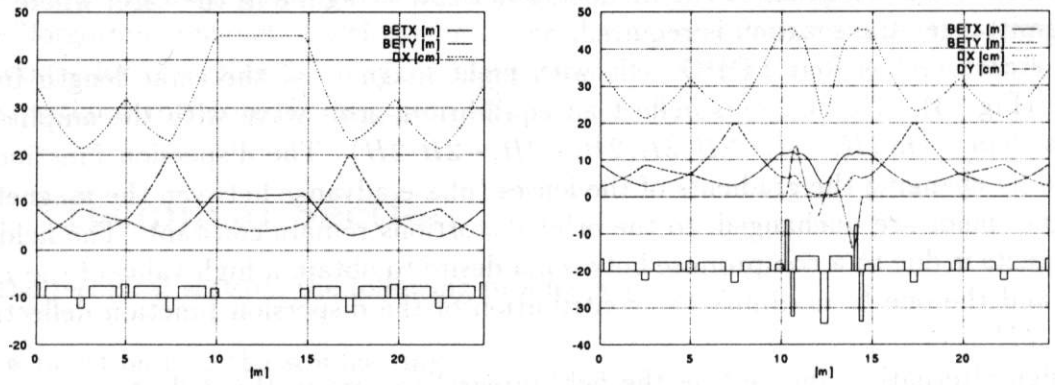

Figure 4: Optical functions for the switched-off (from the left) and switched-on (from the right) spin rotator

The spin rotator scheme is analogous to that proposed in [3], with a transport matrix of the form $\begin{pmatrix} A & 0 \\ 0 & -A \end{pmatrix}$, where $A = \begin{pmatrix} 1 & L \\ 0 & 1 \end{pmatrix}$ and L is the length occupied by the rotator. To realize this scheme, we need two lenses surrounding each solenoid and turned by $\pi/4(1 + ag)$, and a powerful (probably, superconducting) quadrupole between the solenoids.

The length L is chosen to be equal to that of the periodicity element. At the ON/OFF regime of the spin rotator, the horizontal phase does not change and the vertical one increases by 1/2 (by 1.0 on two rotators).

Two periodicity elements on each side supplied separately of the other elements of the half-ring provide the matching of the optics and geometry (the magnets additionally turn to obtain a required angle).

References

[1] Dikansky N.S., at el. *Status of the VEPP-5 Complex*, Proc. of EPAC94, London, 1994, p.482

[2] R.Brinkmann and F.Willeke, Proc. Second Advanced ICFA Dynamics Workshop on Aperture-Related Limitations of the Performance and Beam Lifetime in Storage Rings, Lugando, Switzeland,1988, CERN 88-04, (1988), 208-212.

[3] A.A. Zolents, B.N.Litvenenko, INP Preprint 81-80, Novosibirsk, (1980).